



저작자표시-비영리-변경금지 2.0 대한민국

이용자는 아래의 조건을 따르는 경우에 한하여 자유롭게

- 이 저작물을 복제, 배포, 전송, 전시, 공연 및 방송할 수 있습니다.

다음과 같은 조건을 따라야 합니다:



저작자표시. 귀하는 원저작자를 표시하여야 합니다.



비영리. 귀하는 이 저작물을 영리 목적으로 이용할 수 없습니다.



변경금지. 귀하는 이 저작물을 개작, 변형 또는 가공할 수 없습니다.

- 귀하는, 이 저작물의 재이용이나 배포의 경우, 이 저작물에 적용된 이용허락조건을 명확하게 나타내어야 합니다.
- 저작권자로부터 별도의 허가를 받으면 이러한 조건들은 적용되지 않습니다.

저작권법에 따른 이용자의 권리는 위의 내용에 의하여 영향을 받지 않습니다.

이것은 [이용허락규약\(Legal Code\)](#)을 이해하기 쉽게 요약한 것입니다.

[Disclaimer](#)

공학박사학위논문

**Cell Behavior Modulation using  
Biophysical Interactions**

물리적 자극을 이용한 세포 거동 조절 및 활성화 연구

2015년 8월

서울대학교 대학원

기계항공공학부

이 수 진

# Cell Behavior Modulation using Biophysical Interactions

물리적 자극을 이용한 세포 거동 조절 및 활성화 연구

지도교수 이 정 훈

이 논문을 공학박사 학위논문으로 제출함

2015 년 8 월

서울대학교 대학원

기계항공공학부

이 수 진

이수진의 공학박사 학위논문을 인준함

2015 년 8 월

위	원	장	<u>전 누리</u>	(인)
부	위	원	<u>이 정 훈</u>	(인)
위		원	<u>김 병 수</u>	(인)
위		원	<u>강 지 운</u>	(인)
위		원	<u>신 현 정</u>	(인)

# Abstract

## Cell Behavior Modulation using Biophysical Interactions

Sujin Lee

School of Mechanical and Aerospace Engineering

The Graduate School

Seoul National University

In this thesis, we report the effect of nano- micro- scale materials having various material property affecting cellular responses. For this purpose, micro-scale pillar array which has stepped structure with varying bottom diameter were fabricated by double step photolithography process. Single walled carbon nanotube and magnetic nanoparticle were also engineered to stimulate cellular behaviour. These materials were successfully embedded into cellular system to regulate its migration behaviour, morphology and viability. Our study could give a pioneer understanding regarding cellular response affected by nano- micro- scale systems.

First, we designed a new variation of the microfabricated polymeric pillar array platform that can decouple the stiffness gradient from the focal adhesion area of a cell. This goal is achieved via a “stepped” micro pillar array device (SMPAD) in which the contact area with a cell was kept constant while the diameter of the pillar bodies was altered to attain the proper mechanical stiffness. Using double-step SU-8 mold fabrication, the diameter of the top of every pillar was manufactured to be

identical, whereas that of the bottom was changeable, to achieve the desired substrate rigidity. Fibronectin is immobilized on the pillar tops, providing a focal adhesion site for cells. C2C12, HeLa and NIH3T3 cells were cultured on the SMPAD, and the motion of the cells was observed by time-lapse microscopy. Using this simple platform, which produces a purely physical stimulus, we observed that various types of cell behaviour are affected by the mechanical stimulus of the environment. We also demonstrated directed cell migration guided by a discrete rigidity gradient by varying stiffness.

Next, we demonstrate that the nano-scale magnetic modulation of mitochondrial VDAC2, which is the only mammalian-specific isoform among VDAC isoforms, can contribute to protect the neurodegenerative disease attenuating the changes in the intracellular calcium levels that were induced by beta-amyloid. In this study, BMPs originated from *Magnetospirillum* sp. AMB-1 directly conjugated with VDAC2 antibody using 1-Ethyl-3-(3-dimethylaminopropyl) carbodiimide (EDC) linker which is used to couple carboxyl groups to primary amines. BMPs-VDAC2 antibody complexes (BMPs-Ab) introduced into SH-SY5Y cells, human derived neuroblasts which are often used as *in vitro* models of neuronal function and differentiation. We investigated that the effect of magnetically modulated VDAC2 on the change of intracellular  $Ca^{2+}$  levels induced by  $A\beta$ . SH-SY5Y cells were loaded with 5  $\mu$ M Fluo-3 AM for 30 min, and then the changes in the level of  $Ca^{2+}$  before and after treatment with  $A\beta$  were measured by 488-nm laser source to excite Fluo-3. BMPs-VDAC2 antibody complexes (BMPs-Ab) introduced into SH-SY5Y cells were successfully internalized into SH-SY5Y cells. We found that the capture of VDAC2 with BMPs-Ab was significantly decreasing the expressed intracellular calcium levels induced by  $A\beta$ . This magnetic modulation of VDAC2 considerably increases the proliferation and reduced  $A\beta$ -induced toxicity in SH-SY5Y. These results suggest that magnetic modulation of VDAC-2 is able to protect the neurodegenerative disease attenuating the changes in the intracellular calcium levels

that were induced by A $\beta$ .

Finally, we investigated a self-degradation route for single-wall carbon nanotubes (SWNTs) mediated by built-in peroxidase-like activity of bacterial magnetic nanoparticles (BMPs). Biocompatible BMPs originated from *Magnetospirillum* sp. AMB-1 were directly conjugated through covalent bonding to yield functionalized SWNTs (f-SWNTs) without any additional functionalized processes. Employing transmission electron microscopy (TEM) and Raman spectroscopy, we found that BMPs can act as effective built-in intrinsic peroxidase compare to other enzymatic methods for the degradation of SWNTs. For the possible application in neurobiology, f-SWNT-BMP hybrids were shown as an inhibitor to reduce formation of amyloid-beta (A $\beta$ ) fibrils which is considered as the key element behind Alzheimer's disease. To conform this, we showed that neurotoxicity of A $\beta$  peptide affecting SH-SY5Y cell death is reduced in the presence of these hybrids. Our findings could offer a new approach of mitigating the toxic impact and neurobiological application of CNTs.

**Keywords:** PDMS pillar array, Bacterial magnetic nanoparticle, Single-walled carbon nanotube, Cell migration, Mitochondria targeting, Self-degradation

**Student Number:** 2009-31248

# Contents

<b>Abstract</b>	<b>i</b>
<b>Contents</b>	<b>iv</b>
<b>List of Figures</b>	<b>viii</b>
<b>List of Tables</b>	<b>xviii</b>
<b>Chapter 1 Introduction</b>	<b>1</b>
1.1 Cell behavior	2
1.1.1 Apoptosis	2
1.1.2 Differentiation	4
1.1.3 Cell growth and proliferation	7
1.1.4 Cell migration	9
1.2 3-D fabrication techniques	12
1.3 Nano- scale structure fabrication	15
1.4 Soft lithography for micro- fabrication	18
1.5 Summary	21

<b>Chapter 2 Cell with Microstructure</b>	<b>2 2</b>
2.1 Introduction	2 3
2.2 Materials and Methods	2 6
2.2.1 Geometric considerations	2 6
2.2.2 Fabrication process	2 7
2.2.3 Data acquisition	3 0
2.2.4 Cell preparation	3 0
2.2.5 Immunofluorescence staining	3 0
2.2.6 Quantification	3 1
2.3 Results	3 2
2.3.1 SMPAD characterization	3 2
2.3.2 Analysis of SMPAD stiffness	3 4
2.3.3 Cell morphology on the soft and stiff pillar array	3 7
2.3.4 Cell motion on the soft-to-stiff pillar array	3 9
2.3.5 Cell motility analysis	4 2
2.4 Summary	4 8
<b>Chapter 3 Nanomaterials in Biology Application</b>	<b>4 9</b>
3.1 Bacterial Magnetic Nanoparticle conjugated VADC2 Antibody	5 0
3.1.1 Materials and Methods	5 2
3.1.1.1 Preparation of BMPs	5 2
3.1.1.2 Conjugation of VDAC2 antibody to BMPs	5 2
3.1.1.3 Amyloid beta 25-35 aging	5 3
3.1.1.4 Cell culture and BMPs loaded cell preparation	5 3
3.1.1.5 Intracellular calcium level measurement	5 3
3.1.1.6 Fluorescence labelling	5 4
3.1.1.7 Cell viability assay	5 4

3.1.1.7.1	ATP assay MTS assay	5 4
3.1.1.7.2	ATP assay	5 5
3.1.2	Results	5 6
3.1.2.1	BMPs preparation and VDAC2 targeting	5 6
3.1.2.2	Calcium level	6 0
3.1.2.3	BMP-VDAC2 ab loaded cell viability	6 4
3.1.2.4	Effects on amyloid beta induced injury	6 6
3.1.3	Summary	6 9
3.2	Bacterial Magnetic Nanoparticle–Decorated Single-Wall Carbon Nanotubes	7 0
3.2.1	Materials and Methods	7 3
3.2.1.1	Carboxyl functionalization of SWNTs	7 3
3.2.1.2	BMP extraction and purification	7 3
3.2.1.3	Conjugation of f-SWNTs to BMPs	7 3
3.2.1.4	High-resolution transmission electron microscopy	7 4
3.2.1.5	EDS/FE-SEM preparation	7 4
3.2.1.6	XPS analysis	7 4
3.2.1.7	Raman microscopy of the f-SWNT-BMP hybrids	7 5
3.2.1.8	Catalytic activity of f-SWNT-BMP hybrids	7 5
3.2.1.9	Degradation of f-SWNTs	7 5
3.2.1.10	Thioflavin T assay for A $\beta$ fibril formation	7 6
3.2.1.11	MTS assay for cell viability	7 6
3.2.2	Results	7 8
3.2.2.1	Synthesis of the f-SWNT-BMP hybrid	7 8
3.2.2.2	Characterization	8 0
3.2.2.3	Catalytic activity of the hybrids as a peroxidase	8 3
3.2.2.4	Self-degradation of BMP-Decorated f-SWNTs	8 9
3.2.2.5	Inhibition of amyloid beta fibrillation	9 4
3.2.2.6	Prevention of A $\beta$ -induced neurotoxicity	9 7

3.2.3 Summary	1 0 0
<b>Chapter 4 Conclusion</b>	<b>1 0 1</b>
<b>Bibliography</b>	<b>1 0 4</b>
한글초록	1 2 5

# List of Figures

**Figure 1-1** A schematic showing the magnetic influences on receptor-bound magnetic nanoparticles depending on the nature of the magnetic field applied. (a) By creating a uniform magnetic field that magnetizes the particles, it is possible to induce magnetic interactions (that is, attraction) between bound particles (grey spheres) and hence promote clustering of receptors over large volumes, deep within the body. (b) A single magnet with a large field gradient, induces a translational force on a magnetic nanoparticle that drops off very rapidly with distance from the magnetic field source. This limits the depth to which receptor clustering can be magnetically actuated..... 3

**Figure 1-2** (A) Co-culture of adult rat hippocampal progenitor cells (AHPCs) with astrocytes on microgrooved PS substrate. The square illustrates how the cells align in the same direction as the microgrooves [9]; (B) Elongation of mouse mesenchymal stem cells (mMSCs) inside microgrooves on a silicon substrate [10]; (C) Attachment of rMSCs on ring shaped PMMA microstructures [11]; (D) Formation of embryoid bodies (EBs) using an array of PEG microwells [12]. .... 6

**Figure 1-3** Shapes Adopted by Cells on Islands. Scanning electron micrographs of 3T3 cells in contact with islands of the largest and smallest sizes used in these experiments. The cells were fixed 4 hr after seeding from a randomly growing culture. The volumes and shapes of these cells are

variable; typical examples are shown. Islands occupied by single cells have been selected; up to 60 % of the islands are occupied by either more or less than one cell. Some shrinkage occurs during the process of preparation for electron microscopy. Scale = 50  $\mu\text{m}$ ..... 8

**Figure 1-4** Mc3t3 osteoblasts in contact with a biofunctionalized 80 nm pattern and exhibiting cell protrusions sensing the pattern. Scale bars, (a) 20  $\mu\text{m}$  and (b) 200 nm. (c) Projected cell area ( $\pm$ s.e.m.) as a function of substrate position. Insets: Mc3t3 osteoblasts after 23 h adherence on a homogeneously nanopatterned area with 50 nm c(-RGDfK-) patch spacing (left) and along the spacing gradient (right), respectively. Cells are immunostained for vinculin (green), and actin is visualized using TRITC (6-tetramethylrhodamine isothiocyanate)-phalloidin (red). Scale bars: 20  $\mu\text{m}$  (left); 200 nm (right)..... 1 1

**Figure 1-5** (A) Photographs of the pin holder device for the magnetic cell patterning. A photograph of a magnetic soft iron (A-1) that contains more than 6000 square pillars (100  $\mu\text{m}$  width, 100  $\mu\text{m}$  length, 300  $\mu\text{m}$  height) with center-to-center distance of 250  $\mu\text{m}$  (A-2, A-3). (B) Schematic diagram for fabrication of the 3D cell culture array using magnetic force and a pin holder device. The magnetically labeled cells were seeded into a culture dish with a thin layer of collagen gel and patterned into an array. The patterned cells were further embedded with collagen gel to construct the 3D cell array. (C) Side view of the scheme for the magnetic cell patterning in 3D. . 1 4

**Figure 1-6** Process flow diagram of substrate patterning and protein immobilization. Spin-coated PMMA polymer is patterned by NIL. Exposed  $\text{SiO}_2$  regions are etched and a passivating  $(\text{CF}_x)_n$  polymer ( $x = 1$  or  $2$ ,  $n =$  number of monomer subunits, monomer MW = 31 or 50) is deposited during a  $\text{CHF}_3$  RIE procedure. Residual PMMA is stripped away with acetone, exposing the underlying  $\text{SiO}_2$  in the “patterned regions.” An aminosilane monolayer is covalently attached to the exposed “patterned regions”. Biotin-succinimidyl

ester is then covalently linked to the primary amine of the aminosilane layer, and streptavidin is bound to the biotin layer. Finally, the biotinylated target protein is bound to the streptavidin layer..... 1 6

**Figure 1-7** Cellular micropatterns on templates of physisorbed ECM proteins on biocompatible materials. The templates were created by microfluidic patterning on polystyrene (a), poly(methyl methacrylate) (b), a gold microelectrode pattern on glass (c), an underlying protein micropattern on polystyrene (d), and microtextured PDMS (e). The template, made of collagen (a, c-f) or fibronectin (b, d), induced the selective attachment and spreading of hepatocytes (a-d, f) or keratinocytes (e). ..... 2 0

**Figure 2-1** Illustrations of the Stepped Micro Pillar Array Device (SMPAD) presented here. An illustration of a binary type of SMPAD with a soft pillar array (left) and stiff pillar array (right) (a). Plots of the force and deformation relationship produced on a soft (left) and stiff (right) type of SMPAD (b). The spring constant is proportional to the bottom pillar diameter of the SMPAD ( $F=kx$ , where  $k$  is the spring constant). Illustration of the pillar arrangement (c). The black dot represents a single SMPAD, and the dashed line is the distance between pillars in the SMPAD ( $d=10\ \mu\text{m}$ ). Square (left) and hexagonal (right) arrangements were used here. Side view of gradient types of the SMPAD (d) and (e). Of note, there is a slower increase in the bottom pillar diameter toward the right in the low-strength SMPAD (d) than in the high-strength SMPAD (e). ..... 2 5

**Figure 2-2** Process flow for the SMPAD fabrication. A bare silicon wafer was prepared after piranha cleaning and dehydration processes (a). SU-8 2002 spin coating and flood exposure for the SMPAD base (b). SU-8 2010 spin coating and exposure for the bottom portion of the SMPAD (c). SU-8 2002 spin coating and exposure for the top portion of the SMPAD (d). Developing process for the positive SMPAD

master (e). PDMS casting for the negative mold (f). A cover glass was used to press inter-filling PDMS and generate the thin SMPAD substrate (g). Completed SMPAD substrate (h). Fibronectin coating of the top of the SMPAD using a contact printing method (i). Prepared ECM coated SMPAD (j). Adherent animal cells were seeded and cultured on the prepared SMPAD (k)..... 2 9

**Figure 2-3** Micrographs of SMPAD. SEM images of the positive SU-8 SMPAD master, which has a binary stiffness substrate (a), and the prepared polymeric SMPAD with stiffness gradients (b). Fluorescence image visualizing fibronectin absorption on SMPAD (c). Green dots represent printed fibronectin, and yellow curves represent protein intensity. Cell attachment on the SMPAD 3 h after cell seeding (d)-(f). Images were obtained by optical microscopy (d), confocal microscopy, and SEM (f). Scale bar, 10  $\mu\text{m}$ . ..... 3 3

**Figure 2-4** Force and displacement plots using AFM. The force and z-displacement relationship of the AFM cantilever beam while applying forces on glass and PDMS substrate (a). SMPAD pillars with different bottom diameters (2.5, 5.5, and 7.5  $\mu\text{m}$ ) were also tested to obtain the force-displacement characteristics of the AFM cantilever (b)..... 3 5

**Figure 2-5** Spring constant in the x-direction. Calculated values using the formula presented here are illustrated by black dots, and the values measured by the AFM cantilever tip are shown as red dots. The measured spring constant primarily followed the calculated values; a rapid increase between the soft and stiff types of SMPAD was observed (a). The gradually increasing spring constant with the SMPAD gradient type is shown in (b). (n=5). ..... 3 6

**Figure 2-6** Cell morphology obtained by confocal microscopy. The nucleus, vinculin and actin filament of cultured cells on the soft (left column) and stiff (right column) types of SMPAD were visualized using DAPI, vinculin and actin antibodies respectively. Scale bar, 10  $\mu\text{m}$ . ..... 3 8

**Figure 2-7** Cell responses and migratory behavior on SMPAD with the binary stiffness pillar array (a). When a cell was attached to the soft portion of the substrate, it investigated the surrounding environment with a tapping motion and slowly moved toward the stiff portion of the substrate (cell 1). Although the cell began to move from the stiff portion of the substrate and touched the soft portion, it quickly displaced toward other stiff portions of the substrate (cell 2). The cell explored and migrated along the stiffness boundary and remained on the other stiff area when the cell had initially attached to a stiff portion of the substrate (b). Scale bar, 50  $\mu\text{m}$ . To monitor the real-time cell migration in different cell types, we cultured C2C12 and HeLa cells on our devices. We counted the number of cells on the soft and stiff portions of the substrate every 3 h for up to 21 h. For C2C12, a tendency to move toward the stiff area was observed on C2C12 (c) and NIH3T3 (d). ..... 4 1

**Figure 2-8** NIH3T3 behavior on flat PDMS (Control), SMPAD with identical stiffness (Uniform), and SMPAD with gradually increasing stiffness in the x-direction (Gradient) (a). Cell showed directional migration in the direction of increasing stiffness over 180 min. The net distance traveled by migrated cells in 30 min increments up to 300 min was used to compare the motion of cells on three types of substrate (b). No specific tendency for migration direction was observed between groups at up to 150 min. However, a particular increase in travel distance was observed from 150 min to 210 min, and the cells that attached to the gradient substrate travelled much further than the cells attached to other types of substrates. \* $p < 0.05$  and \*\* $p < 0.005$ ..... 4 5

**Figure 2-9** The location of NIH3T3 cells 18 h after attachment to the SMPAD with low gradient strength ( $G_{0.5}$ ) (a), medium gradient strength ( $G_5$ ) (b), and high gradient strength ( $G_{50}$ ) (c) stiffness. Cells randomly distributed initially, ended up with the vicinity of indicated locations after 18 hours of migration. White arrows indicate the stiffness of the

final locations. (h: hard, m: medium, s: soft area). No difference in migration distances was observed between the x-direction and y-direction when the cells migrated on the low-strength SMPAD (d). The  $G_{0.5}$  type of SMPAD, which is the middle gradient strength, began to induce a mild increase in x-directional migration (e). The distance of cell migration increased sharply on the high-strength SMPAD along the x-direction (f). Cells on the high-strength SMPAD migrated along the x-direction with the highest velocity (g). More than 100 cells on each substrate were used to generate this result.

\*p<0.05 and \*\*p<0.005. .... 4 7

**Figure 3-1** Schematic of the BMP-VDAC2 Ab complex ..... 5 1

**Figure 3-2** (a) Magnetic attraction of BMP disperse in 1X PBS, (b) Transmission electron microscopy (TEM) image of BMP with a scale bar 50 nm. The BMPs from the *Magnetospirillum* sp. AMB-1 were used in our approach, which are inherently biocompatible, can be effectively conjugated with other biomolecules, and can be dispersed well in aqueous solutions because of their stable lipid membrane surrounding the magnetic core. .... 5 7

**Figure 3-3** Transmission electron microscopy (TEM) image of BMPs internalized by a SH-SY5y cells. (a) Control, (b) BMPs only, and (c) BMPs-antibody conjugate. .... 5 8

**Figure 3-4** Specific targeting of BMP-VDAC2 Ab complex to mitochondria inside SH-SY5Y cells; blue: nucleus, red: mitochondria, green: BMP; scale bar: 10  $\mu$ m. .... 5 9

**Figure 3-5** (a) Optical, (b) fluorescence images of normal SH-Sy5y cells; (c) optical and (d) fluorescence images of  $\beta$ -amyloid treated normal SH-Sy5y cells; and (e) optical and (f) fluorescence images  $\beta$ -amyloid treated BMP-Ab loaded SH-Sy5y cells. It is clear that  $Ca^{2+}$  level of  $\beta$ -amyloid treated normal cells is much higher than level of BMP-Ab loaded cells. .... 6 1

**Figure 3-6** Effect of BMP-VDAC2 ab complex to reduce calcium influx induced

	by amyloid beta. Calcium level was calculated from the calibrated fluorescence signal of the probe fluo-3. *p<0.05 and **p<0.01 compared with the control cell.....	6 2
<b>Figure 3-7</b>	Effect of BMP-VDAC2 Ab complex on amyloid beta-induced Ca <sup>2+</sup> influx in the SH-SY5Y cells. Control: VDAC2 untargeted, BMP-VDAC2 ab: VDAC2 targeted cells, Control + 50 μM of aβ: VDAC2 untargeted cells under Aβ treated condition, BMP-VDAC2 ab + 50 μM of aβ: VDAC2 targeted cells with BMPs-Ab under Aβ treated condition. (*p<0.05 and **p<0.01, n=3) .....	6 3
<b>Figure 3-8</b>	Effect of BMP-VDAC2 Ab complex on cell growth by (a) MTS assay and (b) ATP level. Under the amyloid-beta induced neurotoxic condition .....	6 5
<b>Figure 3-9</b>	Effect of BMP-VDAC2 Ab complex on cell growth by (a) MTS assay and (b) ATP level. Control: VDAC2 untargeted cells, BMP-VDAC2 ab: VDAC2 targeted cells with BMPs, Control + 50 μM of aβ: amyloid-beta treated VDAC2 untargeted cells, and BMP-VDAC2 ab + 50 μM of aβ: amyloid-beta treated VDAC2 targeted cells. (*p<0.05, **p<0.01, and ***p<0.001, n=4) .....	6 7
<b>Figure 3-10</b>	Schematic map of mitochondrial Ca <sup>2+</sup> transporters in the amyloid-beta induced toxicity. Aβ results in elevated cytosolic calcium levels and localize to mitochondrial membranes. Aβ in mitochondria inhibits mitochondrial ATP production and other energy-dependent functions, and releases calcium stored in mitochondria, thereby further deregulating neuronal calcium signaling. Finally, a release of proapoptotic proteins from damaged mitochondria results in neuronal injury. However, the magnetic modulation of VDAC2 should block the localization of Aβ to the mitochondria, whereas promote the Ca <sup>2+</sup> uptake into mitochondria within the threshold. Mitochondria produce ATP and maintain other functions.....	6 8
<b>Figure 3-11</b>	Illustration of f-SWNT-BMP hybrid formation. EDC and sulfo-NHS are used to activate carboxyl groups of f-SWNTs. BMPs directly	

conjugated with f-SWNTs using their primary amine groups..... 7 2

**Figure 3-12** Micrograph of f-SWNTs and f-SWNT-BMP hybrids (a), (b), (d), and (e). BMPs dangle from the f-SWNT bundles in the hybrid images (d) and (e), whereas only f-SWNTs are seen in images (a) and (b). Magnetic attraction of f-SWNTs (c) and f-SWNT-BMP hybrids (f) was performed. After functionalization, the f-SWNTs and the hybrids were fully dispersed in DI water. However, the hybrids were mutually attracted to each other and aligned with their opposite magnetic poles facing opposing f-SWNTs within a one-minute interval..... 7 9

**Figure 3-13** Raman spectra (a), EDS results of f-SWNT-BMP hybrids (b) and f-SWNTs (c). When the unmodified SWNTs (pristine) were compared with the f-SWNTs, the intensity of the G peak for the f-SWNTs and the hybrids showed no noticeable change; however, the intensity of the D peak increased drastically, resulting in an increased intensity ratio of the D to G band (a). Inset: Starting from the bottom, the D peak of pristine SWNT, f-SWNT, and hybrid. The Fe signals would have originated from the BMPs (b) because most impurities, including Ni, Co, and Fe, that were used as catalysts during the synthesis of the f-SWNTs were removed during the functionalization process (c)..... 8 1

**Figure 3-14** XPS analysis of the Fe2p peak and the N1s core level of the hybrids. Fe2p scan showing the characteristic binding energy peaks of Fe 2p<sub>3/2</sub> and Fe 2p<sub>1/2</sub> of Fe<sub>3</sub>O<sub>4</sub> (a). In the N1s scan, the 400.1 eV peak was assigned to the residual amino groups on the surface of Fe<sub>3</sub>O<sub>4</sub>, and the 401.0 eV peak was assigned to the amide groups in the hybrids (b)..... 8 2

**Figure 3-15** Peroxidase-like activity of hybrids and dependence of the peroxidase-like activity on the H<sub>2</sub>O<sub>2</sub> concentration and the time-dependent absorbance changes at different H<sub>2</sub>O<sub>2</sub> concentrations. Color change of the TMB substrate in TMB + H<sub>2</sub>O<sub>2</sub> (a), TMB + H<sub>2</sub>O<sub>2</sub> + BMPs (b),

and TMB + H<sub>2</sub>O<sub>2</sub> + Hybrids (c), Synergetic peroxidase-like activity of hybrids (d), Comparison of the time-dependent peroxidase-like activity changes with hybrids and BMPs (e). The catalytic activity of the hybrids is dependent on the concentration of H<sub>2</sub>O<sub>2</sub> (f). Moreover, the hybrids quickly catalyzed the oxidation of the TMB peroxidase substrate and induced a rapid initial reaction rate and a subsequent stable stage depending on the concentration of H<sub>2</sub>O<sub>2</sub> (g). ..... 8 5

**Figure 3-16** Steady-state kinetic assay and catalytic mechanism of hybrids and BMPs. The concentration of H<sub>2</sub>O<sub>2</sub> was 50mM and the TMB concentration was varied (a), and the concentration of TMB was 1.6 mM and the H<sub>2</sub>O<sub>2</sub> concentration was varied (b). Double reciprocal plots of activity of hybrids and BMPs with fixed concentration of H<sub>2</sub>O<sub>2</sub> and varied TMB concentrations (c), and with the fixed concentration of TMB and varied H<sub>2</sub>O<sub>2</sub> concentrations (d)..... 8 7

**Figure 3-17** TEM images (a)-(d) and Raman spectra (e) and (f). Most of the f-SWNTs remained bundled in the H<sub>2</sub>O<sub>2</sub> condition after 24 h of incubation (b), whereas the majority of the f-SWNT-BMP hybrid bundles were degraded, leaving residual BMPs and carbonaceous material in the samples after the BMP-induced degradation (d). Scale bars are 200 nm. In the Raman spectra, the I<sub>D</sub>/I<sub>G</sub> ratio for the hybrids drastically increased compared with that for the f-SWNT sample due to the BMP-induced degradation (e) and (f). ..... 9 1

**Figure 3-18** Raman spectra of the hMPO-induced and BMP-induced degradation of f-SWNTs. The intensity of the D-band for the hybrids under BMP-induced degradation (1) was higher than that of the f-SWNTs under hMPO-induced degradation (2). The relative degradation ratio (I<sub>D</sub>/I<sub>G</sub>) for the BMP-induced degradation was also higher than the hMPO-induced degradation. In addition, in the Raman spectra for BMP-induced degradation, the hybrid showed clear disappearance of the radial breathing mode (RBM) at 169 cm<sup>-1</sup>, indicating the destruction of the tubular structures in the f-SWNTs. .... 9 3

- Figure 3-19** Fluorescence images of A $\beta$  fibrils in the absence and presence of hybrids (a) and (b) and signal intensity comparison (c). To visualize A $\beta$  fibrils in solution, FITC-labeled A $\beta$  antibodies were combined with the samples after 7 days of A $\beta$  incubation. A fluorescence image of A $\beta$  without hybrids (a) shows a stronger signal than the A $\beta$  with hybrids (b). The scale bars are 10  $\mu$ m..... 9 5
- Figure 3-20** ThT assay results of A $\beta$  only, A $\beta$  with BMP, SWNT and Hybrid. Here, we clearly observed a quenching effect, which reduces the fluorescence signal (red, blue, green dots). Meanwhile, the signal from the A $\beta$  without hybrids was greatly increased (black dots) during the 18 h of observation. .... 9 6
- Figure 3-21** Optical microscopy images of cultured SH-SY5Y cells with and without hybrids. We observed that there is no significant difference between without (a) and with (b) hybrids in the survival of the SH-SY5Y cells after 3 days of cell culture. The scale bars are 200  $\mu$ m. From the MTS assay, the cytotoxic effects of the hybrids on the viability of the SH-SY5Y cells were also insignificant, even at a high concentration of 20  $\mu$ g/ml (c). .... 9 8
- Figure 3-22** Effect of the BMP, SWNT and hybrids on the SH-SY5Y cell growth under the amyloid-beta-induced neurotoxic condition by MTS assay. Control: untreated cells, A $\beta$ : 200  $\mu$ M A $\beta$ -treated cells, A $\beta$ +BMP: 200  $\mu$ M A $\beta$  and 10 ng/ml BMP-treated cells, A $\beta$ +SWNT: 200  $\mu$ M A $\beta$  and 10 ng/ml SWNT-treated cells and A $\beta$ +HYB: 200  $\mu$ M A $\beta$  and 10 ng/ml hybrids-treated cells. This results showed that the cell viabilities of the hybrid-treated cells increased by more than 30%. 9

## List of Tables

<b>Table 1-1</b> Mimicking ECM components to create cell microenvironment .....	1 7
<b>Table 3-1</b> Comparison of the apparent Michaelis–Menten constant ( $K_m$ ) and maximum reaction rate ( $V_{max}$ ) between hybrids and BMPs .....	8 8

## **Chapter 1 Introduction**

# **Nano- Micro- Technology for Cell Biology**

Cells are the basic structural and functional unit of living systems. It is hence important to understand the mechanism of how cells interact with the environment. Indeed, cells are sensitive to biochemical, mechanical, and topological cues. Our understanding of the mechanisms on how cells sense these cues and our ability to manipulate cellular behaviors accordingly will allow efficient and therapeutic intervention of related diseases and expedite the development of new methods for drug screening and discovery. Nano- micro- fabrication techniques are particularly useful in facilitating the research in this aspect by creating and mimicking the physiological and pathological cellular environment.

## 1.1 Cell behavior

### 1.1.1 Apoptosis

Normal cells usually will undergo a self-termination or apoptosis, but for cancer cells, they become immortal. It is therefore important to understand the underlying mechanisms governing the cell fate, life, or death. This understanding would help to intervene and cure different diseases. Apoptosis is a programmed cell death, involving a series of biochemical events which eventually lead to the cell death, with morphological and molecular characteristics including blebbing, changes at the cell membrane, cell shrinkage, nuclear fragmentation, chromatin condensation, and chromosomal DNA fragmentation. Apoptosis can be triggered by various stimuli involving different molecular pathways. Chen *et al.* found that cells could switch from growth to apoptosis when seeded onto small micro-patterned islands containing ECM proteins [1]. The results showed that cells attached to nonpatterned surfaces would not undergo apoptosis, but about 20% of the cells seeded on 20  $\mu\text{m}$ -diameter circle-shaped patterns would undergo apoptosis. By further decreasing the diameter size of these circle-patterns from 20 to 10  $\mu\text{m}$ , the percentage of apoptotic cells adhered on these patterns progressively increased. Similar results were observed in a later study from Dike *et al.* [2]. These results demonstrate that the cell shape is one of the important factors to determine the fate of a cell. Chiu *et al.* fabricated cell culture dishes utilizing collagen gels with different stiffness [3]. The results indicate that soft substrates could induce apoptosis in polarized cells. It appears that the soft collagen gels can up-regulate the store-operated calcium influx across the cell membrane to increase the cytosolic calcium levels. This disturbed calcium homeostasis eventually resulted in the activation of l-calpain, which cleaves l-spectrin to induce actin disorganization and apoptosis. Recently, Dobson showed that a magnetic on/off switch for cell-death signalling in cancer cells is developed using antibodies conjugated to magnetic nanoparticles (Figure 1-1) [4].

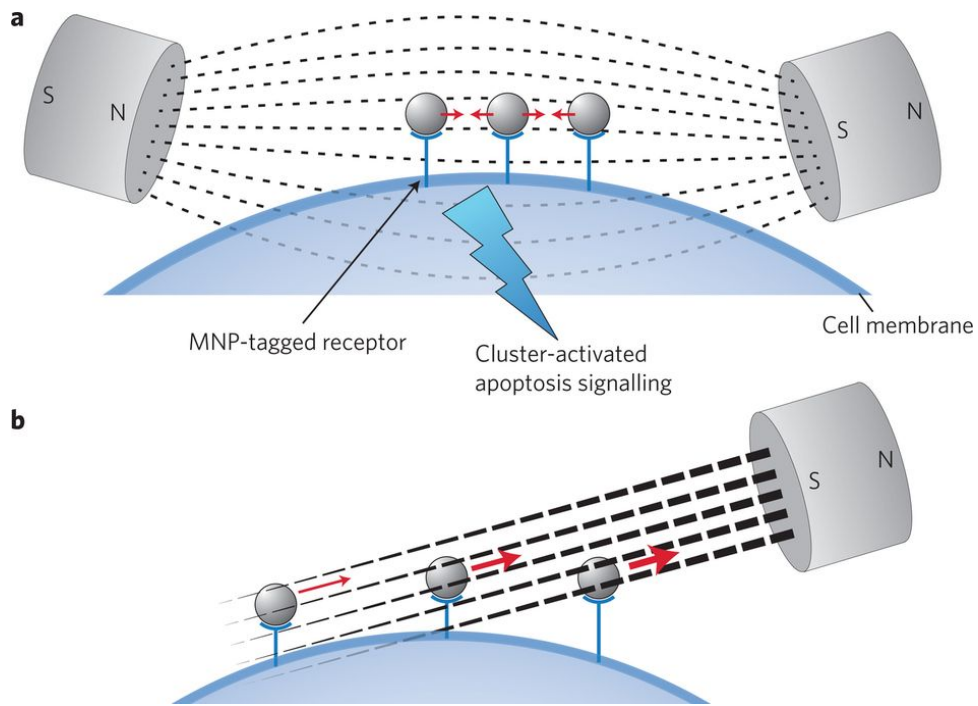


**Figure 1-1** A schematic showing the magnetic influences on receptor-bound magnetic nanoparticles depending on the nature of the magnetic field applied. (a) By creating a uniform magnetic field that magnetizes the particles, it is possible to induce magnetic interactions (that is, attraction) between bound particles (grey spheres) and hence promote clustering of receptors over large volumes, deep within the body. (b) A single magnet with a large field gradient, induces a translational force on a magnetic nanoparticle that drops off very rapidly with distance from the magnetic field source. This limits the depth to which receptor clustering can be magnetically actuated.

### 1.1.2 Differentiation

Although the molecular mechanisms involved in the renewal and apoptosis of cells appear different, ample evidence has shown that those two processes are related in cells under different mechanical/physical/chemical environment. Indeed, geometric control of the substrate can switch the adhered cells between growth, apoptosis, and differentiation [2]. Differentiation is the process of cells becoming more specialized types. It starts right after the formation of a zygote, which differentiates into a complex system containing different tissue and cell types. This process also exists in the adult organism, usually occurring as a part of regenerative process for wound repair and tissue regeneration. For stem cells, differentiation is one of their most important features. External cues, including microenvironment, biomolecules, and the substrates, can regulate the gene expression of stem cells to switch and govern the cell fate. Here, we highlight several cases demonstrating that nano- micro-fabrication techniques were applied to manipulate the cellular microenvironment to regulate stem cell differentiation. McBeath *et al.* showed that different shapes of micropatterns can lead human mesenchymal stem cells to differentiate into adipocytes or osteoblasts [5]. The results showed that stem cells seeded on ECM with low density could differentiate into adipocyte-like cells, while those seeded on ECM with high density appeared more osteogenic. Further results indicated that these mesenchymal stem cells seeded on small or large-size patterns could differentiate into adipocytes or osteoblasts, respectively. A recent study from the same group further revealed the mechanism of stem cell differentiation on different shapes of patterns [6]. It appears that geometry determines spatial distribution of cytoskeletal tension, which regulates the differentiation of stem cells. Indeed, the cell tensions of different patterns at different locations are different, as shown in Fig. 3. Cells on the convex part of the patterns are subjected to high cellular tension, which guides MSCs to differentiate into osteoblasts. Cells at the concave part of the

patterns have lower cellular tension which leads MSCs to differentiate into adipocytes. Similar results were obtained in three dimensional cell patterns. These results are consistent with previous observations that stem cells can differentiate differently on substrates with different stiffness [7]. Consistently, direct mechanical loading can also affect the differentiation commitment of stem cells [8]. In a study by Mallapragada *et al.*, adult rat hippocampal progenitor cells (AHPCs) exhibited an elongated morphology along microgrooved laminin coated polystyrene (PS) substrates [9]. On these substrates, the elongated morphology of the cells remained intact after seeding cortical astrocytes with the AHPCs, and the differentiation of AHPCs towards an early neural phenotype (III  $\beta$ -tubulin) was enhanced after co-culturing. Likewise, mouse mesenchymal stem cells (mMSCs) were shown to exhibit an elongated morphology when cultured on microgrooves (Figure 1-2) [10].

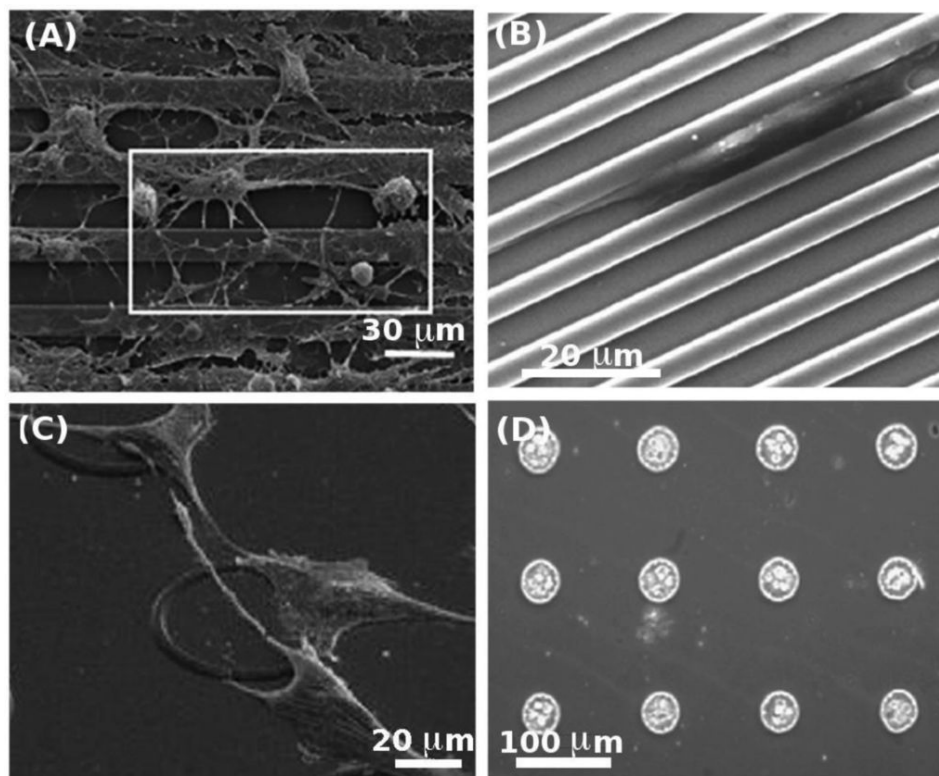


**Figure 1-2** (A) Co-culture of adult rat hippocampal progenitor cells (AHPCs) with astrocytes on microgrooved PS substrate. The square illustrates how the cells align in the same direction as the microgrooves [9]; (B) Elongation of mouse mesenchymal stem cells (mMSCs) inside microgrooves on a silicon substrate [10]; (C) Attachment of rMSCs on ring shaped PMMA microstructures [11]; (D) Formation of embryoid bodies (EBs) using an array of PEG microwells [12].

### **1.1.3 Cell growth and proliferation**

Cell growth and proliferation refer to the growth of cell population, which are dependent on the cell adherence to solid surfaces. The whole process of cell proliferation starts with cells adhering to the substrate surface, with parental cells dividing to generate daughter cells. More populated cells then migrate out to continuously colonize the surface until a crowded cell sheet is formed and proliferation stopped. O'Neill *et al.* seeded whole mouse embryo (WME) and NIH 3T3 cells on patterned areas with different size (Figure 1-3) [13]. The results indicate that the DNA synthesis for WME cells is limited whereas a 6-fold increase could be observed in NIH 3T3 cells when the cells were constrained on a small growing area. Therefore, the alteration of shape or area where cells are seeded can significantly affect the synthesis of DNA and, subsequently, cell proliferation. Consistently, it has been shown that cells cultured on nano-structured PDMS surfaces have higher proliferation and lower apoptosis rate [14].

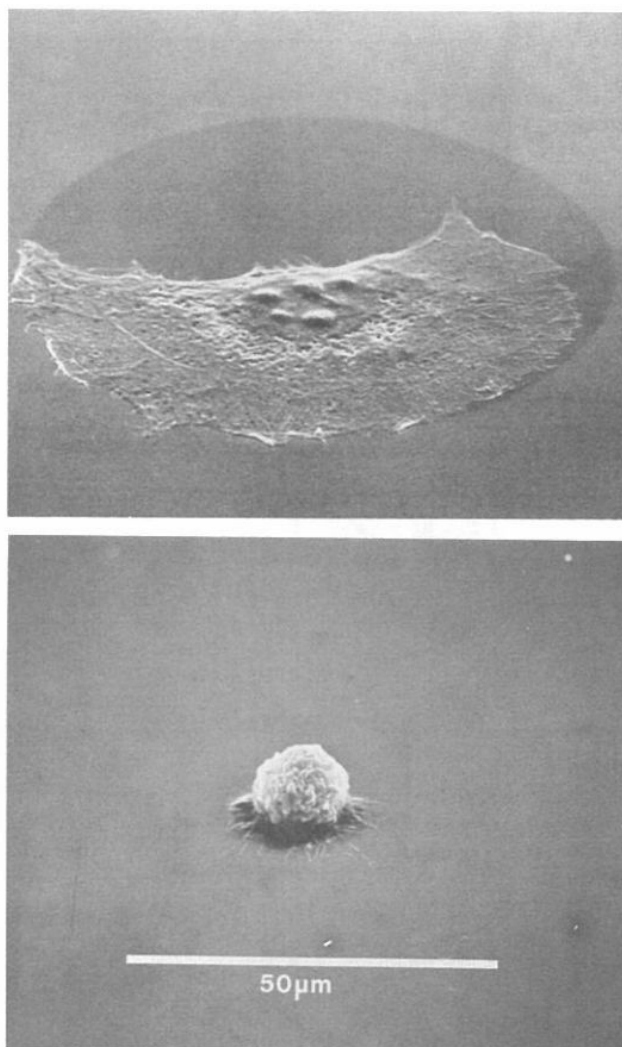


**Figure 1-3** Shapes Adopted by Cells on Islands. Scanning electron micrographs of 3T3 cells in contact with islands of the largest and smallest sizes used in these experiments. The cells were fixed 4 hr after seeding from a randomly growing culture. The volumes and shapes of these cells are variable; typical examples are shown. Islands occupied by single cells have been selected; up to 60 % of the islands are occupied by either more or less than one cell. Some shrinkage occurs during the process of preparation for electron microscopy. Scale = 50  $\mu\text{m}$ .

#### 1.1.4 Cell migration

Cell migration plays a central role in regulating cellular functions, including embryonic development, immune response, and wound healing process. Any error occurring during the cell migration process can lead to severe pathophysiological consequences, including tumor formation, vascular dysfunction, or malformation during the development of organisms. Nano- micro- fabrication technologies have provided powerful tools to study the migration of single or multiple cells, by controlling the adhesion areas or the topography of the ECM where cells can migrate on. It becomes clear that cell migration is mainly determined by two systems: intracellular signaling mechanism and extracellular physical/biochemical cues. The intracellular signaling mechanism includes the signals controlling the cell protrusion in the leading edge, integrin-mediated membrane adhesion to the substrate, formation and stabilization of attachments, and contraction and detachment from the substrate in the rear edge. Physical/biochemical cues are mainly related to the cellular microenvironment which includes chemical stimulation and physical topography [15-17]. In this section, we will focus on the regulation of cell migration directed by microenvironment cues. The lamellipodia-like protrusion of cells seeded on micro-patterned surface can be induced by EGF stimulation. Bailly *et al.* created vitronectin-patterned lines on the gold surface where MTLn3 cells were constrained to grow [18]. EGF can be clearly observed to stimulate lamellipodia extension out from the adhesive pattern toward the inert areas. Saadi *et al.* [19] developed a simple microfluidic device for generating stable concentration gradients of IL-8 in 2D and 3D environments. With this device, neutrophil chemotaxis and migration can be observed and monitored. Similar method was also developed by Jeon *et al.* [20]. The topography of ECM can also control cell migration through physical cues. Wood showed that mesenchymal fish cells cultured on different patterns on micro-fabricated quartz discs could predominantly align and migrate parallelly along the

long axis of the adhesive patterns after a few hours of culture [21]. These polarization and alignment effects can also be found in other cell types, including oligodendrocytes [22] and hippocampal neurons [23] and fibroblast [24]. This platform of applying nano- micro- fabrication technologies to create special microenvironment has proven to be a versatile and powerful tool for the study of cell migration. It provides a well-controlled cell culture environment in which cells can be observed in real time. Furthermore, it allows us to integrate both biophysical and biochemical factors, which is necessary in mimicking biological conditions as cells constantly receive environmental signals in both soluble and insoluble forms. Indeed, nano- micro- fabrication technique has been successfully applied for the study of cellular functions related to migration, such as adhesion on quasi three-dimensional cell microenvironment [25,26], and artificial mirco- nano- structures [27]. Hirschfeld-Warneken *et al.* [28] found that cells elongate themselves along the gradient on a substrate with a larger ligand distance (Figure 1-4). Theoretical calculation based on a one-dimensional continuum viscoelastic model is used to predict the migration speed of a single cell in response to a linear ligand density gradient across a solid substrate as a function of gradient slopes. The model predicts biphasic dependence between migration speed and gradient slope with a maximum speed at an intermediate gradient slope, above which the cell speed decreases with increasing slope [29].

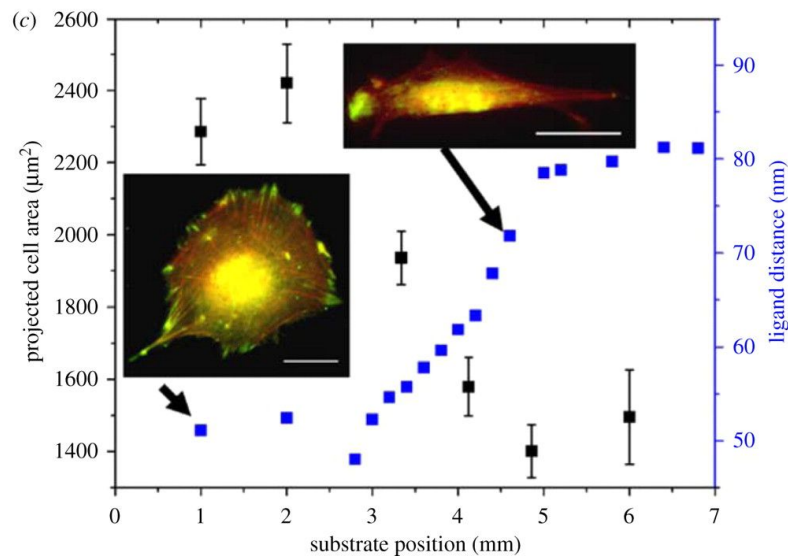
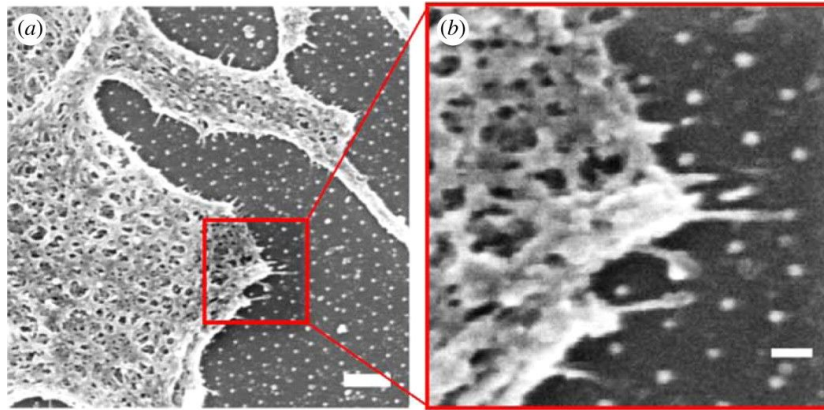


**Figure 1-4** Mc3t3 osteoblasts in contact with a biofunctionalized 80 nm pattern and exhibiting cell protrusions sensing the pattern. Scale bars, (a) 20  $\mu\text{m}$  and (b) 200 nm. (c) Projected cell area ( $\pm$ s.e.m.) as a function of substrate position. Insets: Mc3t3 osteoblasts after 23 h adherence on a homogeneously nanopatterned area with 50 nm c(-RGDfK-) patch spacing (left) and along the spacing gradient (right), respectively. Cells are immunostained for vinculin (green), and actin is visualized using TRITC (6-tetramethylrhodamine isothiocyanate)-phalloidin (red). Scale bars: 20  $\mu\text{m}$  (left); 200 nm (right).

## 1.2 3-D fabrication techniques

Apparently, cells *in vivo* are subjected to environment in three dimensions. In addition, cells *in vivo* tightly interact with the surrounding environment which contains various physical and chemical cues. As such, the cell environment *in vivo* is more complicated than what can be generated in 2D tissue culture dishes. Indeed, the cellular functions and structure under 3D environment demonstrated features significantly different from 2D cultured cells [30,31]. Therefore, three-dimensional techniques are becoming more and more important in cell biology to generate microenvironment mimicking the physiological condition closer than that of two-dimensional devices and patterns. These three-dimensional techniques can offer powerful tools to study the different mechanisms of cellular behaviors and functions under the physiological and pathological conditions. While not the mainstream activities, three-dimensional devices can also be generated by soft lithography at micron scale and by electrospinning at nano- scale. In this part, we introduce other methods aimed to specifically create three dimensional patterns or devices for the studies of cell biology. Giang *et al.* reported a method using a mold composed of deep reactive ion etched (DRIE) trenches to get concave cavities in three-dimensional structures [32]. In this case, partially degassed PDMS pre-polymer was applied to a hydrophobic mold with a high curing temperature to create the desired patterns. Ice-lithography was another method newly developed [33]. This method utilizes patterned water droplets created by micro- scale plasma activated templates. The pre-cured PDMS is applied to encapsulate patterned water. The space occupied by water can then formulate the 3D cavities. Joong Park *et al.* further improved this technique by utilizing DMSO as the liquid to occupy the space within PDMS [34]. This approach allows easier control of the size and shape of the solidified template. With this method, multiple concave micro-wells can be conveniently generated to successfully entrap cells. Therefore, ice-lithography has potential biological and biomedical applications in areas such as the fabrication of cell docking devices.

Electroplating is a method to obtain a durable metal replication master for cylindrical microchannels [35]. The master dimension can be controlled by the electroplating time and swapping power. As such, PDMS micro-channels can be obtained without soft lithography. Chan-Park *et al.* have demonstrated that concave or convex micron patterns can be generated by gas expansion [36]. In this case, prepolymer substances trapping argon gas in the microcavities can be polymerized by applying UV lights to develop 3D PDMS molds. These micro-channels can be, subsequently, applied to study cell biology. Mina Okochi *et al.* showed that a three-dimensional (3D) cell culture system has been fabricated using a magnetic force based cell patterning method, demonstrating a facile approach for the analysis of invasive capacity of BALB/3T3/*v-src* using an magnetic force and magnetite nanoparticles (Figure 1-5) [37].

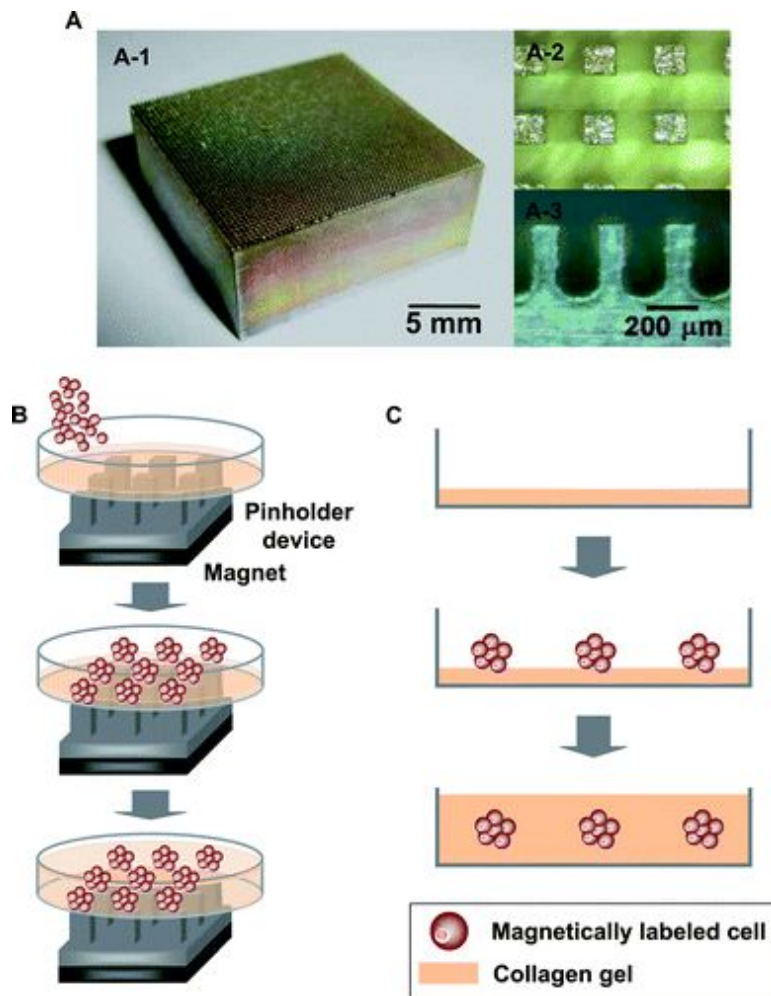


**Figure 1-5** (A) Photographs of the pin holder device for the magnetic cell patterning. A photograph of a magnetic soft iron (A-1) that contains more than 6000 square pillars (100  $\mu\text{m}$  width, 100  $\mu\text{m}$  length, 300  $\mu\text{m}$  height) with center-to-center distance of 250  $\mu\text{m}$  (A-2, A-3). (B) Schematic diagram for fabrication of the 3D cell culture array using magnetic force and a pin holder device. The magnetically labeled cells were seeded into a culture dish with a thin layer of collagen gel and patterned into an array. The patterned cells were further embedded with collagen gel to construct the 3D cell array. (C) Side view of the scheme for the magnetic cell patterning in 3D.

### 1.3 Nano- scale structure fabrication

Various nano-structured fabrication techniques other than electrospinning have achieved tremendous progress in applying to cell biology during last decade. Nano-structured materials have many unique properties: (i) large fraction of surface and high ratio of surface area to volume; (ii) high surface energy; (iii) precise spatial confinement; (iv) reduced imperfections. These properties do not exist in the corresponding bulk materials. A “dip-pen” nanolithography (DPN) in a direct-write fashion was invented in 1999 [38]. In brief, an atomic force microscope tip was used to deliver collections of molecules in a positive printing mode. The results indicate that alkanethiols can be printed in lines on a gold thin film with 30 nm resolution, analogous to what a dip pen can do. During the past 10 years since this technique was invented, DPN has been developed as a general method for generating functional surface-patterns on the sub-100 nm scale, with the chemical composition and structure precisely tailored by an atomic force microscope. For example, Lee *et al.* [39] applied DPN to fabricate nanoarrays of ECM domains of fibronectin on a thin-film gold surface. 3T3 Swiss fibroblast cells were successfully seeded onto these fabricated patterns consisting of nanoarrays. Therefore, DPN can provide the opportunity to study a variety of surface-mediated biological processes at subcellular levels. Electron beam fabrication is another method which can create nano-patterns with different materials. Indeed, a resolution of 10 nm was achieved in 1976 [40] and Yasin *et al.* [41] successfully fabricated <5 nm poly(methylmethacrylate)-resist lines utilizing a developer assisted by an ultrasonic approach. Other nano-fabrication systems, like nano-imprint lithography (Figure 1-6) [42], nanoshaving, and scanning probe microscopy [43,44], have also been developed for studies in cell biology. And in the past decade, there has been tremendous interest in exploring the potency of biomimetic fibers in tissue engineering, and several techniques originally developed for different purposes have been used for this application (Table 1-1) [45].

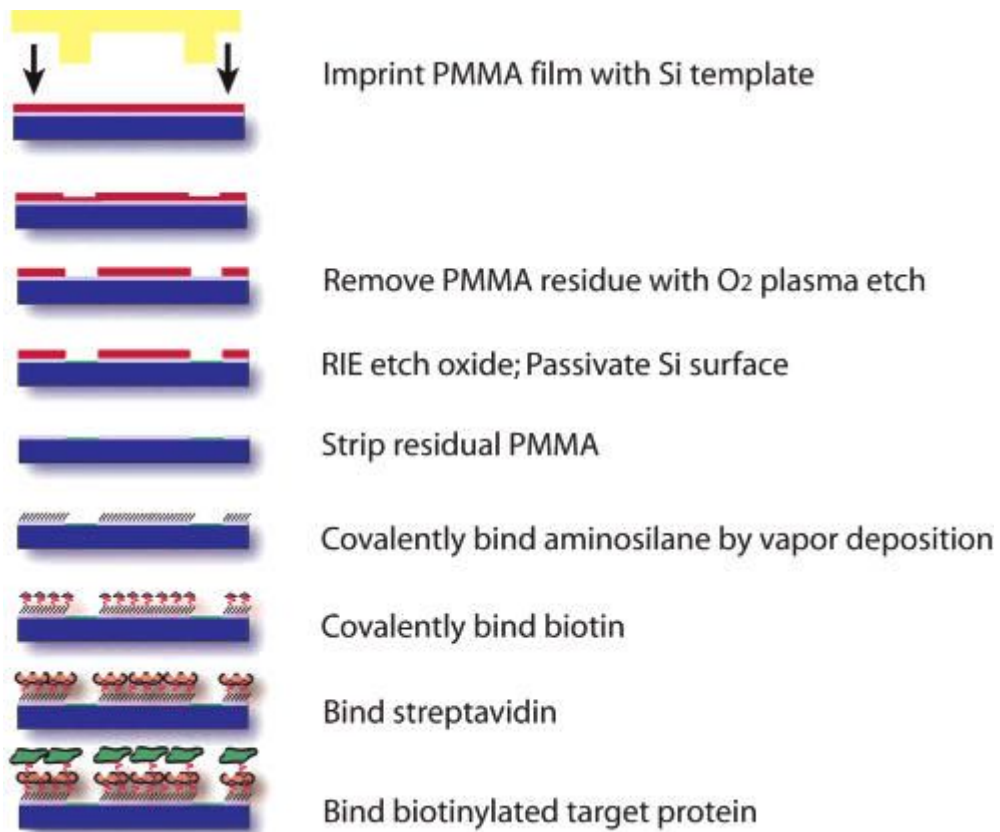


**Figure 1-6** Process flow diagram of substrate patterning and protein immobilization. Spin-coated PMMA polymer is patterned by NIL. Exposed SiO<sub>2</sub> regions are etched and a passivating (CF<sub>x</sub>)<sub>n</sub> polymer ( $x = 1$  or  $2$ ,  $n =$  number of monomer subunits, monomer MW = 31 or 50) is deposited during a CHF<sub>3</sub> RIE procedure. Residual PMMA is stripped away with acetone, exposing the underlying SiO<sub>2</sub> in the “patterned regions.” An aminosilane monolayer is covalently attached to the exposed “patterned regions”. Biotin-succinimidyl ester is then covalently linked to the primary amine of the aminosilane layer, and streptavidin is bound to the biotin layer. Finally, the biotinylated target protein is bound to the streptavidin layer.

**Table 1-1** Mimicking ECM components to create cell microenvironment

<b>Natural component</b>	<b>Method</b>	<b>Material used</b>	<b>Role</b>
Fibres: collagens, elastins	Electrospinning	Carbon, PLA, PGA, PLGA, polycaprolactone, polydioxanone, chitosan	3D cell scaffolding, promote adhesion
	Self-assembly	Peptide amphiphile	3D cell scaffolding, promote adhesion, differentiation
	Nanopatterning	PEG, poly(ester amide)	Induce morphogenesis
Adhesion proteins: laminin, fibronectin	Conjugation of adhesion motif to the matrix backbone	RGD and IKVAV amino acid sequences	Promote cell adhesion to matrices
Proteoglycans: heparin sulphate	Sulphating matrix backbone	Alginate-sulphate, perlecan, sulphated chitosan	Control the release and presentation of growth factors and cytokines
Minerals: hydroxyapatite		Hydroxyapatite	Induce osteogenesis and mineralization

## 1.4 Soft lithography for micro- fabrication

Soft lithography is the keystone of a set of techniques for non-photolithographic fabrication, which is mainly based on the elastometric stamp to mold desirable two- or three dimensional nano- micro- scale patterns on different substrata [18,25,46,47]. In general, it includes several major techniques: microcontact printing, replica molding, microtransfer molding micromolding, and solvent-assisted micromolding. Due to its low cost and easy fabrication characteristics, it has been widely applied in biology studies during the past decade. Soft lithography process is usually divided into two parts: (1) create and fabricate the elastomeric elements; (2) apply these elements to release the desirable geometrical patterns onto substrata. Due to the advantages of soft lithography, e.g., it can be fabricated at low costs and cells constrained on a certain location with desirable shapes, there are a lot of applications of soft lithography in cell biology, such as creating patterned cell culture and co-culture systems, manipulating topography of ECM, and imposing cells with gradient chemical stimulation [46]. SAM is not the only way to obtain soft lithography patterning surface. Ma *et al.* created micro-patterns via micro-contact printing method [48,49]. With this method, the patterns created by comb polymer were quite stable. While the micro-contrast printing technology has been exceedingly useful and applied in cell biological studies, there is a practical limit in the resolution of the created patterns, typically at the scale of 100 - 200 nm [50]. This is mainly due to the surface diffusion of the molecular inks and the molecular disorder at the pattern edges. Microfluidics system is another major application of soft lithography technology. Microfluidics systems are typically applied for the screening purpose of protein crystallization, bio-analysis, synthesis, examination, and manipulation of samples consisting of a single or multiple cells, and drug development. Different kinds of stimuli (chemical molecules or mechanic stimulation) can also be delivered to cells by this system in microfluidic channels at subcellular levels. For example,

Takayama *et al.* reported the application of multiple laminar streams in a microfluidic channel to deliver membrane permeable molecules to highlight subcellular microdomains [51]. This method can also be readily applied for the potential non-invasive visualizing, probing, and manipulating the cellular metabolic and structural machinery. Shiu *et al.* have created a three dimensional microfluidic system which can deliver cells to an adhesive tissue culture surface patterned in concentric squares [3]. Different cell types, e.g., bovine capillary endothelial and human bladder cancer cells, can be deposited at different squares. This system can also allow the deposition of the same type of cells on defined areas where each area can be treated with different substances. Folch & Toner [52] have created cellular micropatterns on a variety of biocompatible polymers and heterogeneous surfaces by microfluidic patterning of physisorbed ECM templates (Figure 1-7).

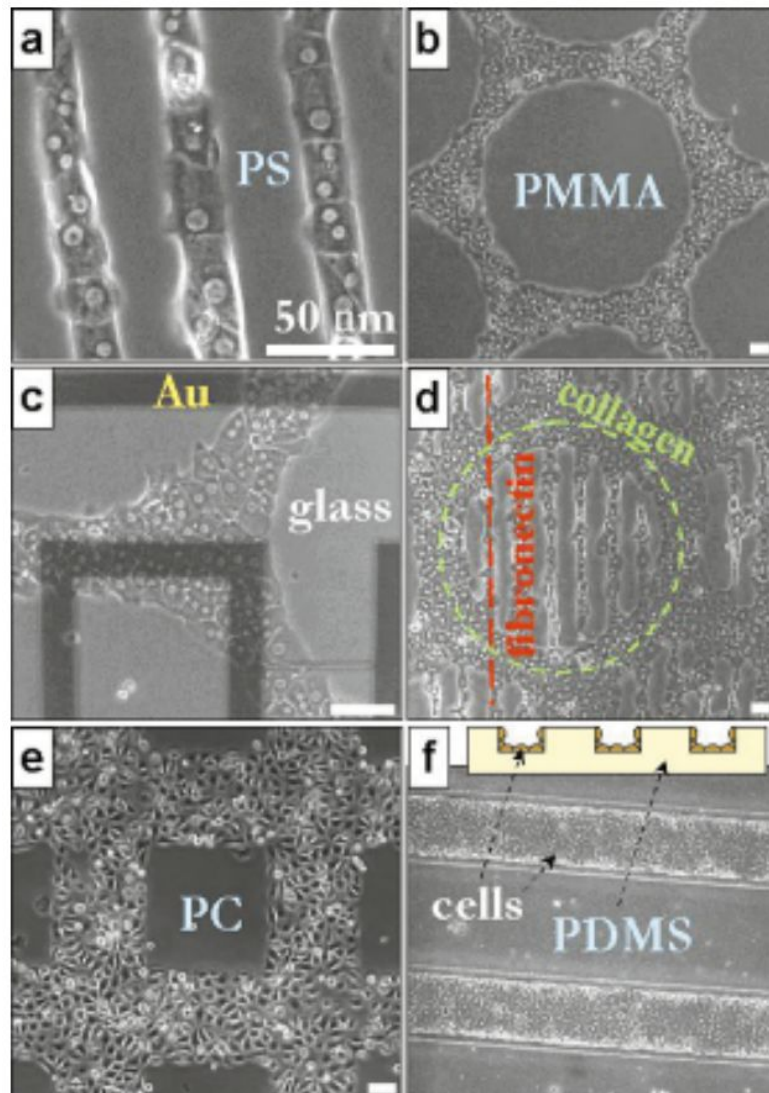


**Figure 1-7** Cellular micropatterns on templates of physisorbed ECM proteins on biocompatible materials. The templates were created by microfluidic patterning on polystyrene (a), poly(methyl methacrylate) (b), a gold microelectrode pattern on glass (c), an underlying protein micropattern on polystyrene (d), and microtextured PDMS (e). The template, made of collagen (a, c-f) or fibronectin (b, d), induced the selective attachment and spreading of hepatocytes (a-d, f) or keratinocytes (e).

## 1.5 Summary

Nano- micro- fabrication techniques have provided scientists with powerful tools to control cellular microenvironment, mimicking both the physiological and pathological environment. The control of cellular microenvironment, both physically and biochemically, can allow the study of fundamental molecular mechanisms regulating vital cellular functions. In particular, the regulation of stem cell differentiation by microenvironment can not only advance our understanding of the mechanism of stem cell differentiation, but also facilitate the development of new methods to grow biocompatible artificial organs/tissues to replace the dysfunctional counter parts *in vivo*. Indeed, Hartman *et al.* [53] have recently shown that cancer cells on three-dimensional environment were suitable models for the development and testing of anti-neoplastic drugs. Nano- micro- technologies have also been applied in the clinic studies [54,55] medical assays [56,57], tissue engineering [26,58-60], and drug development [61]. While all these applications have had significant impact on different fields, they are not discussed in detail because this review article is mainly focused on the studies integrating nano- micro- fabrication technologies to elucidate the molecular mechanism of signaling transduction in cell biology. For the future research activities, we expect more work on the integration of nano- micro- technology and molecular imaging in live cells to elucidate the detailed molecular mechanisms on how cells perceive the nano- micro- environmental cues and coordinate the signals cascades for appropriate responses. This will further our in-depth understanding of the cell-environment interaction and help the development of new technologies/reagents against related diseases.

## **Chapter 2 Cell with Microstructure**

### **Cell Motility Regulation on a Stepped Micro Pillar Array Device (SMPAD) with a Discrete Stiffness Gradient**

In this chapter, we show a new variation of the microfabricated polymeric pillar array platform that can decouple the stiffness gradient from the focal adhesion area of a cell. This goal is achieved via a “stepped” micro pillar array device (SMPAD) in which the contact area with a cell was kept constant while the diameter of the pillar bodies was altered to attain the proper mechanical stiffness. Using this simple platform, which produces a purely physical stimulus, we observed that various types of cell behavior are affected by the mechanical stimulus of the environment. We also demonstrated directed cell migration guided by a discrete rigidity gradient by varying stiffness.

## 2.1 Introduction

Cells explore their environment and react to various stimuli by reforming intracellular structures, such as actin filaments, to respond to their surroundings [62-67]. The mechanical properties of the environment can influence many aspects of the cell life cycle [68,69]. When cells are plated onto a planar substrate, the morphology and behaviour of the cell depends on the stiffness of this substrate [70-72]. If the substrate is soft, aggregates of adhesion molecules remain small and transitory. When the substrate is stiff, a clear network of contractile stress fibres develops, and strong focal adhesions anchoring the cell to the substrate are observed [5,7,73-78]. Cells sense the elastic modulus, interpreted as environmental rigidity, by deforming their surroundings through cell-generated forces. In particular, the elasticity of the substrate in contact with the cell can influence the direction of cell migration. This directional cell migration guided by stiffness gradients, called durotaxis, was originally observed in fibroblasts migrating across a soft-to-stiff interface of planar two-dimensional (2D) surfaces [79-81]. This prior work utilized numerous methods to create polymer-based substrates with varying rigidity [7,70,71,74]. However, maintaining accurate control over the arrangement of substrate stiffness, such as the amount and direction of the gradient, is challenging. Thus, many investigators have sought methods to increase the dimensional complexity of *in vitro* migratory environments.

Micro-scale polymeric pillar arrays have commonly been used as cell force detectors [82,83]. This type of pillar array has been recently used to study cell movement and shape by various methods, including the application of a gradient of rigidity provided by varying pillar diameters [84]. However, the adhesion area of the extracellular matrix (ECM) has also varied across different pillars because of changes in diameter. Variation in adhesion area is one of the essential cues associated with the formation of focal adhesions and may affect cell migration and

proliferation [85,86]; thus, adhesion area must be decoupled from the effects of a pure rigidity gradient.

In Figure 2-1, we present a “stepped” micro pillar array device (SMPAD) that can offer the rigidity gradient in a discrete fashion without varying the adhesion area. This idea was realized by using a widespread photolithography technology: double-step SU-8 mold fabrication. Polydimethylsiloxane (PDMS) was used to fabricate the double-layered polymeric pillar substrate to form three-dimensional (3D) structures because it is biocompatible and possesses unique mechanical properties. To create stiffness differences, the diameter of the bottom layer of fabricated pillars is tuned while the top layer is maintained uniformly. The different bending forces for each pillar achieved by varying the pillar diameter can affect cellular motion and behavior when attached to the pillar array, similar to an environmental stiffness gradient. This stepped pillar substrate can be used to monitor cellular behavior on various types of substrates providing not only a soft-to-stiff interface (Figure 1(a)) but also varying stiffness gradient strengths (Figure 1(d), (e)). In this study, we observed that major cellular reactions, such as cell morphology, viability, and velocity, were affected by the mechanical stimulus from the SMPAD. Especially, NIH3T3 cell migration was demonstrated across the various rigidity gradient increments. We found that the stiffness gradient must be larger than a certain value to initiate a directional and consistent migration. In addition, in the environment with the highest variation in stiffness, cells reached maximum velocity in their migrating motion. Our results clearly demonstrate that cells prefer a stiffer environment, and a correlation between cell velocity and stiffness gradient strength was observed.

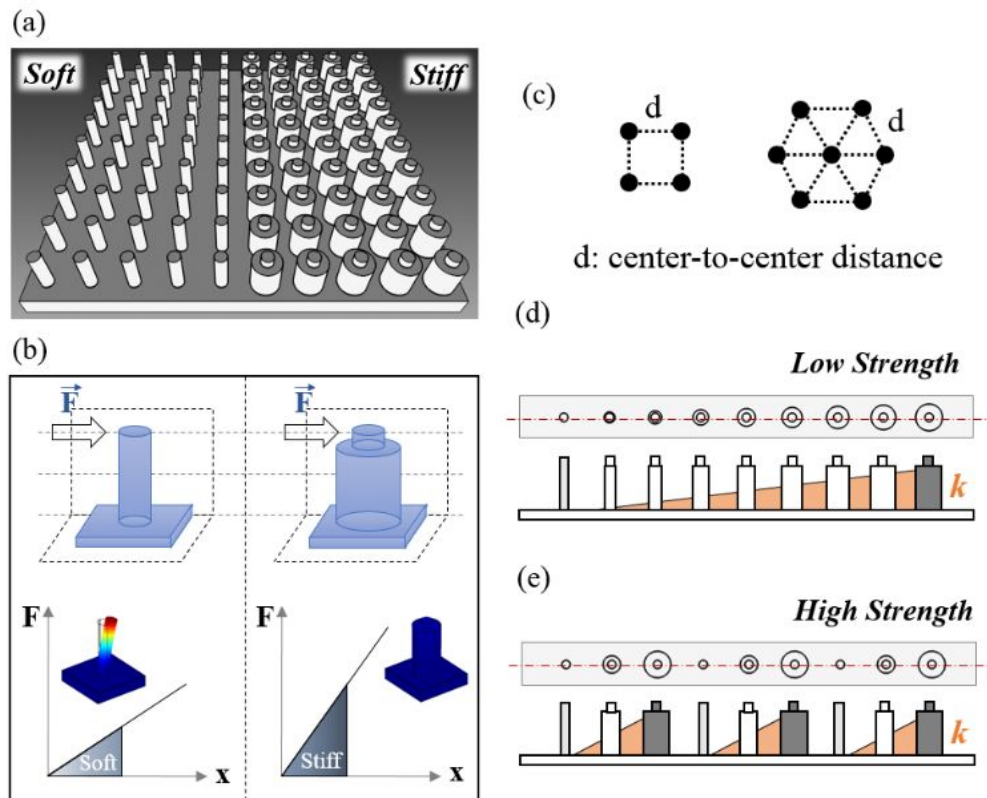


**Figure 2-1** Illustrations of the Stepped Micro Pillar Array Device (SMPAD) presented here. An illustration of a binary type of SMPAD with a soft pillar array (left) and stiff pillar array (right) (a). Plots of the force and deformation relationship produced on a soft (left) and stiff (right) type of SMPAD (b). The spring constant is proportional to the bottom pillar diameter of the SMPAD ( $F=kx$ , where  $k$  is the spring constant). Illustration of the pillar arrangement (c). The black dot represents a single SMPAD, and the dashed line is the distance between pillars in the SMPAD ( $d=10\ \mu\text{m}$ ). Square (left) and hexagonal (right) arrangements were used here. Side view of gradient types of the SMPAD (d) and (e). Of note, there is a slower increase in the bottom pillar diameter toward the right in the low-strength SMPAD (d) than in the high-strength SMPAD (e).

## 2.2 Materials and Methods

### 2.2.1 Geometric considerations

A polymeric micro-scaled pillar behaves similar to a spring, such that the deflection is directly proportional to the force applied by the attached cells [87]. Each pillar was treated as a cylindrical cantilever beam, with one end fixed to the substrate and the other end free. We used two types of pillar array configurations, which formed square and hexagonal arrangements, with the center-to-center distance ( $d$ ) fixed at 10  $\mu\text{m}$  to provide constant contact guidance. The relationship between the force,  $F$ , and the free end displacement,  $x$ , for a cylindrical beam can be determined using the theory of cantilever beam bending (Euler–Bernoulli Beam Theory) [88-91]:

$$F = Kx$$

$$K = \frac{3\pi ED}{64L^3}$$

where  $K$  is the spring constant,  $E$  is the Young's modulus, and  $D$  and  $L$  are the diameter and height of the pillar, respectively. According to the above equation, the spring constant  $K$  can be modified by varying the size of the pillar. To calculate the spring constant of the stepped pillar in our case, we divided each pillar into two sections, the top and bottom pillar:

$$\frac{1}{K} = \frac{1}{K_a} + \frac{1}{K_b}, (D_a \neq D_b)$$

In the above formula,  $K_a$  and  $K_b$  are the spring constants, and  $D_a$  and  $D_b$  are the diameter for the top and bottom portions, respectively. Given the existence of stiffness variation between tissues, we initially considered the soft-to-stiff substrate condition of the pillar array, which have different bottom pillar diameters to produce

a binary stiffness. We designed the array such that the soft pillar had a 2  $\mu\text{m}$  bottom diameter and the stiff pillar had a 7  $\mu\text{m}$  bottom diameter, and the total height of the whole pillars was fixed at 10  $\mu\text{m}$ . The calculated spring constants were 2.3  $\text{nN}/\mu\text{m}$  for the soft pillar and 206.4  $\text{nN}/\mu\text{m}$  for the stiff pillar. We then considered the other type of substrate with gradually increasing stiffness. In this case, bottom pillar diameters were increased continuously over the course of the substrates from 2  $\mu\text{m}$  to 7  $\mu\text{m}$ , with a total pillar height of 7  $\mu\text{m}$  and center-to-center spacing of 10  $\mu\text{m}$  along the axis of increasing pillar diameter. To monitor the effects of stiffness strength on cellular behavior, three types of stiffness gradients were constructed, corresponding to low gradient strength ( $\Delta K = 0.5 \text{ nN}/\mu\text{m}$ ), medium gradient strength ( $\Delta K = 5 \text{ nN}/\mu\text{m}$ ) and high gradient strength ( $\Delta K = 50 \text{ nN}/\mu\text{m}$ ). The low gradient strength substrate included diameters ranging from 2 to 3  $\mu\text{m}$ , corresponding to a physiologically relevant stiffness of 6.8 to 72  $\text{nN}/\mu\text{m}$ . The medium gradient strength substrate was designed with diameters ranging from 2 to 5  $\mu\text{m}$ , corresponding to a pillar stiffness of approximately 6.8 to 149  $\text{nN}/\mu\text{m}$ . The high gradient strength substrate included diameters ranging from 2 to 7  $\mu\text{m}$ , corresponding to a pathologically relevant stiffness of 6.8 to 267  $\text{nN}/\mu\text{m}$ .

### **2.2.2 Fabrication process**

To achieve a stepped pillar structure, we used the general photolithography processes described in Figure 2-2. SMPAD fabrication begins with a double-exposure patterning of SU-8 photoresist (MicroChem, USA). SU-8 is spun onto the wafer yielding a 10  $\mu\text{m}$  thick film. This SU-8 film is soft baked at 65  $^{\circ}\text{C}$  for 1 min and then 95  $^{\circ}\text{C}$  for 2 min on a hot plate. Next, as shown in Figure 2-2(c), the SU-8 film is exposed to UV light (365 nm) with a chromium photomask of the bottom pillar pattern in a mask aligner (Karl Suss, Germany). After exposure, an additional layer is coated, baked and exposed again as a top pillar layer with the thickness of 2  $\mu\text{m}$  (Figure 2-2(b)). Then, the wafer is post-exposure baked with the same

temperature conditions as the soft-baked step. After pattern development (Figure 2-2(e)), the surface of the SU-8 master must be passivated with (tridecafluoro-1,1,2,2-tetrahydrooctyl)-1-trichlorosilane (Sigma Aldrich, Korea) to prevent the master from detaching from the wafer. For preparing the negative mold, PDMS is mixed at a 10:1 base polymer to curing agent ratio and allowed to degas for 2 h. Then, it is poured onto the SU-8 master and cured in a 110°C convection oven for 20 min. The polymer is allowed to cool for 10 min, and the master is gently peeled out of the negative mold (Figure 2-2(f)). The surface of the negative mold is again passivated with a fluorinated silane to prevent the liquid PDMS from permanently bonding to the PDMS negative mold during the second casting. As shown in Figure 2-2(g), a thin layer of PDMS is applied to the negative mold, and then, a glass slide or cover glass pretreated in a plasma etcher is placed on top to sandwich the film. The mold is placed in a 70°C oven and cured overnight to ensure maximum crosslinking of the PDMS polymer. The SMPAD bound to the top cover glass or slide is then peeled away from the negative mold (Figure 2-2(h)).

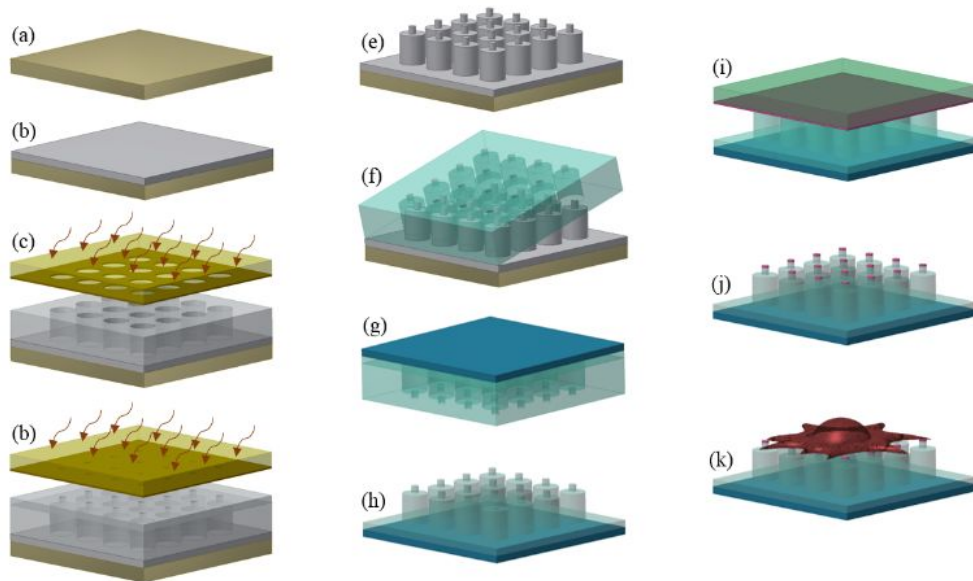


**Figure 2-2** Process flow for the SMPAD fabrication. A bare silicon wafer was prepared after piranha cleaning and dehydration processes (a). SU-8 2002 spin coating and flood exposure for the SMPAD base (b). SU-8 2010 spin coating and exposure for the bottom portion of the SMPAD (c). SU-8 2002 spin coating and exposure for the top portion of the SMPAD (d). Developing process for the positive SMPAD master (e). PDMS casting for the negative mold (f). A cover glass was used to press inter-filling PDMS and generate the thin SMPAD substrate (g). Completed SMPAD substrate (h). Fibronectin coating of the top of the SMPAD using a contact printing method (i). Prepared ECM coated SMPAD (j). Adherent animal cells were seeded and cultured on the prepared SMPAD (k).

### **2.2.3 Data acquisition**

Time-lapse imaging of SMPADs was performed with an inverted microscope (Nikon, Japan) maintained at 37°C. Images were recorded using a 40X objective (0.6 NA, air), and the temporal variation in the position of pillars was collected over a period of time. The position of each pillar in each frame was determined using the particle tracking plug-in for ImageJ software (NIH), which employs an autocorrelation algorithm. In all cases, pillars were tracked before the cell spread over them to establish an equilibrium (zero force) position. The time-dependent displacement of a given pillar was then calculated by subtracting its initial position (corresponding to zero force) from the position in a given frame.

### **2.2.4 Cell preparation**

NIH3T3, C2C12, and HeLa cells were maintained in Dulbecco's modified Eagle's medium containing 10% fetal bovine serum and 1% penicillin-streptomycin (all from GIBCO, USA) at 37 °C and 5% CO<sub>2</sub>. Oxygen plasma was used to render the SMPAD surface hydrophilic for enhancing the adhesion of the fibronectin (Sigma Aldrich, Korea) as the ECM. As shown in Figure 2(i) and (j), the ECM was applied to the top pillar surface by stamping a fibronectin coating onto a flat PDMS substrate. The remaining areas of the pillar and bottom substrate were blocked with 2% Pluronic F127 (BASF, USA) to prevent interference with cell behavior as a result of unnecessary attachment, as illustrated in Figure 2(k). To monitor migratory cell behavior in response to the strength of the stiffness gradient in real time, cells on various types of SMPAD were cultured in a portable incubator (IC-L-10, Chamlide, Korea) that can maintain constant temperature, humidity, and CO<sub>2</sub>. Images were captured every 3 min for up to 24 h.

### **2.2.5 Immunofluorescence staining**

The distribution of fibronectin adsorbed on the PDMS substrate was examined using immunofluorescence. After the coated fibronectin was blocked with blocking solution (3% bovine serum albumin (BSA) in 1X phosphate buffered saline (PBS)) for 30 min, primary antibody was added in solution for 1 h. Then, the PDMS surface was rinsed several times with washing buffer (1X PBS containing 0.05% Tween-20). To quantify the fibronectin distribution, a secondary antibody conjugated with fluorescein-isothiocyanate (FITC, Thermo Scientific, USA) was used. Fibronectin distribution on the PDMS substrate was analyzed using image processing software (NIS Element, Nikon, Japan). Actin filaments within the cell were labeled with fluorescent conjugated anti-actin filament (Millipore, USA) to investigate the effect of substrate stiffness on cell structure and morphology. Cells were fixed with 4% paraformaldehyde (Sigma Aldrich, Korea) for 15-20 min at room temperature and washed several times with washing buffer. To improve the permeability of cell membranes, 0.1% Triton X-100 (Sigma Aldrich, Korea) in PBS was used for 1-5 min. Cells were blocked for 30 min in blocking solution, and fluorescent conjugated anti-actin filament solution was added to the cells. Then, the cells were incubated for 1 h. Cell shape was photographed using confocal laser scanning microscopy (CLSM, Zeiss, USA). Nuclei were stained with 4',6-diamidino-2-phenylindole (DAPI, Millipore, USA) for 1-5 min, followed by washing the cells three times with 1X washing buffer.

### **2.2.6 Quantification**

Data are expressed as the mean  $\pm$  standard deviation. Statistical analyses were conducted using statistical software (SAS 9.4, USA). Differences were considered significant at  $P < 0.05$ .

## **2.3 Results**

### **2.3.1 SMPAD characterization**

The physical properties of the fabricated SMPAD were investigated using scanning electron microscopy (SEM) and atomic force microscopy (AFM). Figure 2-3(a) shows the binary stiffness version of the SMPAD, which generates soft-to-stiff substrate conditions in the pillar array. In this image, a soft pillar has a 2  $\mu\text{m}$  bottom diameter, and a stiff pillar has a 7  $\mu\text{m}$  bottom diameter; the height of whole pillars was fixed at 10  $\mu\text{m}$ . We also designed a SMPAD stiffness gradient type in which rigidity varies unidirectionally in the substrate. The center-to-center distance was fixed at 10  $\mu\text{m}$  in Figure 2-3(b). Chemical stimuli, such as the ECM, can trigger cell migration. Our SMPAD offers a uniform amount of an ECM environment on its top surface because of its unique double-stepped design. To verify the amount of ECM on the top surface, we used FITC-labeled fibronectin absorbed with flat PDMS and stamped it onto the pillar array using a microcontact printing method. Figure 2-3(c) shows regularly distributed green circular patterns that depict the stamped fibronectin of the SMPAD tops, and the yellow line depicts the fibronectin signal intensity. Notably, this fluorescence image depicts circular shape and regular spacing between the pillars. These images demonstrate that the fabricated polymeric pillar array only generates physical stimulus to the cells regarding stiffness differences without any chemical variation. After seeding cells onto our platform, we precisely investigated cell attachment by taking optical and confocal microscopic images, as shown in Figure 2-3(d) and (e). Cell fixation was performed to obtain scanning electron microscopic images, and these images revealed that cells were adhered onto the SMPAD and pulled them with high tensile forces (Figure 2-3(f)).

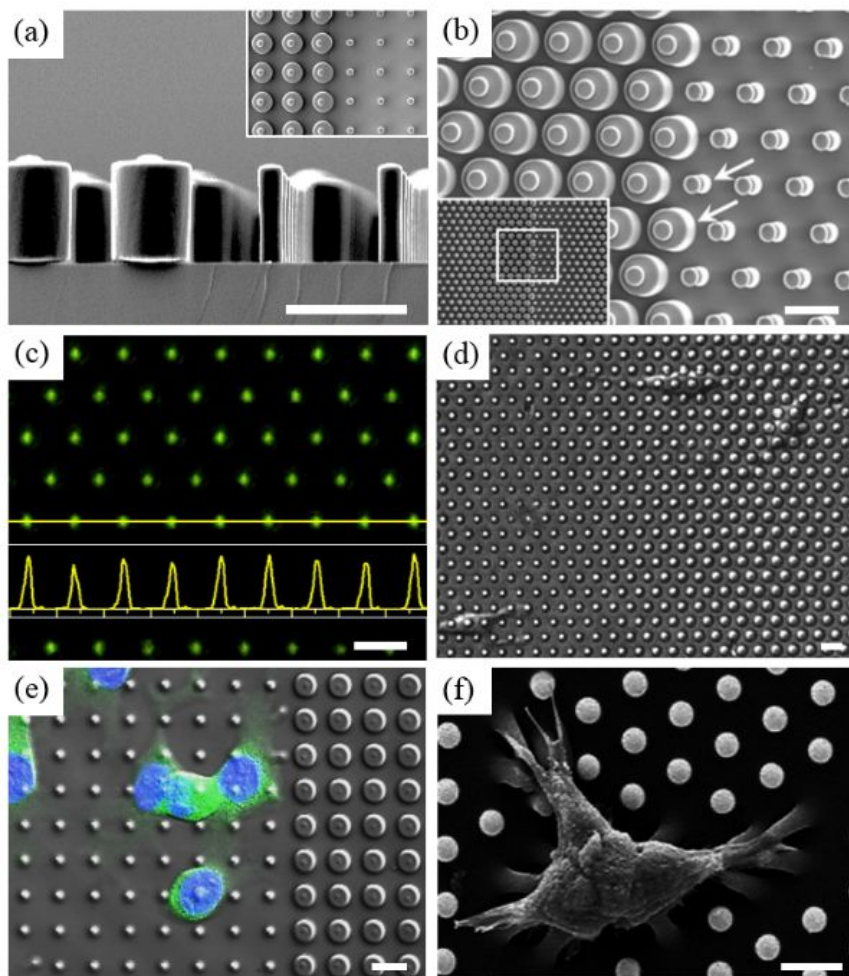


**Figure 2-3** Micrographs of SMPAD. SEM images of the positive SU-8 SMPAD master, which has a binary stiffness substrate (a), and the prepared polymeric SMPAD with stiffness gradients (b). Fluorescence image visualizing fibronectin absorption on SMPAD (c). Green dots represent printed fibronectin, and yellow curves represent protein intensity. Cell attachment on the SMPAD 3 h after cell seeding (d)-(f). Images were obtained by optical microscopy (d), confocal microscopy, and SEM (f). Scale bar, 10  $\mu\text{m}$ .

### 2.3.2 Analysis of SMPAD stiffness

In this study, we analyzed the stiffness of the SMPAD using an AFM. To obtain spring constant of SMPAD pillar, the AFM cantilever touches the free end of the pillar and applies a force of known value. To simplify the analysis, we assumed that our double-stepped pillars have uniform material properties such that the deflection is equivalent to the corresponding force divided by the spring constant. Figure 2-4 shows a force-displacement relationship obtained from AFM data. The straight line shows the linear relationship between the applied forces and AFM cantilever beam displacement which represents spring constant. Substrate stiffness was measured by applying force using the AFM against a glass substrate, and a similar force range on the PDMS substrate (Figure 2-4(a)). In case of SMPAD pillars, we obtained several values of spring constant according to their bottom diameter. The AFM test results of three types of pillar array with different bottom diameters are illustrated in Figure 2-4(b).

The measured spring constant of the binary and gradient types of substrates with AFM measurement is illustrated in Figure 2-5(a) and (b). From our previous research, we obtained the Young's modulus of PDMS as measured by AFM by acquiring the force-displacement curve and performing calculations using the Hertz model [92]. The measured elastic modulus of PDMS was calculated as  $\sim 1$  MPa. The black squares represent the calculated values of the spring constant according to the cantilever beam bending formula and the obtained Young's modulus, and the red circles represent real values measured by the AFM. For these results, we were able to measure only a selection of SMPADs using more than 10 samples because accurately locating an AFM tip on the correct spot of the SMPAD is extremely difficult. Regardless, we obtained reasonable values for the spring constant of SMPADs compared with the calculated values.

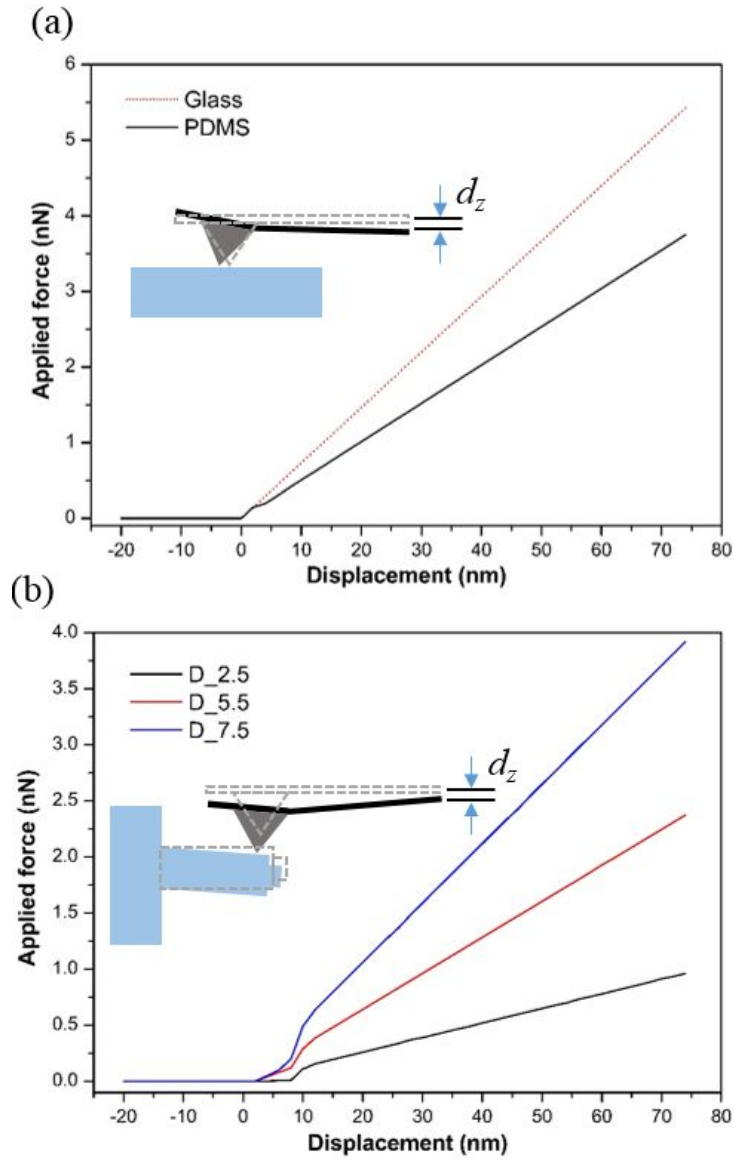


**Figure 2-4** Force and displacement plots using AFM. The force and z-displacement relationship of the AFM cantilever beam while applying forces on glass and PDMS substrate (a). SMPAD pillars with different bottom diameters (2.5, 5.5, and 7.5  $\mu\text{m}$ ) were also tested to obtain the force-displacement characteristics of the AFM cantilever (b).

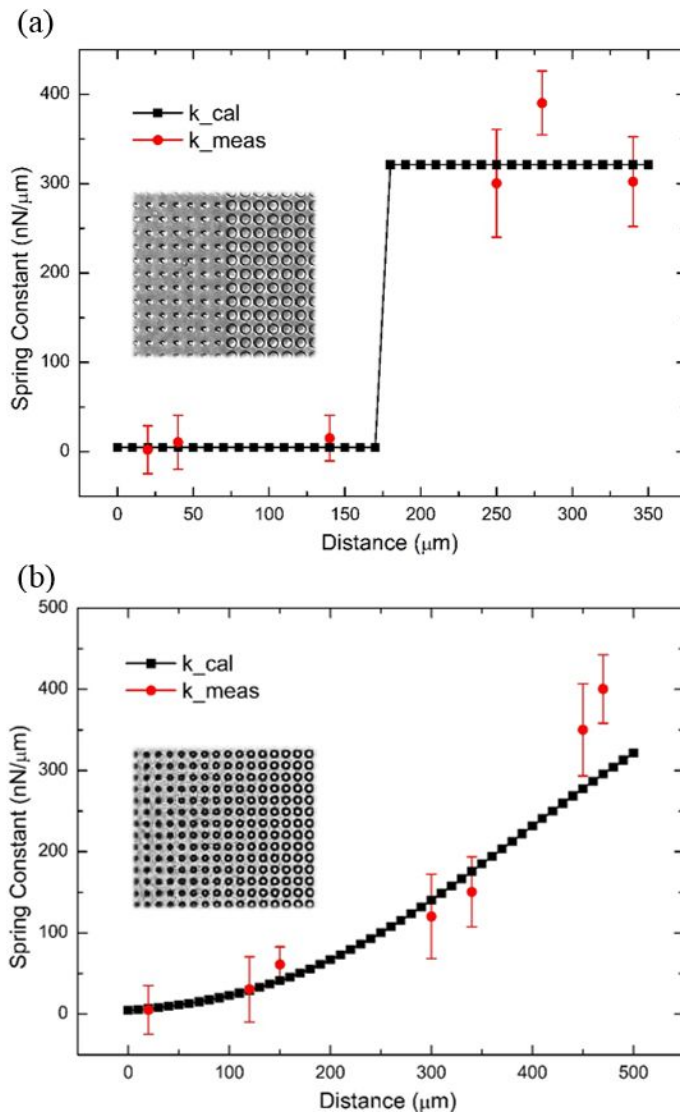


**Figure 2-5** Spring constant in the x-direction. Calculated values using the formula presented here are illustrated by black dots, and the values measured by the AFM cantilever tip are shown as red dots. The measured spring constant primarily followed the calculated values; a rapid increase between the soft and stiff types of SMPAD was observed (a). The gradually increasing spring constant with the SMPAD gradient type is shown in (b). ( $n=5$ ).

### **2.3.3 Cell morphology on the soft and stiff pillar array**

Prior to testing the cell responses on SMPAD surfaces with binary stiffness, cell morphology was investigated on both stiff and soft SMPAD types because the cytoskeleton is directly related to migratory cell behavior. We prepared both soft SMPAD with 2  $\mu\text{m}$  and stiff SMPAD with 7  $\mu\text{m}$  bottom pillar diameters. We cultured C2C12 cells ( $1 \times 10^4$  cells/mL) on both prepared surfaces. To visualize the pillar tops, we treated the SMPAD surface with DiI solution, which was absorbed by and stained the SMPAD surface before cell seeding. DAPI and a vinculin antibody labeled with FITC were used to stain the cells 24 h after cell seeding to examine differences in cell morphology. Fluorescence images were captured by confocal microscopy (Carl Zeiss, Germany). Figure 2-6 illustrates that the cells on the soft substrate have fewer stress fibers than the cells on the stiff substrate. Stress fibers in the stiff platform were articulated and more prominent. These results indicate that the formation of the cytoskeleton is modulated by SMPAD stiffness.

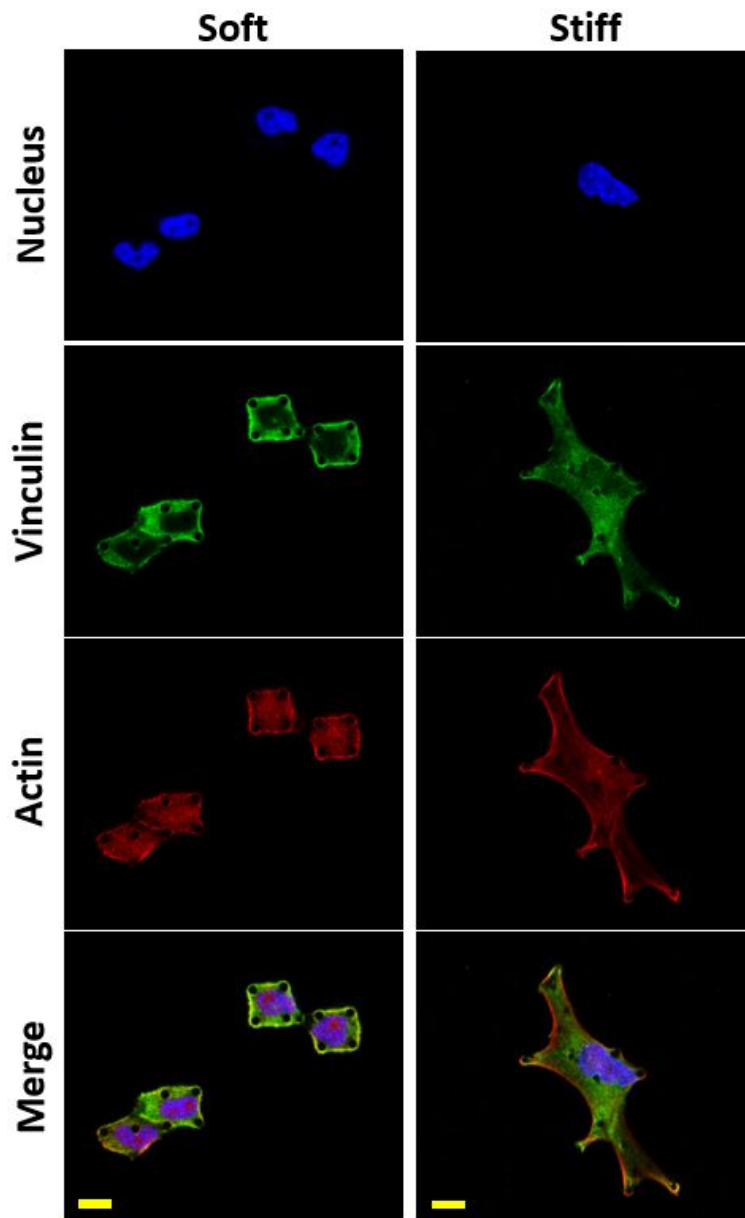
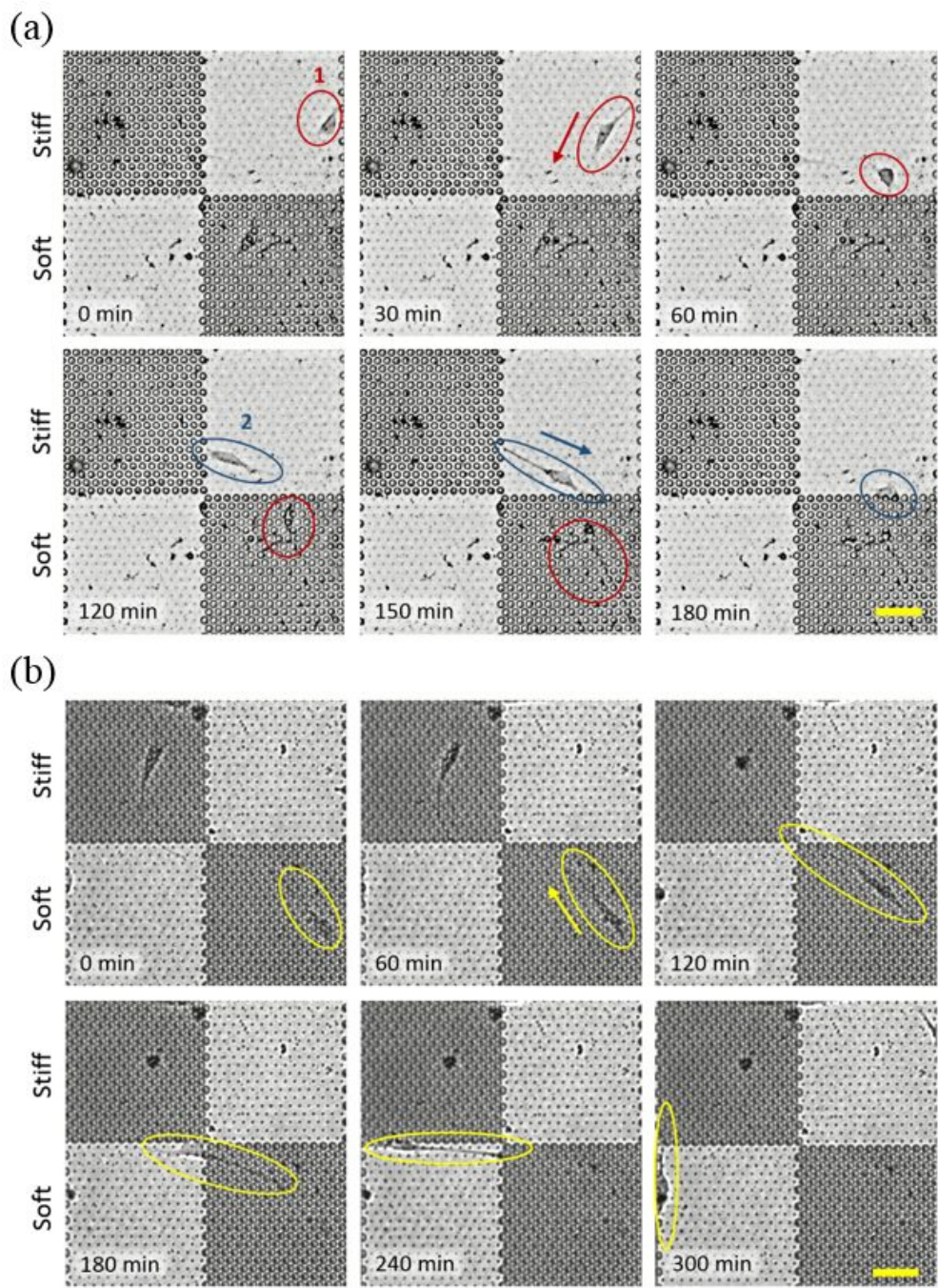


**Figure 2-6** Cell morphology obtained by confocal microscopy. The nucleus, vinculin and actin filament of cultured cells on the soft (left column) and stiff (right column) types of SMPAD were visualized using DAPI, vinculin and actin antibodies respectively. Scale bar, 10  $\mu$ m.

#### **2.3.4 Cell motion on the soft-to-stiff pillar array**

We cultured and investigated the muscle cell line C2C12 on the soft and stiff type of SMPAD because this cell line has been used as a model of skeletal muscle cell adhesion [93,94], growth and differentiation and is affected by the mechanical properties of the environment. We selected a hexagonal arrangement for the pillar array, rather than the square arrangement used for the cell migration experiments, to minimize the attached cell area. The size of the pillar pattern in the soft (2.3 nN/ $\mu\text{m}$ ) and stiff (204.3 nN/ $\mu\text{m}$ ) pillar array was  $150 \times 150 \mu\text{m}$  considering the area of spreading cells. Figure 2-7(a) shows that the C2C12 cells were primarily attached to the soft pillar array. After cell attachment, these cells began to spread and sense the surrounding environment in the soft substrate. When the cells probed the stiff pillar array with a tapping motion, they suddenly leaped from the soft pillar array and quickly moved across to the stiff region (cell 1). Although the cells were attached to the stiff pillar array, they could move onto the soft pillar array to investigate the environment with a tapping motion (cell 2). In this case, the cells also showed successive migration toward the stiff pillar array.

Then, we observed the behavior of cells attached to the stiff pillar array (Figure 2-7(b)). After the cells continued to tap the surrounding stiff environment, they migrated toward a separate stiff pillar array site by moving along the stiffness boundary (yellow circle). These results demonstrate that C2C12 migration is regulated by the substrate stiffness and that these cells migrated toward the stiff substrate. To determine the effect of substrate stiffness on cell behavior in another cell line, we also tested a typical cancer cell line, HeLa, on this platform. Figure 2-7(c) and (d) illustrates that C2C12 cells significantly migrated toward the stiff pillar array after 21 h, whereas the HeLa cells moved and migrated randomly. Five different replicates were performed, and more than 100 cells from each cell line were analyzed to generate these results.



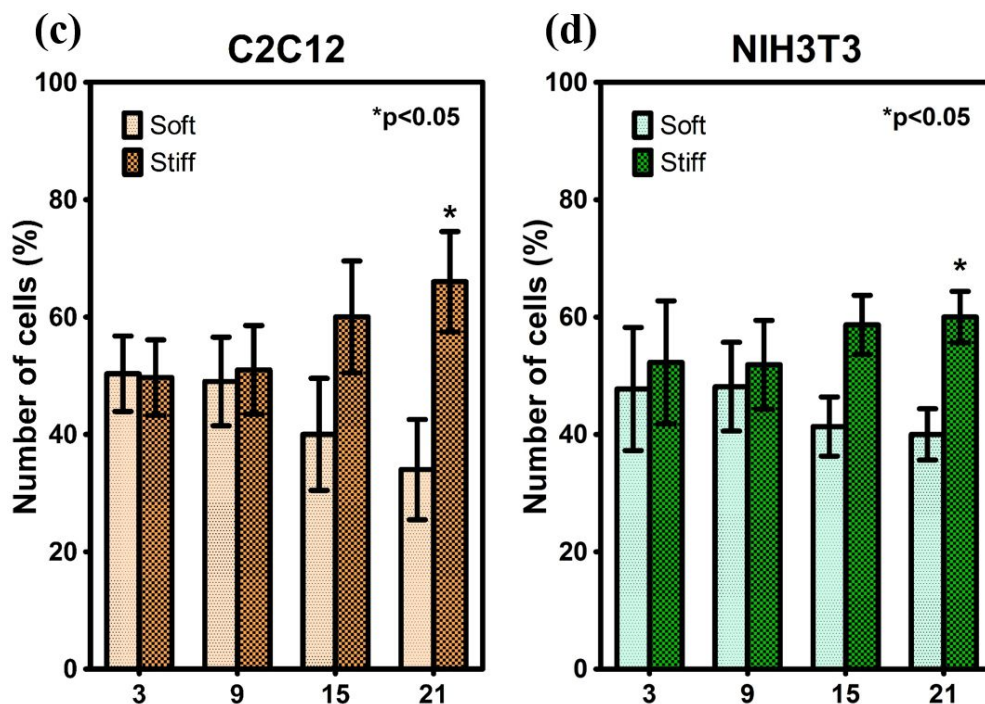


**Figure 2-7** Cell responses and migratory behavior on SMPAD with the binary stiffness pillar array (a). When a cell was attached to the soft portion of the substrate, it investigated the surrounding environment with a tapping motion and slowly moved toward the stiff portion of the substrate (cell 1). Although the cell began to move from the stiff portion of the substrate and touched the soft portion, it quickly displaced toward other stiff portions of the substrate (cell 2). The cell explored and migrated along the stiffness boundary and remained on the other stiff area when the cell had initially attached to a stiff portion of the substrate (b). Scale bar, 50  $\mu\text{m}$ . To monitor the real-time cell migration in different cell types, we cultured C2C12 and HeLa cells on our devices. We counted the number of cells on the soft and stiff portions of the substrate every 3 h for up to 21 h. For C2C12, a tendency to move toward the stiff area was observed on C2C12 (c) and NIH3T3 (d).

### 2.3.5 Cell motility analysis

To evaluate the effect of the stiffness gradient on cellular behavior, we cultured NIH3T3, a widely used mouse fibroblast cell line, for the migration experiments [95-98] on three types of substrates: flat PDMS (Control), a uniformly distributed pillar array substrate (Uniform), and a SMPAD with gradually increasing bottom pillar diameters (Gradient). To minimize cell-to-cell communication, a small number of cells ( $1 \times 10^3$  cells/mL) were sparsely plated on the SMPAD placed in a culture dish. Then, we focused on the migration of an individual cell on the array. Cells attached and spread independent of each substrate within hours of seeding, with most cells tapping and beginning to migrate to the surrounding environment, similar to previous experiments [99,100]. As shown in Figure 2-8(a), NIH3T3 cells migrated in response to the stiffness gradients present in the gradient substrate but remained near their original position on flat and uniform substrates within 3 h. To more quantitatively verify that cell migration behavior is affected by environmental stiffness gradients, the net distance traveled by cells on the three types of substrate was measured using time-lapse video microscopy over 5 h (Figure 2-8(b)). Using ImageJ software, we tracked the path of more than 30 cells on each platform and measured the distance traveled every 30 min. A significant increase in the net distance was observed after 150 min for the migratory cells attached to the gradient substrate, whereas no significant migratory behavior was observed on the flat and uniform substrates. These results demonstrate that the stiffness gradient of the substrate on which cells are attached triggers cell migration and ultimately affects cellular behavior.

To monitor the effects of the degree of stiffness on cellular behavior, we cultured the NIH3T3 on three types of stiffness gradients, a low gradient strength ( $\Delta K = 0.5$  nN/ $\mu\text{m}$ ), medium gradient strength ( $\Delta K = 5$  nN/ $\mu\text{m}$ ) and high gradient strength ( $\Delta K = 50$  nN/ $\mu\text{m}$ ). The low gradient strength substrate included pillar

diameters ranging from 2 to 3  $\mu\text{m}$ , which corresponded to a physiologically relevant stiffness of 6.8 to 72  $\text{nN}/\mu\text{m}$  (Figure 2-9(a)). The medium gradient strength substrate was designed with pillar diameters ranging from 2 to 5  $\mu\text{m}$ , which corresponded to a pillar stiffness of approximately 6.8 to 149  $\text{nN}/\mu\text{m}$  (Figure 2-9(b)). The high gradient strength substrate included pillar diameters ranging from 2 to 7  $\mu\text{m}$ , which corresponded to a pathologically relevant stiffness of 6.8 to 267  $\text{nN}/\mu\text{m}$  (Figure 2-9(c)). When the rigidity gradient was 0.5  $\text{nN}/\mu\text{m}$ , the cells wandered nearly randomly without a specific orientation. The cells began to directionally migrate toward higher stiffness regions when the gradient was 5  $\text{nN}/\mu\text{m}$ . This stiffness-guided migration was highly repeatable and consistent on the pillar array with the 50  $\text{nN}/\mu\text{m}$  stiffness gradient. The final locations of cells in Figure 2-9(a), (b), and (c) illustrate these behaviors, as shown by enhanced green fluorescence protein (eGFP) expression in NIH3T3 cells 18 h after experiment onset. Figure 2-9(d), (e), and (f) more clearly demonstrates that the successive migratory behavior of cells depends on the stiffness gradient over 12 h. A large displacement was observed in the x axis with the high rigidity gradient (Figure 2-9(f)), whereas no significant difference was observed between the distances along the x and y axes with the low rigidity gradient (Figure 2-9(d)). After 8 h, the cell migration distance was greatly increased on the high stiffness gradient pillar array (Figure 2-9(f)). This motility enhancement became more pronounced on the larger stiffness gradient, as illustrated in Figure 2-9(g). The cell velocity along the x axis on the high-strength SMPAD was  $1.3 \pm 0.32$   $\mu\text{m}/\text{min}$  and  $0.38 \pm 0.12$   $\mu\text{m}/\text{min}$ , with no stiffness variation. The mean velocity of each cell in the x-direction was traced over 24 h ( $n \sim 20$ ), and the error bars represent the  $V_{\text{max}}$  and  $V_{\text{min}}$  on each platform. These data clearly indicate that the strength of the stiffness gradient greatly affects cell motility. These results demonstrate that cell movement is highly influenced by the environmental stiffness gradient and its strength, similar to the findings of previous research [100].

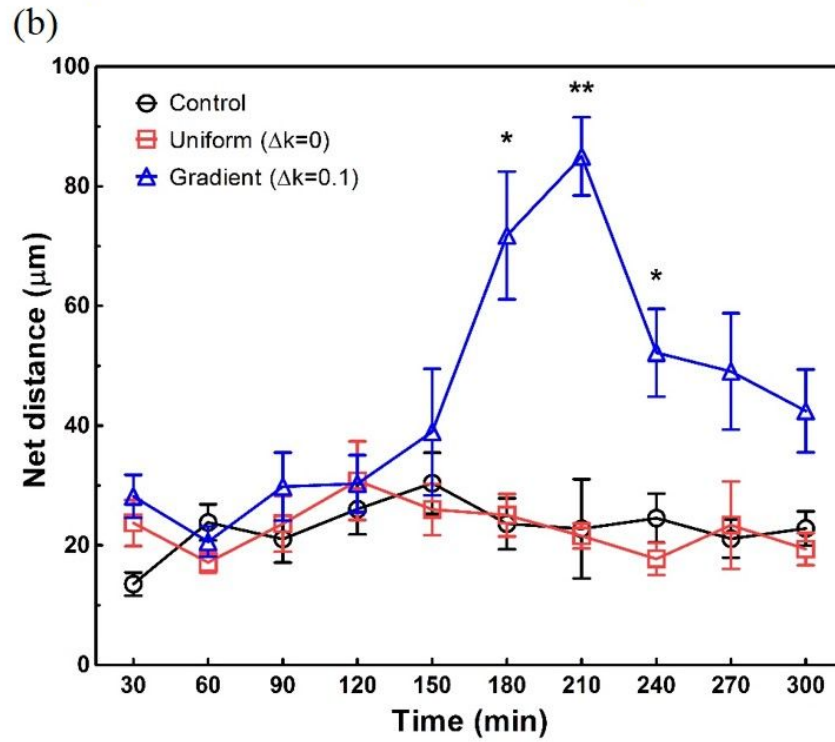
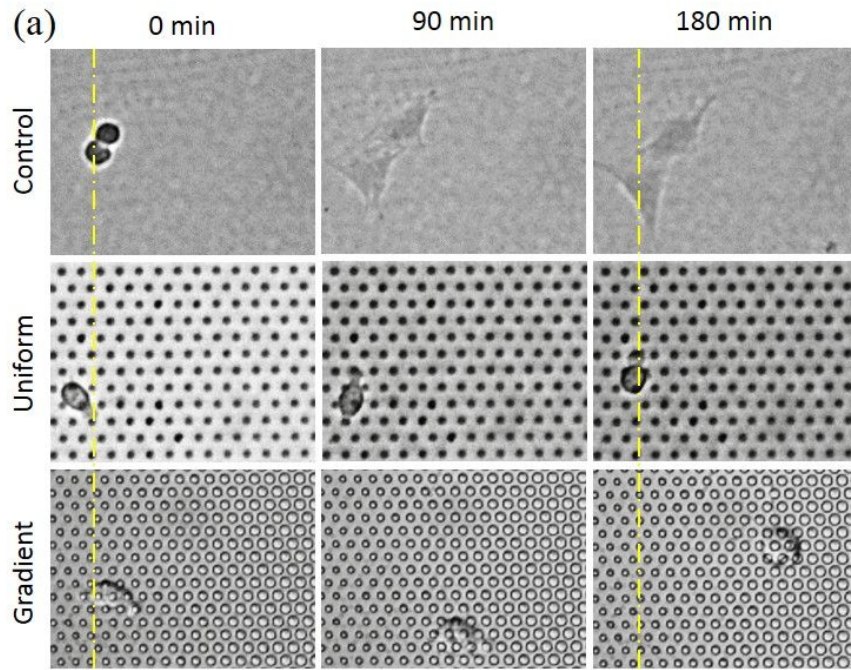


**Figure 2-8** NIH3T3 behavior on flat PDMS (Control), SMPAD with identical stiffness (Uniform), and SMPAD with gradually increasing stiffness in the x-direction (Gradient) (a). Cell showed directional migration in the direction of increasing stiffness over 180 min. The net distance traveled by migrated cells in 30 min increments up to 300 min was used to compare the motion of cells on three types of substrate (b). No specific tendency for migration direction was observed between groups at up to 150 min. However, a particular increase in travel distance was observed from 150 min to 210 min, and the cells that attached to the gradient substrate travelled much further than the cells attached to other types of substrates. \* $p < 0.05$  and \*\* $p < 0.005$ .

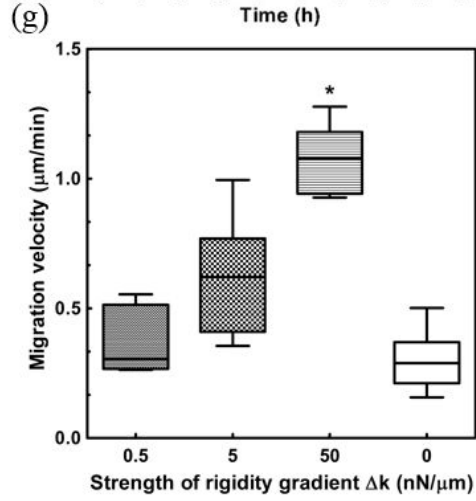
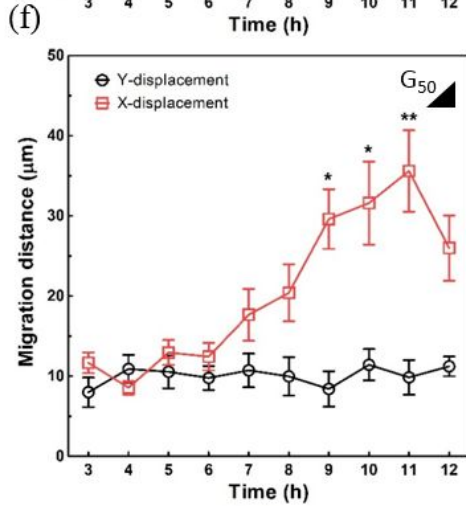
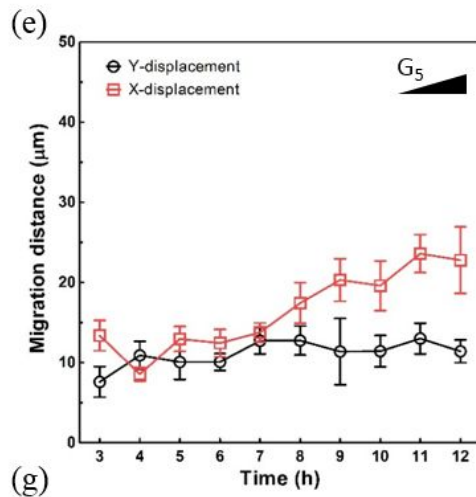
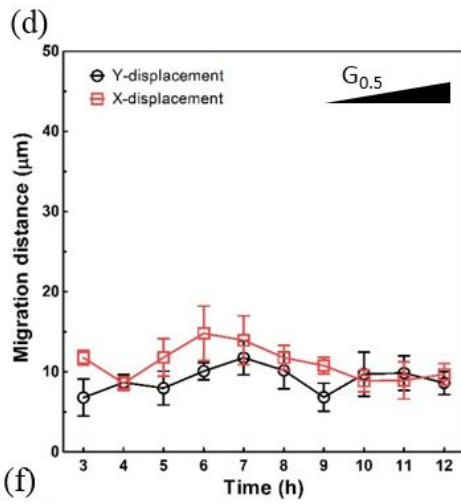
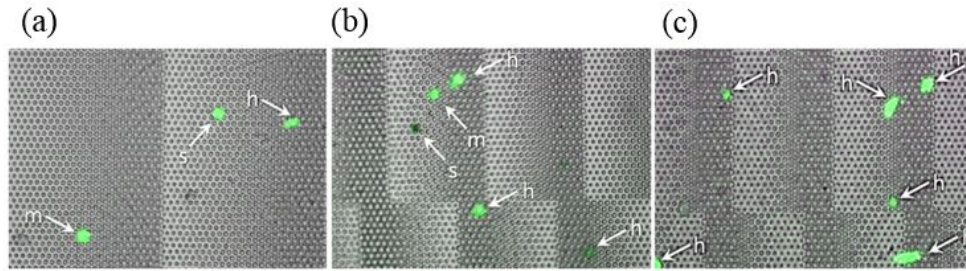


**Figure 2-9** The location of NIH3T3 cells 18 h after attachment to the SMPAD with low gradient strength ( $G_{0.5}$ ) (a), medium gradient strength ( $G_5$ ) (b), and high gradient strength ( $G_{50}$ ) (c) stiffness. Cells randomly distributed initially, ended up with the vicinity of indicated locations after 18 hours of migration. White arrows indicate the stiffness of the final locations. (h: hard, m: medium, s: soft area). No difference in migration distances was observed between the x-direction and y-direction when the cells migrated on the low-strength SMPAD (d). The  $G_{0.5}$  type of SMPAD, which is the middle gradient strength, began to induce a mild increase in x-directional migration (e). The distance of cell migration increased sharply on the high-strength SMPAD along the x-direction (f). Cells on the high-strength SMPAD migrated along the x-direction with the highest velocity (g). More than 100 cells on each substrate were used to generate this result. \* $p < 0.05$  and \*\* $p < 0.005$ .

## **2.4 Summary**

Cell migration was demonstrated along a discrete rigidity gradient created by pillars with varying diameters. By maintaining a uniform area on top of the pillars, we eliminated any effect of the size of the adhesion area. The two-step fabrication technique of the double-layered pillar enabled this special configuration. Using this simple platform, which produces a purely physical stimulus, we observed that various types of cell behavior were affected by the mechanical stimulus from the environment. We also demonstrated a directed cell migration guided by a discrete rigidity gradient of varied strength. Interestingly, cell velocity was highest at the highest stiffness gradient strength, similar to the simulated results from previous studies. Our approach allowed us to regulate the mechanical properties of the polymeric pillar array device and eliminated the effects of the size of the contact area. This technique is a unique tool for studying cellular motion and behavior in relation to various stiffness gradients of the environment. The newly developed platform introduced here can be further used to investigate cell migration for many other biological applications, such as artificial tissue engineering, plastic surgery, and the study of the migration behavior of cancerous cells.

## **Chapter 3 Nanomaterials in Biology Application**

### **Bacterial Magnetic Nanoparticle Conjugated with VDAC2 antibody and Carbon Nanotube**

In this chapter, we first show that magnetic capture of mitochondrial VDAC2 with BMPs conjugated VDAC2 antibody was significantly decreasing the expressed intracellular calcium levels and neurotoxicity induced by A $\beta$ . This magnetic modulation of mitochondrial VDAC play key role in various Ca<sup>2+</sup> flux pathways should provide attractive targets for future development of Alzheimer's disease.

And then, we present a self-degradation route for SWNTs mediated by the built-in peroxidase-like activity of BMPs. BMPs can act as effective built-in intrinsic peroxidases that are comparable to other enzymatic methods for the degradation of SWNTs. For possible applications in neurobiology, f-SWNT-BMP hybrids were shown to be inhibitors that reduce the formation of amyloid-beta fibrils, which are considered the key element behind Alzheimer's disease.

### **3.1 Bacterial Magnetic Nanoparticle conjugated VDAC2 Antibody**

Mitochondria are the governors of both cell life (e.g. energy generation) and cell death. Some regulation of both of these functions occurs at the level of the outer membrane in that it controls the flow of metabolites and the release of intermembrane space proteins into the cytosol. The VDAC proteins, pore-forming proteins predominantly found in the outer mitochondrial membrane, are the major pathways for anions, cations, ATP,  $\text{Ca}^{2+}$  and metabolites flux through the outer membrane [101,102]. These can be regulated in many ways and the integration of these regulatory inputs allows mitochondrial metabolism to be adjusted to changing cellular conditions [103,104].  $\text{Ca}^{2+}$  is known to synchronize mitochondrial metabolism as well as intracellular  $\text{Ca}^{2+}$  signalling is fundamental to neuronal physiology and viability. Therefore  $\text{Ca}^{2+}$  signalling have become a major focus of study in multifactorial neurodegenerative diseases such as Alzheimer disease (AD) [105,106]. In AD, neurotoxic mechanisms that are associated with  $\beta$ -amyloid ( $\text{A}\beta$ ) include mitochondria dysfunctions cause disturbances in calcium homeostasis [107]. This suggests that the control of intracellular calcium flux can prevent or inhibit fatal injury caused by  $\text{A}\beta$ -induced neurotoxicity. Here, we demonstrate that the magnetic modulation of mitochondrial VDAC2, which is the only mammalian-specific isoform among VDAC isoforms, can contribute to protect the neurodegenerative disease attenuating the changes in the intracellular calcium levels that were induced by beta-amyloid. In this study, BMPs originated from *Magnetospirillum* sp. AMB-1 directly conjugated with VDAC2 antibody using 1-Ethyl-3-(3-dimethylamino propyl) carbodiimide (EDC) linker which is used to couple carboxyl groups to primary amines (Figure 3-1).

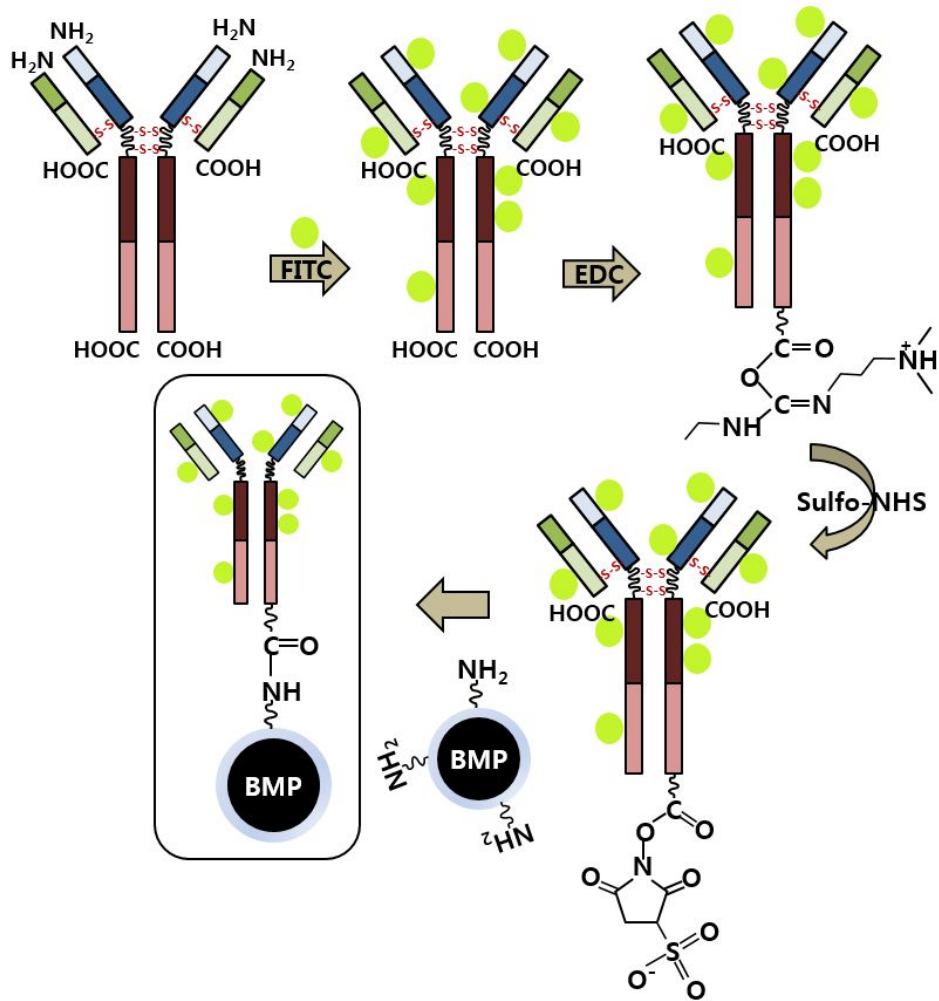


**Figure 3-1** Schematic of the BMP-VDAC2 Ab complex

### **3.1.1 Materials and Methods**

#### **3.1.1.1 Preparation of BMPs**

BMPs were obtained from *Magnetospirillum* sp. AMB-1 (ATCC<sup>®</sup> 700264), which was cultured in magnetic spirillum growth medium (MSGM) for 5 days inside shaking incubator at 30 °C under anaerobic conditions. Cultured *Magnetospirillum* sp. AMB-1 were centrifuged for 25 min at 5000 rpm and then lysed by sonication (VCX500, Sonics&Materials, USA) for 30 min. BMPs were collected using a neodymiumiron boron (NdFeB) magnet and washed for 5 times with 1X PBS. Collected BMPs were dispersed in 1X PBS and sterilized with autoclave (121 °C, 15 min). Concentration of extracted BMPs was determined by inductive coupled plasma-atomic emission spectrometer (ICP-AEX, ICPS-7500, Shimadzu, Japan).

#### **3.1.1.2 Conjugation of VDAC2 antibody to BMPs**

N-(3-Dimethylaminopropyl)-N'-ethylcarbodiimide hydrochloride(EDC, Sigma-aldrich, Korea) and N-Hydroxysulfosuccinimide sodium salt (Sulfo-NHS, Sigma-aldrich, Korea) were dissolved in 0.1 M MES buffer (2-(N-morpholino) ethanesulfonic acid, pH=8.3). The mixture was added to 10 µl of 1 mg/ml C-termini VDAC2 antibody to be able to react with a carboxyl group for 15 min to form an amine-reactive O-acylisourea intermediate. After adjustment of pH in between 7 to 8 by adding 3 µl of 20X PBS buffer, 500 µl of BMPs contained in 1X PBS is added. This mixture is gently shaken at room temperature for 2 h to accelerate binding reaction. Unconjugated antibodies were separated from the antibody conjugated BMPs three times with 1X PBS buffer under the strong magnet field. Bicinchoninic acid (BCA) protein assay was demonstrated to determine the amount of antibody bound to nanoparticle. BCA protein assay result showed that the amount of antibody bound to BMP is around 60 %.

### **3.1.1.3 Amyloid beta 25-35 aging**

A $\beta_{25-35}$  was dissolved in distilled water at a concentration of 1 mM and then incubated in a capped vial at 37 °C for 7 days to form aggregation, which was frozen and stored at 4 °C.

### **3.1.1.4 Cell culture and BMPs loaded cell preparation**

Human neuroblastoma SH-SY5Y cells were cultured in Low glucose Dulbecco's modified Eagle's medium (DMEM/LOW GLUCOSE, Thermo Scientific, USA) at 37 °C with 5 % of CO<sub>2</sub> to reach a confluence of 70 % to 80 % containing 10 % (v/v) fetal bovine serum (FBS, Thermo Scientific, USA) and 1 % penicillin/streptomycin (Thermo Scientific, USA). The BMPs and VDAC2 antibody conjugated BMPs were treated in the serum free medium with 10 µg/ml concentration during 6 h for sufficient time to internalize. And then they were cultured in normal cell culture medium for 24 h to take enough time to deliver particles into the intracellular organelles. After trypsinization, magnetic particle loaded cells were separated from non-loaded cells and collected using strong neodymium magnet. Collected magnetic particle loaded cells were seeded at  $1 \times 10^4$  cells/well in 96-well plate after cell enumeration using a hemocytometer.

### **3.1.1.5 Intracellular calcium level measurement**

To induce cell injury, cells were incubated with 50 µM A $\beta_{25-35}$  for 24 h. To study the effects of BMP-VDAC2 antibody complex, cells were pre-incubated with particles for 3 days, and then A $\beta_{25-35}$  was added to the medium of magnetically collected cells for additional 24 h. To measure the intracellular calcium level of BMP-VDAC2 antibody loaded and normal SH-SY5Y cells, cells grown on glass coverslip were treated for 30 min at 37 °C with 5 µM Fluo-3 AM. The fluorescence changes determined by Fluo-3 represent the intracellular calcium [Ca<sup>2+</sup>]<sub>i</sub> changes. Multiple Plate Reader (Victor 3, Perkin Elmer, USA) were acquired fluorescence level using a

488-nm laser source to excite Fluo-3. The signals were collected at 505-530 nm.

### **3.1.1.6 Fluorescence labelling**

In order to check accurate targeting of BMPs-VDAC2 antibody complex onto intercellular organelle, VDAC2 antibody was labeled with the fluorescein isothiocyanate (FluoroTag<sup>TM</sup>, Sigmaaldrich, Korea) which is a widely used fluorophore prior to the immobilization of antibody and BMPs. After delivering of FITC labeled BMPs-antibody complex into the SH-SY5Y cells for 24 h, cells were fixed with 3.7 % formaldehyde in 1X PBS for 15 min at room temperature. Following washing twice with wash buffer, 0.1 % Triton X-100 in 1X PBS, the fixed cells were permeabilized and blocked with 1 % BSA and 0.1 Triton X-100 in 1X PBS for 20 min. Then the actin filaments were stained by incubating cells with TRITC-conjugated phalloidin (1:200) for 50 min at room temperature. The cells were washed three times with 1X PBS and nucleus staining was performed by incubating three times with a diluted DAPI in 1X PBS (1:1000) for 5 min each. The stained cells were examined using a confocal laser scanning microscope (Carl Zeiss-LSM510, Germany).

### **3.1.1.7 Cell viability assay**

#### **3.1.1.7.1 ATP assay MTS assay**

3-(4,5-dimethylthiazol-2-yl)-5-(3-carboxymethoxyphenyl)-2-(4-sulfophenyl)-2H-tetrazolium (MTS) was used to evaluate the cytotoxicity of the particles and viability of cells in several conditions.  $1 \times 10^4$  cells/well of SH-SY5Y cells were seeded on 96-well plate with 100  $\mu$ l of the culture medium. After incubation for 6 days on each condition, 20  $\mu$ l of CellTiter 96<sup>®</sup> Aqueous One Solution Reagent (Promega, USA) was added into each well. Then the plate was incubated at 37 °C for 2 h in a humidified 5 % CO<sub>2</sub> atmosphere and absorbance was recorded at 490 nm with an absorbance reader (Thermo Fisher Scientific Inc., USA). All of the assays were

repeated at least twice and 3 wells for one group were investigated in each assay. The absorbance of control cells was normalized to 100 % of viability in every assay.

#### **3.1.1.7.2 ATP assay**

The SH-SY5Y cells ( $1 \times 10^4$  cells/well) were seeded on opaque-walled 96-well plate with 100  $\mu$ l of the culture medium and cultured for 3 and 6 days. ATP content was measured in accordance with the protocol of CellTiter-Glo Luminescent cell viability assay kit (Promega, USA). The procedure was followed a protocol provided by manufacturer. In brief, 100  $\mu$ l of CellTiter-Glo reagent was added to the each well and mixed for 2 min at room temperature. Then the intracellular ATP content was measured using luminometer (Thermo Fisher Scientific Inc., USA). The assay was repeated twice and 3 wells for one group were investigated in each experiment.

### 3.1.2 Results

#### 3.1.2.1 BMPs preparation and VDAC2 targeting

The BMPs from the *Magnetospirillum sp.* AMB-1 used in our approach are inherently biocompatible, can be effectively conjugated with other biomolecules, and disperse well in aqueous solutions because of their stable lipid membrane surrounding the magnetic core (Figure 3-2). The lipid membrane is rich in phosphatidyl-ethanolamine (approximately 29 %), which provides amine-binding sites, making the BMPs easy to disperse and conjugate to other biomolecules, such as antibodies, enzymes, and polypeptides. Therefore, we could make our hybrids via a very simple method. BMPs directly conjugated with VDAC2 antibody using 1-Ethyl-3-(3-dimethylamino propyl) carbodiimide (EDC) linker which is used to couple carboxyl groups to primary amines. BMPs-VDAC2 antibody complexes (BMPs-Ab) introduced into SH-SY5Y cells, human derived neuroblasts which are often used as *in vitro* models of neuronal function and differentiation. As shown in Figure 3-3 and 3-4, most of BMPs-Ab were successfully internalized into SH-ST5Y cells and observed with correlation to mitochondria (yellow color). In contrast, BMPs without VDAC-2 antibody were randomly distributed inside cells, with no particular mitochondrial localization.

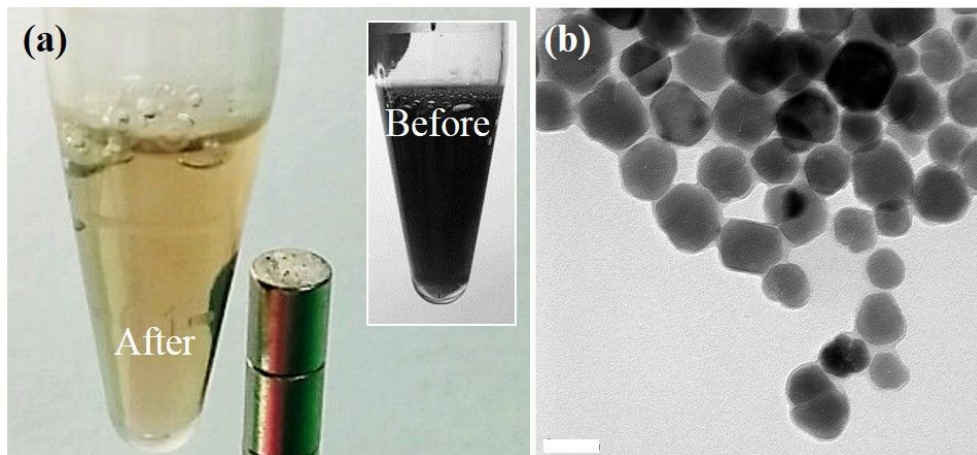


**Figure 3-2** (a) Magnetic attraction of BMP disperse in 1X PBS, (b) Transmission electron microscopy (TEM) image of BMP with a scale bar 50 nm. The BMPs from the *Magnetospirillum* sp. AMB-1 were used in our approach, which are inherently biocompatible, can be effectively conjugated with other biomolecules, and can be dispersed well in aqueous solutions because of their stable lipid membrane surrounding the magnetic core.

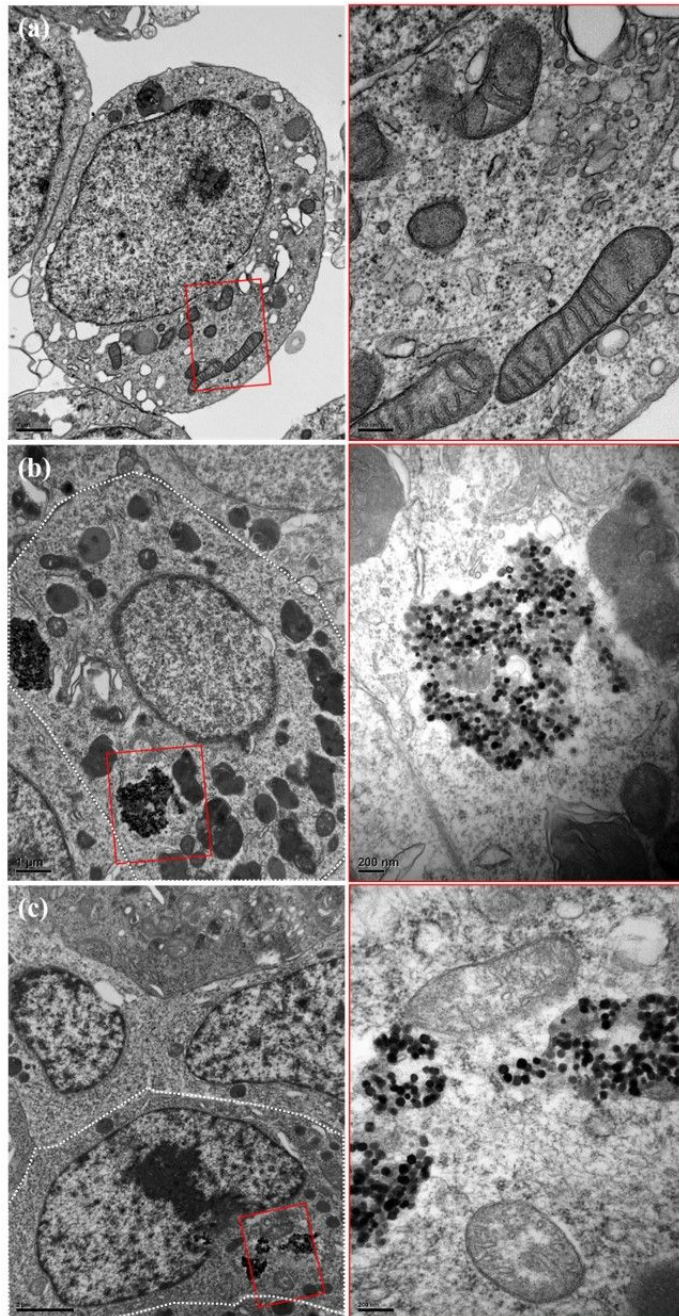


**Figure 3-3** Transmission electron microscopy (TEM) image of BMPs internalized by a SH-SY5y cells. (a) Control, (b) BMPs only, and (c) BMPs-antibody conjugate.

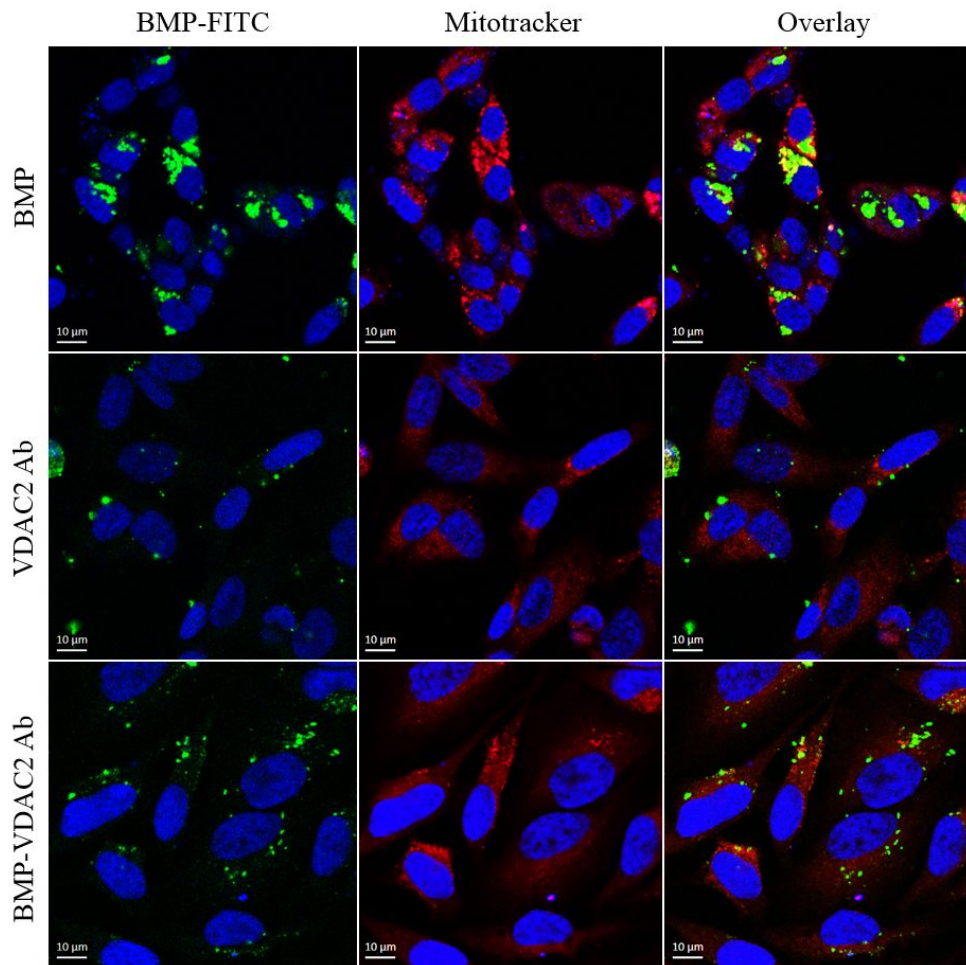


**Figure 3-4** Specific targeting of BMP-VDAC2 Ab complex to mitochondria inside SH-SY5Y cells; blue: nucleus, red: mitochondria, green: BMP; scale bar: 10  $\mu$ m.

### 3.1.2.2 Calcium level

We investigated that the effect of magnetically modulated VDAC2 on the change of intracellular  $\text{Ca}^{2+}$  levels induced by  $\text{A}\beta$ . SH-SY5Y cells were loaded with 5  $\mu\text{M}$  Fluo-3 AM (Sigma-Aldrich Co., USA) for 30 min, and then the changes in the level of  $\text{Ca}^{2+}$  before and after treatment with  $\text{A}\beta$  were measured by 488-nm laser source to excite Fluo-3. We prepared number of optical images to show intracellular calcium level of untargeted and targeted SH-SY5Y cell in presence or absence of  $\text{A}\beta$  in supplementary information (Figure 3-5). Because of their many roles in energy production, cell-death regulation, and cell signalling transduction, mitochondria have been considered an important target for therapeutic treatment of various diseases [108,109]. Thereby, the efficient internalization and specific mitochondrial VDAC2 targeting of the BMP-Ab is promising for mitochondria specific manipulation of cell function.  $\text{A}\beta$ , a hallmark of AD, destabilizes intracellular  $\text{Ca}^{2+}$  homeostasis, resulting in an elevation of intracellular free  $\text{Ca}^{2+}$  concentration [106,110,111]. Fluorescence intensity reflecting intracellular  $\text{Ca}^{2+}$  concentration was measured by the Microplate Reader (Victor 3, Perkin Elmer, USA). As shown in Figure 3-6, intracellular calcium levels of VDAC2 targeted SH-SY5Y cells with BMPs-Ab moderately decreased compare to those of untargeted cells when the  $\text{A}\beta$  was not treated. After treatment of  $\text{A}\beta$ , however, capture of VDAC2 with BMPs-Ab was found to more significantly decrease the expressed intracellular calcium levels when compare to those of untargeted cells (Figure 3-7).  $\text{Ca}^{2+}$  is an interesting second messenger which can initiate both cellular life and death pathways in mitochondria.

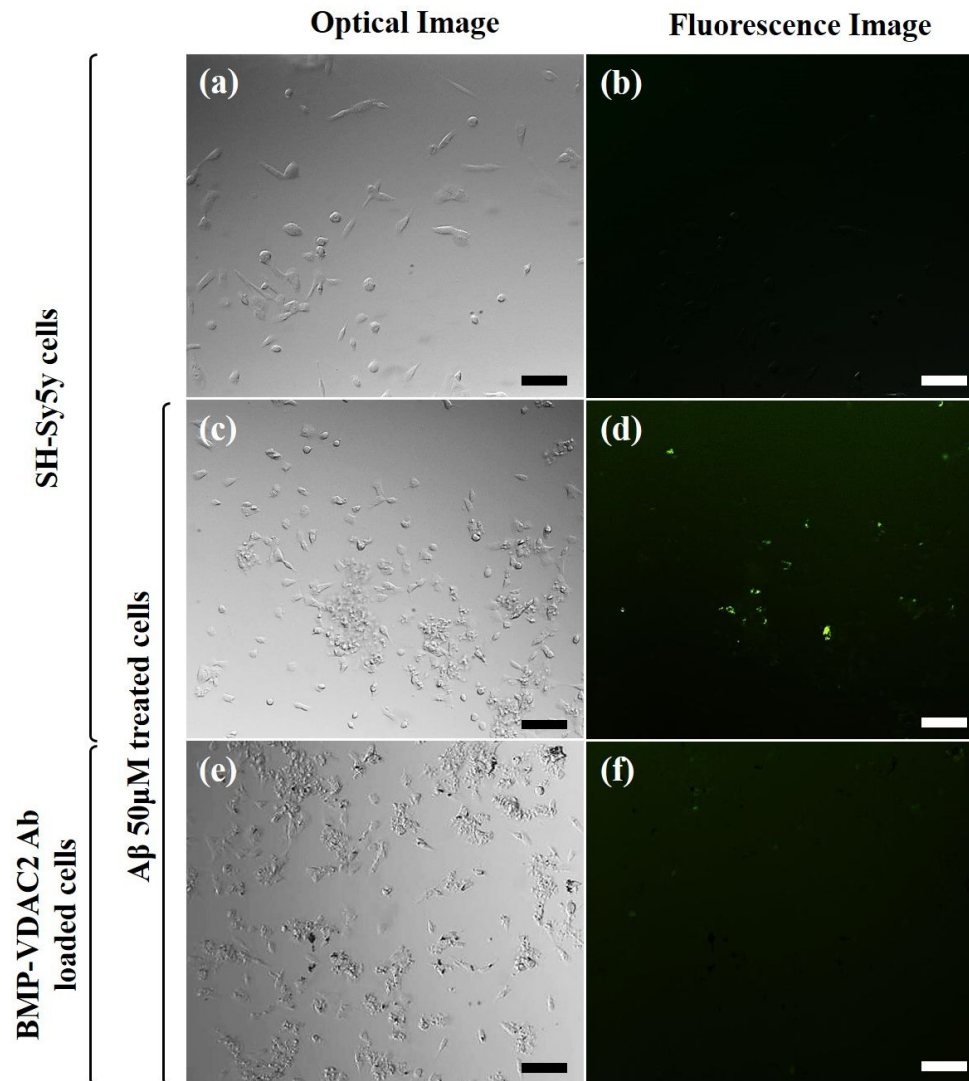


**Figure 3-5** (a) Optical, (b) fluorescence images of normal SH-Sy5y cells; (c) optical and (d) fluorescence images of  $\beta$ -amyloid treated normal SH-Sy5y cells; and (e) optical and (f) fluorescence images  $\beta$ -amyloid treated BMP-Ab loaded SH-Sy5y cells. It is clear that  $\text{Ca}^{2+}$  level of  $\beta$ -amyloid treated normal cells is much higher than level of BMP-Ab loaded cells.

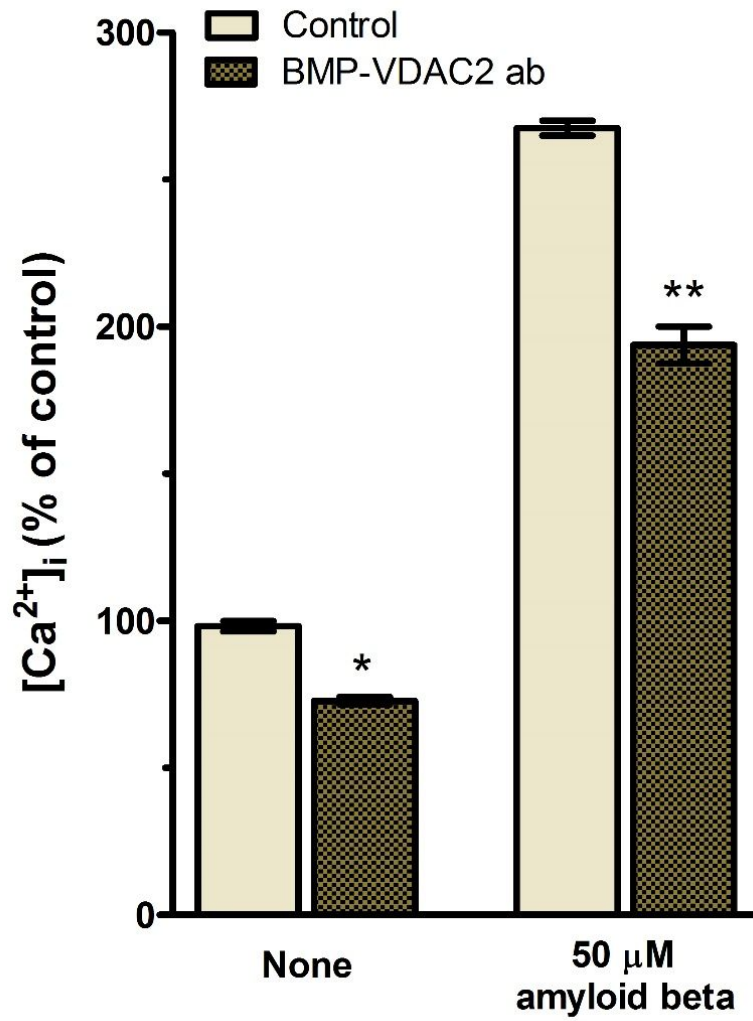


**Figure 3-6** Effect of BMP-VDAC2 ab complex to reduce calcium influx induced by amyloid beta. Calcium level was calculated from the calibrated fluorescence signal of the probe fluo-3. \* $p < 0.05$  and \*\* $p < 0.01$  compared with the control cell.

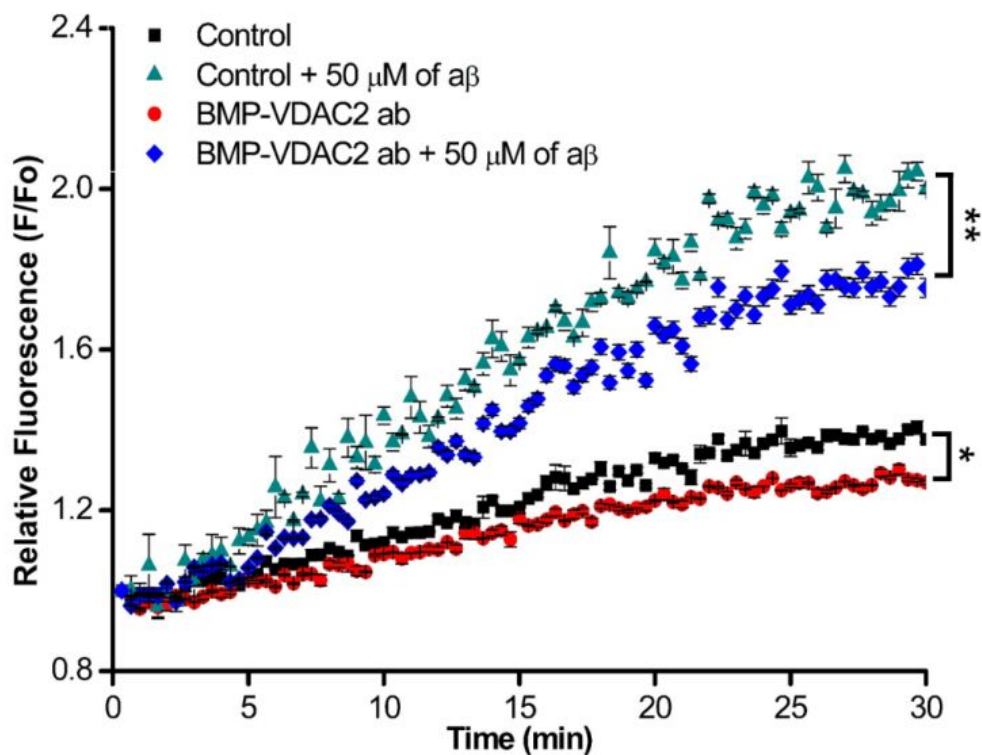


**Figure 3-7** Effect of BMP-VDAC2 Ab complex on amyloid beta-induced  $\text{Ca}^{2+}$  influx in the SH-SY5Y cells. Control: VDAC2 untargeted, BMP-VDAC2 ab: VDAC2 targeted cells, Control + 50  $\mu\text{M}$  of  $\text{A}\beta$ : VDAC2 untargeted cells under  $\text{A}\beta$  treated condition, BMP-VDAC2 ab + 50  $\mu\text{M}$  of  $\text{A}\beta$ : VDAC2 targeted cells with BMPs-Ab under  $\text{A}\beta$  treated condition. (\* $p < 0.05$  and \*\* $p < 0.01$ ,  $n=3$ )

### **3.1.2.3 BMP-VDAC2 ab loaded cell viability**

Mitochondria accumulate  $\text{Ca}^{2+}$  for cellular bioenergetics metabolism and suppression of mitochondrial motility within the cell. Excessive  $\text{Ca}^{2+}$  uptake into mitochondria often leads to mitochondrial membrane permeabilization and induction of apoptosis. Interestingly, magnetic modulation of VDAC2 considerably increases the proliferation of SH-ST5Y cells, up to 50% for 3 days culture (Figure 3-8(a)). The increased growth can be ascribed to the ATP content of the VDAC2 targeted cells that improved about 30% higher compared with that of VDAC2 untargeted cells (Figure 3-8(b)).

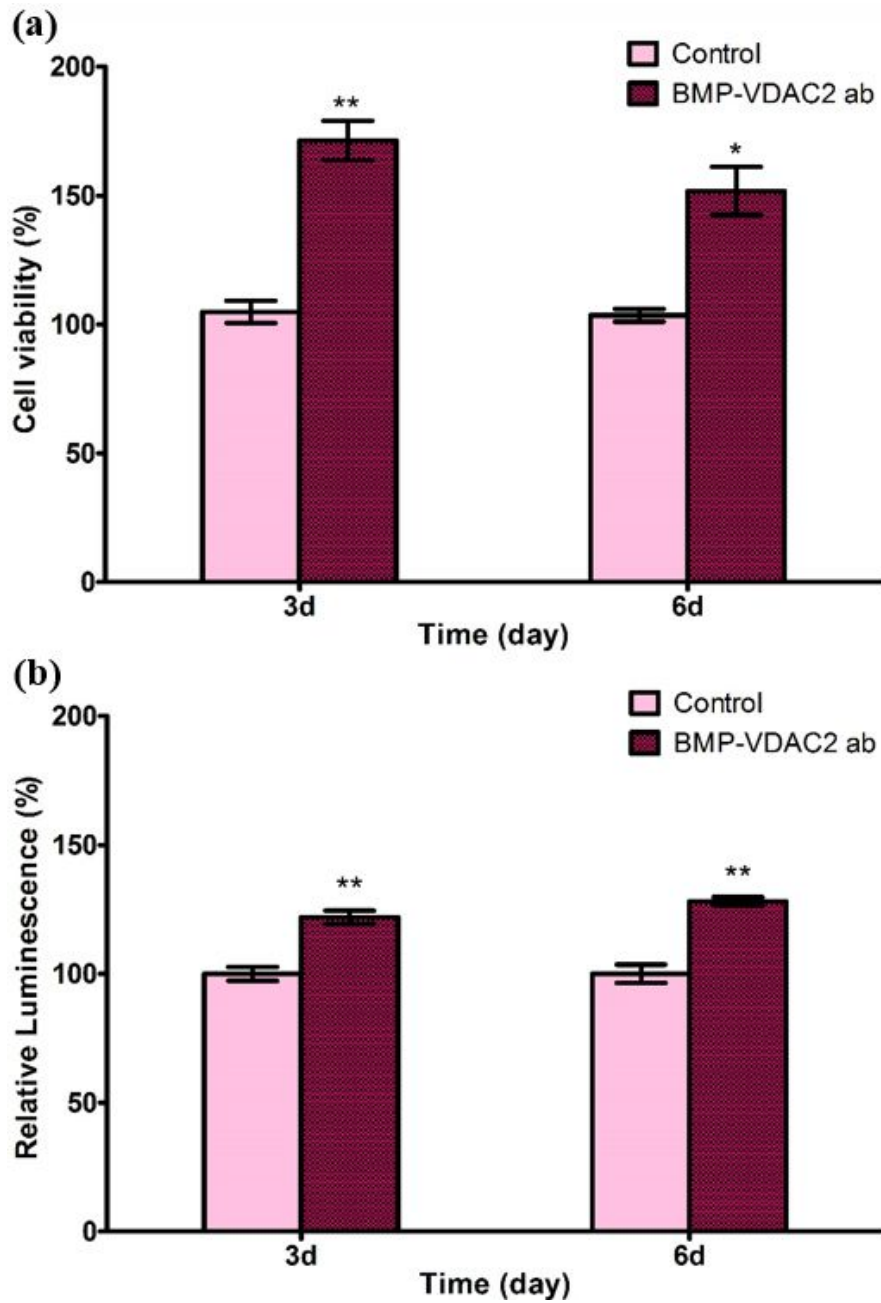


**Figure 3-8** Effect of BMP-VDAC2 Ab complex on cell growth by (a) MTS assay and (b) ATP level. Under the amyloid-beta induced neurotoxic condition

#### 3.1.2.4 Effects on amyloid beta induced injury

Previous results were reconfirmed with the change of cell viability in the presence of A $\beta$  (25–35), which destabilize intracellular Ca<sup>2+</sup> homeostasis. As shown in Figure 3-9(a) and (b), A $\beta$  treatment induced lethal cell death, however, magnetic capture of VDAC2 with BMPs-Ab significantly reduced A $\beta$ -induced toxicity in SH-SY5Y cells. Ca<sup>2+</sup> signalling causes transient changes in cytosolic Ca<sup>2+</sup> concentration. Mitochondria rapidly take up Ca<sup>2+</sup> when a physiological stimulus elicits an increase in cytosolic Ca<sup>2+</sup> concentrations. This uptake machinery allows mitochondria to act as “Ca<sup>2+</sup> buffers” to maintain the normal homeostasis. A $\beta$  destabilize intracellular Ca<sup>2+</sup> homeostasis as well as localize to mitochondrial membranes, block the transport of nuclear-encoded mitochondrial proteins to mitochondria, interact with mitochondrial proteins, disrupt the electron transport chain, increase reactive oxygen species (ROS) production, cause mitochondrial damage, and eventually induce the neurodegeneration or cell death (Figure 3-10, Right) [112-114]. The magnetic modulation of VDAC2 should block the localization of A $\beta$  to the mitochondria, whereas promote the Ca<sup>2+</sup> uptake into mitochondria within the threshold. Consequently, mitochondria should be able to maintain its functions like the ATP production and other energy-dependent function (Figure 3-10, Left). In the previous studies, we reports that magnetic stimulation can lead to changes in a wide range of cellular properties, such as cell shape, cytoskeletal organization, and cell fate [115,116]. And also, some other groups demonstrated that activation of ion channels is possible by using nanoscale magnetic particles [117-119]. Magnetic modulation of mitochondrial VDAC plays key role in various Ca<sup>2+</sup> influx and efflux pathways should provide attractive targets for future development of AD treatments.

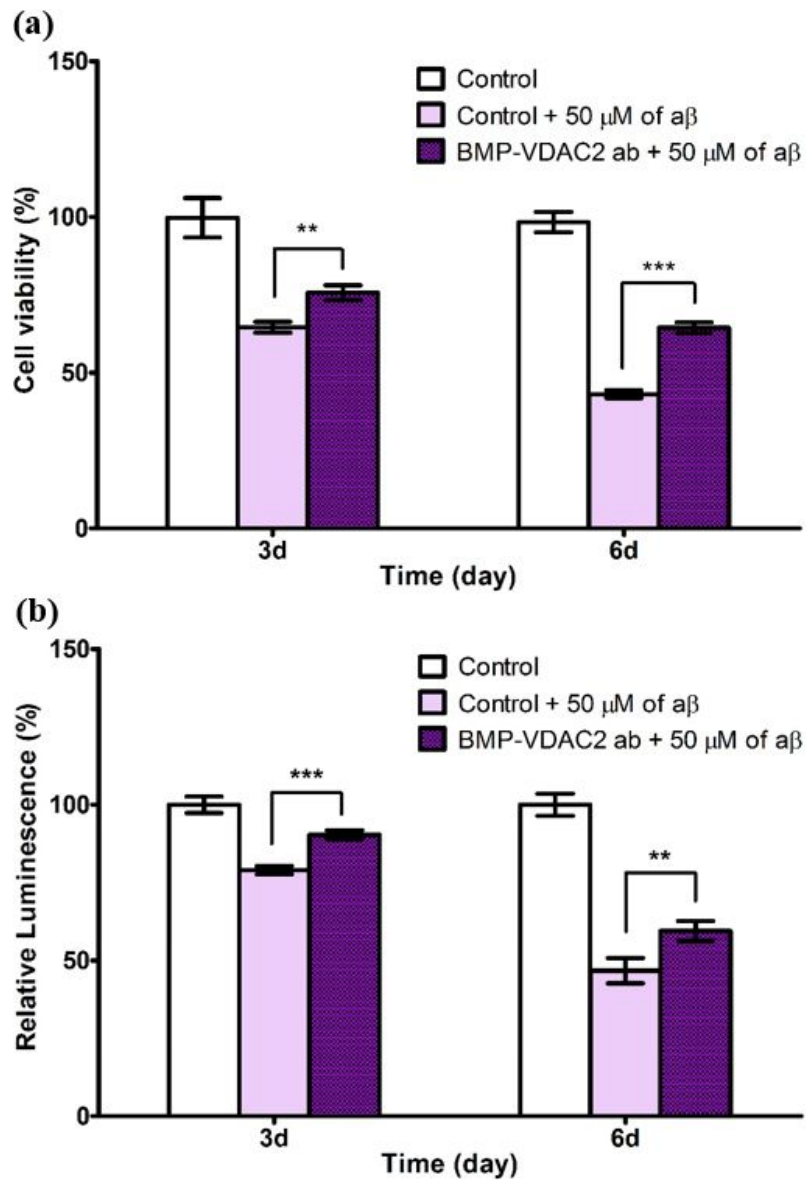


**Figure 3-9** Effect of BMP-VDAC2 Ab complex on cell growth by (a) MTS assay and (b) ATP level. Control: VDAC2 untargeted cells, BMP-VDAC2 ab: VDAC2 targeted cells with BMPs, Control + 50  $\mu\text{M}$  of  $\text{a}\beta$ : amyloid-beta treated VDAC2 untargeted cells, and BMP-VDAC2 ab + 50  $\mu\text{M}$  of  $\text{a}\beta$ : amyloid-beta treated VDAC2 targeted cells. (\* $p$ <0.05, \*\* $p$ <0.01, and \*\*\* $p$ <0.001,  $n$ =4)

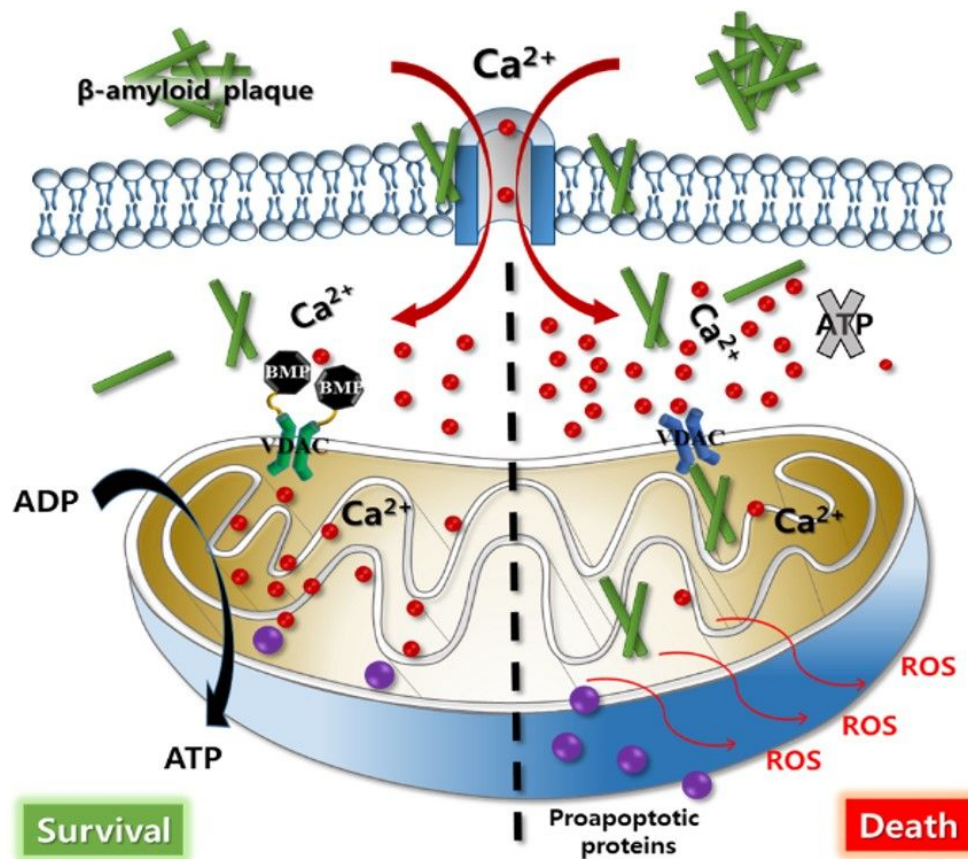


**Figure 3-10** Schematic map of mitochondrial  $\text{Ca}^{2+}$  transporters in the amyloid-beta induced toxicity.  $\text{A}\beta$  results in elevated cytosolic calcium levels and localize to mitochondrial membranes.  $\text{A}\beta$  in mitochondria inhibits mitochondrial ATP production and other energy-dependent functions, and releases calcium stored in mitochondria, thereby further deregulating neuronal calcium signaling. Finally, a release of proapoptotic proteins from damaged mitochondria results in neuronal injury. However, the magnetic modulation of VDAC2 should block the localization of  $\text{A}\beta$  to the mitochondria, whereas promote the  $\text{Ca}^{2+}$  uptake into mitochondria within the threshold. Mitochondria produce ATP and maintain other functions.

### **3.1.3 Summary**

BMPs-VDAC2 antibody complexes (BMPs-Ab) introduced into SH-SY5Y cells were successfully internalized into SH-SY5Y cells. The capture of VDAC2 with BMPs-Ab was significantly decreasing the expressed intracellular calcium levels induced by A $\beta$ . This magnetic modulation of VDAC2 considerably increases the proliferation and reduced A $\beta$ -induced toxicity in SH-SY5Y. These results suggest that magnetic modulation of VDAC-2 is able to protect the neurodegenerative disease attenuating the changes in the intracellular calcium levels that were induced by A $\beta$ .

### **3.2 Bacterial Magnetic Nanoparticle–Decorated Single-Wall Carbon Nanotubes**

Carbon nanotubes (CNTs) have emerged as a leading nanomaterial for biomedical applications because of their extraordinary properties, which make them useful as delivery vehicles for drugs, proteins, and DNA into cells [120-126]. While CNTs have proven useful in biological systems, negative effects, such as inflammatory responses, oxidative stress, free radical formation and peroxidative product accumulation, have also been observed for CNTs and their accumulated aggregates [127-134]. Therefore, it is necessary to characterize the toxicity and biocompatibility of CNTs and to identify their biodegradation and elimination pathways before they can be used in biomedical applications. Great attention has been paid to the construction and discovery of novel enzyme mimetic nanomaterials, which have significant advantages for controlled preparation at low cost, flexibility in structural design and composition, and tunable catalytic activities.

Recently, it was found that magnetic nanoparticles ( $\text{Fe}_3\text{O}_4$ ) possess intrinsic peroxidase-like catalytic activity, thus opening the door for the development of nanoscale materials in the biochemical field [135]. Since this discovery, various inorganic nanomaterials have been reported to have peroxidase-like catalytic activities [136,137]. Some recent reports showed that carboxyl-modified graphene oxide (GO) and single-wall carbon nanotubes (SWNTs) display intrinsic peroxidase-like activities, such that they could catalyze 3,3',5,5'-tetramethylbenzidine (TMB) to produce a blue-colored product in the presence of  $\text{H}_2\text{O}_2$  [138-140]. The results clearly showed that the observed “catalytic” effect could be attributed to the intrinsic properties of these materials rather than any metal residues.<sup>31</sup> Several hybrid complexes with inorganic nanomaterials incorporated within different matrices have been constructed and have proved to be highly efficient catalyst systems in various organic transformation reactions [141,142]. Typically, hemin–graphene hybrid

nanosheets and a magnetic nanoparticle/multi-walled carbon nanotube nanocomplex are exploited for their peroxidase-like catalytic activities [143,144]. However, it is rare to find research on the characterization and use of the degradation effect caused by the catalytic activity of the nanoparticles embedded in carbon-based structures. To the best of our knowledge, this is the first study to demonstrate effective *in vitro* degradation of biocompatible bacterial magnetic nanoparticle (BMP)-decorated SWNTs and their real application in neurobiology. The BMPs employed in this study are ferrimagnetic nanoparticles ( $\text{Fe}_3\text{O}_4$ ) wrapped with a stable lipid membrane containing lipids and proteins [116,145]. Therefore, they are inherently biocompatible and disperse well in aqueous solutions. These biocompatible BMPs were directly conjugated through covalent bonding to functionalized SWNTs (f-SWNTs) (Figure 3-11). Furthermore, BMPs act as a highly effective intrinsic peroxidase for the self-degradation of BMP-decorated f-SWNTs, showing that they are a suitable material for biological applications. Finally, we investigated the effect of self-degradable hybrids on the aggregation of amyloid-beta ( $\text{A}\beta$ ) peptides as a further neuro-therapeutic application. A thioflavin T assay was performed to prove the ability of these hybrids to inhibit amyloid-beta fibrils formation, which is considered the key process in Alzheimer's disease. In addition, under the amyloid-beta-induced neurotoxic conditions, the cell survival rate of SH-SY5Y cells, human-derived neuroblasts, which are often used as *in vitro* models of neuronal function and differentiation, was investigated in the presence of the hybrids. Our findings in this research suggest possible applications of CNTs in neurobiology, while eliminating the negative effects of CNTs that are anticipated based on previous studies.

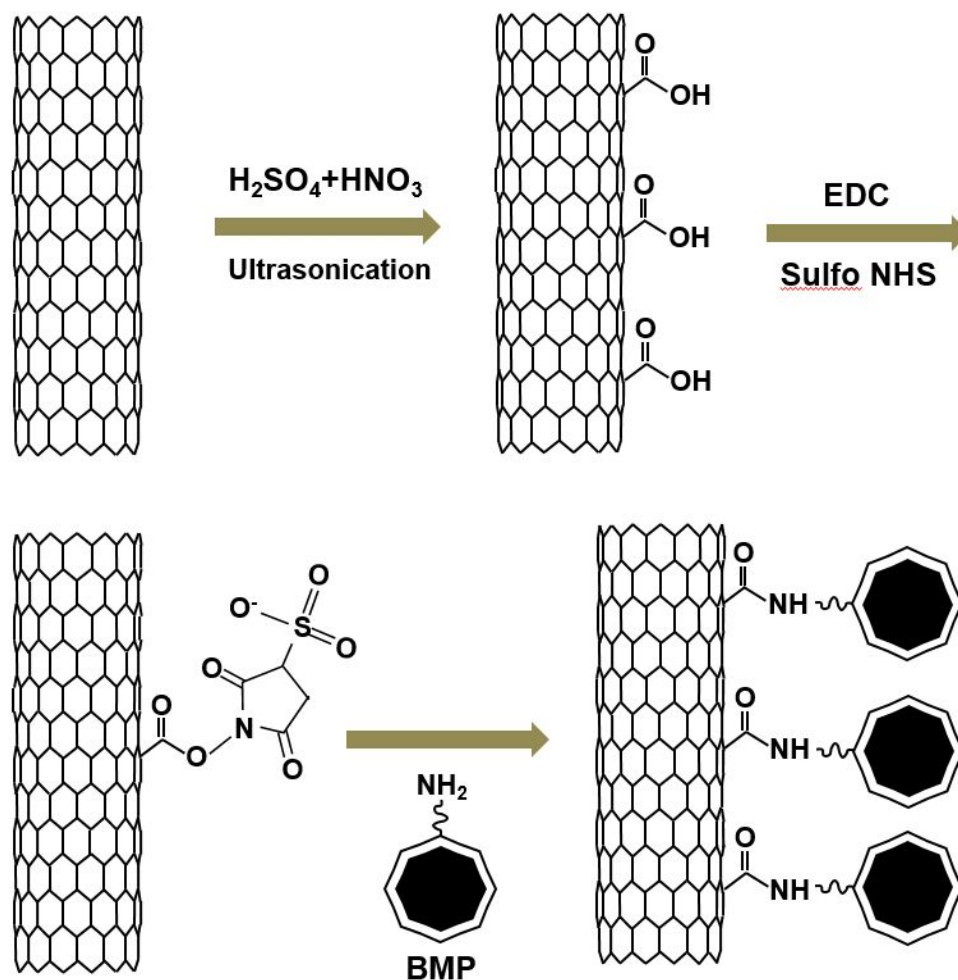


**Figure 3-11** Illustration of f-SWNT-BMP hybrid formation. EDC and sulfo-NHS are used to activate carboxyl groups of f-SWNTs. BMPs directly conjugated with f-SWNTs using their primary amine groups.

### **3.2.1 Materials and Methods**

#### **3.2.1.1 Carboxyl functionalization of SWNTs**

A quantity of 10 mg of SWNTs (ASP-100F) was added to a mixture of concentrated sulfuric acid (15 ml) and nitric acid (5 ml) and ultrasonicated for more than 24 h. A volume of 200 ml of deionized (DI) water was then added to the mixture. The diluted mixture was filtered using a 70- $\mu\text{m}$  filter to eliminate any unnecessary SWNT aggregates. A second filtering step was performed using 2- $\mu\text{m}$  filter paper to harvest functionalized SWNTs (f-SWNTs). Any remaining toxic ingredients and additives were removed by washing several times using excess DI water. After sufficiently washing the filter paper, the remaining f-SWNTs on the filter paper were placed into 1 ml of DI water and vortexed for 3 min to disperse the f-SWNTs into solution.

#### **3.2.1.2 BMP extraction and purification**

BMPs were obtained from *Magnetospirillum* sp. AMB-1 (ATCC® 700264) that was cultured in magnetic spirillum growth medium (MSGM) for 5 days in a shaking incubator at 30 °C under anaerobic conditions. Cultured *Magnetospirillum* sp. AMB-1 were centrifuged for 25 min at 5,000 rpm and then lysed by sonicating (VCX500, Sonics & Materials, USA) for 30 min. BMPs were collected using a neodymium-iron-boron (NdFeB) magnet and then washed 5 times with 1X PBS. The collected BMPs were dispersed in 1X PBS and sterilized by autoclaving (121 °C, 15 min). The concentration of the extracted BMPs was determined using an inductively coupled plasma-atomic emission spectrometer (ICP-AEX, ICPS-7500, Shimadzu, Japan).

#### **3.2.1.3 Conjugation of f-SWNTs to BMPs**

A quantity of 4 mg of N-(3-dimethylaminopropyl)-N'-ethylcarbodiimide hydrochloride -

ride (EDC, Sigma-Aldrich, Korea) and 11 mg of N-hydroxysulfosuccinimide sodium salt (Sulfo-NHS, Sigma-Aldrich, Korea) were dissolved in 100  $\mu$ l of 0.5 M and 0.1 M MES buffer (2-(N-morpholino) ethanesulfonic acid, pH = 8.3), respectively. The mixture was then added to 1 ml of 1 mg/ml carboxylated SWNTs for reaction with a carboxyl group for 15 min to form an amine-reactive O-acylisourea intermediate. After adjusting the pH (ranging from 7 to 8) by adding 30  $\mu$ l of 20X PBS buffer, the solution was mixed with 10  $\mu$ l of 1 mg/ml BMPs contained in 1X PBS and placed on a shaker at room temperature for 2 h to accelerate the binding reaction. Unconjugated f-SWNTs were separated from the f-SWNT-BMP conjugates three times in 1X PBS buffer under a strong magnetic field.

#### **3.2.1.4 High-resolution transmission electron microscopy**

The morphologies of the f-SWNT-BMP hybrids were analyzed using a high-resolution transmission electron microscope (HR-TEM; JEM-3000F, JEOL, Japan) operated at 300 kV. HR-TEM samples were prepared by placing a drop of the hybrid, dispersed in ethyl alcohol, on a 200-mesh holey carbon-coated copper grid. The samples were then dried at room temperature.

#### **3.2.1.5 EDS/FE-SEM preparation**

Energy dispersive X-ray spectroscopy (EDS) analysis was performed using a field-emission scanning electron microscope (FE-SEM; SUPRA 55VP, Carl Zeiss, Germany) with an X-ray microanalysis instrument operated at 30 kV. Samples for EDS/FE-SEM were prepared by drying a drop of each sample dispersed in DI water on a silicon wafer at 70 °C for 10 min. The samples were introduced into the vacuum chamber, and the X-ray spectra were acquired within minutes.

#### **3.2.1.6 XPS analysis**

X-ray photoelectron spectroscopy (XPS) measurements were performed using a K-

Alpha (Thermo Scientific) system. A drop of each sample was placed on a cleaned silicon wafer and dried in an oven at 70 °C overnight. A K $\alpha$  aluminum (1486.6 eV) X-ray source was used with a beam diameter of approximately 400  $\mu$ m. The spectrometer energy was calibrated to the 3d5/2 electronic level of silver (368.2 eV) and the 2p3/2 electronic level of copper (932.8 eV). Low pressure in the sample chamber ( $6.5 \times 10^{-9}$  mbar) was used for the analysis.

#### **3.2.1.7 Raman microscopy of the f-SWNT-BMP hybrids**

Raman spectra were collected using a LabRam Aramis (Horiba Jobin-Yvon, France) spectrometer with an Ar-ion laser (514.532 nm) excitation source. A drop of each sample was loaded onto clean glass wafers and dried before analysis. Samples were focused using an optical microscope with a spot size of approximately 1  $\mu$ m. The excitation power was 1 mW, and the spectra were calibrated prior to acquisition using a glass wafer.

#### **3.2.1.8 Catalytic activity of f-SWNT-BMP hybrids**

Catalytic experiments were performed using 20  $\mu$ l of 1 mg/ml f-SWNT-BMP hybrid ( $\sim 7.2 \times 10^9$  nanoparticles in a reaction volume of 200  $\mu$ l) in a 25 mM NaH<sub>2</sub>PO<sub>4</sub> buffer solution with a 1.6 mM TMB substrate and 50 mM H<sub>2</sub>O<sub>2</sub>. The samples were allowed to react for 20 min at 40 °C and were centrifuged at 15,000 g for 10 min to collect the precipitate on the bottom of the tube. The supernatant solution from each tube was then transferred into a 96-well plate. A volume of 20  $\mu$ l of 0.18 M H<sub>2</sub>SO<sub>4</sub> was added to each sample to stop the catalytic reaction, and the optical absorbance was read at 450 nm (yellow color). For kinetic studies, the optical absorbance was read every 30 sec at 650 nm for 30 min at room temperature (blue color). To prevent unexpected signals from particles, we placed small magnets beside each well to hold particles near magnets.

#### **3.2.1.9 Degradation of f-SWNTs**

To demonstrate BMP-induced degradation, both f-SWNTs and f-SWNT-BMP hybrids were simply incubated in 200  $\mu\text{M}$   $\text{H}_2\text{O}_2$  for 24 h at 37  $^\circ\text{C}$ . For hMPO-induced degradation, a quantity of 5  $\mu\text{g}$  of human myeloperoxidase (hMPO) was mixed with 100  $\mu\text{l}$  of 1 mg/ml f-SWNTs suspended in 50 mM phosphate buffer containing 140 mM NaCl and 100  $\mu\text{M}$  diethylene triamine pentaacetic acid (DTPA), a transition metal chelator. Hydrogen peroxide was added at a rate of 200  $\mu\text{M}$  per hour for 5 h. Due to the loss of hMPO activity in the incubation system, the enzyme was replenished after 5 h, and the reaction mixture was maintained at 37  $^\circ\text{C}$  for 24 h. Sodium hypochlorite was added every hour to give concentrations of 200  $\mu\text{M}$  for 24 h at 37  $^\circ\text{C}$ .

#### **3.2.1.10 Thioflavin T assay for A $\beta$ fibril formation**

First, a 2.5 mM ThT stock solution was prepared by adding 8 mg of ThT to 10 ml of 1X PBS buffer and filtering through a 0.2- $\mu\text{m}$  syringe filter. This solution was stored in the dark. This stock solution was diluted into the 1X PBS buffer on the day of analysis to generate a 20  $\mu\text{M}$  ThT working solution and covered with aluminum foil. Then, 1 mg of A $\beta$  25-35 (Sigma Aldrich, Korea) was dissolved in DMSO to the final concentration of 10 mM. This A $\beta$  stock solution was diluted into 1X PBS buffer to generate 10, 50, and 100  $\mu\text{M}$  A $\beta$  and incubated at RT with gentle shaking for the proper amount of time. On the day of analysis, 5  $\mu\text{l}$  of the ThT working solution was mixed with 95  $\mu\text{l}$  of each A $\beta$  fibril formation in a black 96-well plate and measured using a Microplate Reader (Victor3, Perkin Elmer, USA). Fluorescence intensity was measured by excitation at 450 nm and emission at 485 nm.

#### **3.2.1.11 MTS assay for cell viability**

The 3-(4,5-dimethylthiazol-2-yl)-5-(3-carboxymethoxyphenyl)-2-(4-sulfophenyl) - 2H-tetrazolium (MTS) assay was performed to evaluate the hybrid cytotoxicity and cell viability. A human-derived cell line, SH-SY5Y (neuroblastoma), was used for

biocompatibility evaluation. The cells ( $5 \times 10^3$  cells/well) were seeded into a 96-well plate with 120  $\mu$ l of culture medium. After the cells were sufficiently cultured, 25  $\mu$ l of CellTiter 96® AQueous One Solution Reagent (Promega, USA) was added to each well. The plate was then incubated at 37 °C for 1–4 h in a humidified 5% CO<sub>2</sub> atmosphere, and the absorbance was recorded at 490 nm using a microplate reader (Sunrise, Tecan, Switzerland). All assays were performed in three separate experiments. The absorbance of the control cells was defined as 100% viability in every assay.

## 3.2.2 Results

### 3.2.2.1 Synthesis of the f-SWNT-BMP hybrid

The BMPs from the *Magnetospirillum sp.* AMB-1 used in our approach are inherently biocompatible, can be effectively conjugated with other biomolecules, and disperse well in aqueous solutions because of their stable lipid membrane surrounding the magnetic core [116,145]. The lipid membrane is rich in phosphatidyl-ethanolamine (approximately 29%), which provides amine-binding sites, making the BMPs easy to disperse and conjugate to other biomolecules, such as antibodies, enzymes, and polypeptides. Therefore, we could make our hybrids via a very simple method. We used these lipid bilayer functional groups to directly link with the CNTs via a common conjugation method without any functionalized process involving BMPs. SWNTs were functionalized through covalent modification by attaching carboxyl groups ( $-\text{COOH}$ ) to the SWNT surfaces in acidic solutions [146]. The BMPs were conjugated to the f-SWNTs with 1-ethyl-3-[3-dimethylaminopropyl]carbodiimide hydrochloride, which facilitates carboxyl-to-amine conjugation (Figure 3-11). Direct evidence of the conjugation of BMPs to the f-SWNTs was obtained by magnetic attraction. After functionalization, the f-SWNTs and the hybrids were fully dispersed in DI water. However, the hybrids were mutually attracted to each other and aligned with their opposite magnetic poles facing opposing f-SWNTs within the one-minute interval. Electron microscopy images were used to confirm the arrangement of BMPs on the f-SWNTs surfaces (Figure 3-12). The morphological features of the hybrids significantly differed from those of the f-SWNTs with a clean surface. As shown in Figure 3-12(b) and (d), elongated nanoparticles with spatially isolated features uniformly decorated the surfaces of individual f-SWNTs and/or small f-SWNT bundles. Furthermore, these elongated BMPs were mostly aligned on the nanotubes, although some exceptions were also observed.

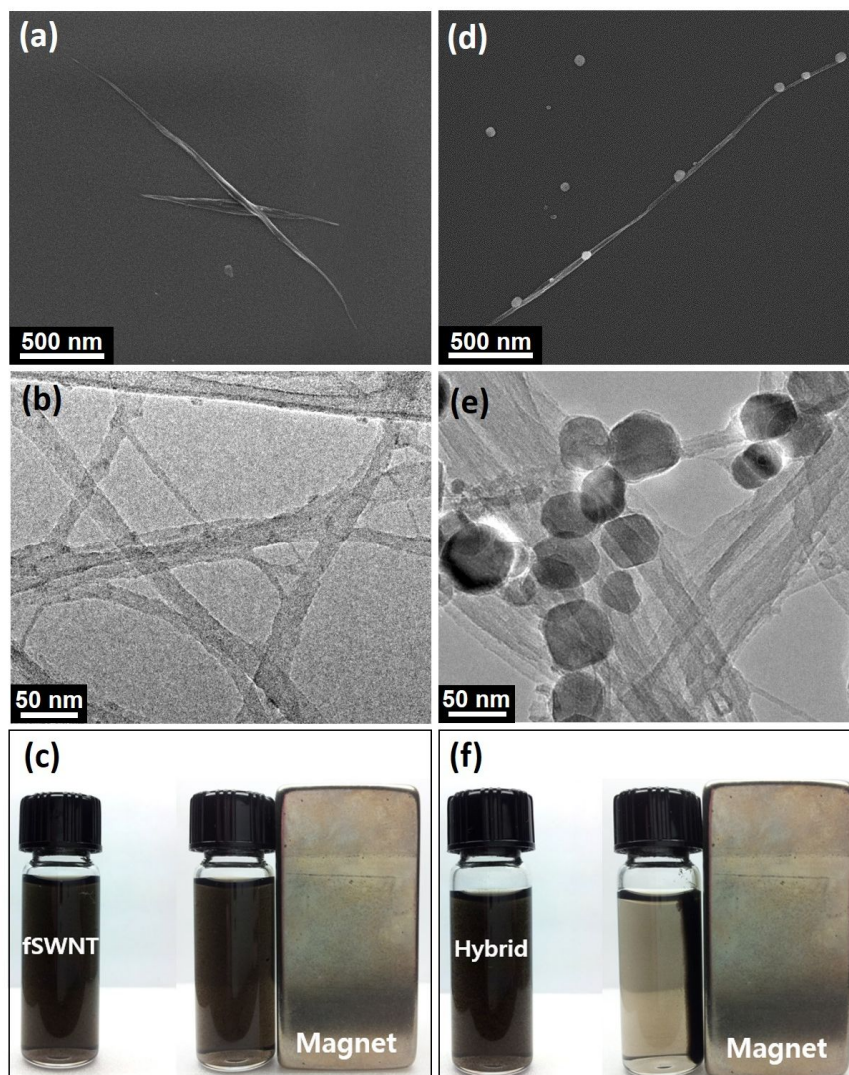


**Figure 3-12** Micrograph of f-SWNTs and f-SWNT-BMP hybrids (a), (b), (d), and (e). BMPs dangle from the f-SWNT bundles in the hybrid images (d) and (e), whereas only f-SWNTs are seen in images (a) and (b). Magnetic attraction of f-SWNTs (c) and f-SWNT-BMP hybrids (f) was performed. After functionalization, the f-SWNTs and the hybrids were fully dispersed in DI water. However, the hybrids were mutually attracted to each other and aligned with their opposite magnetic poles facing opposing f-SWNTs within a one-minute interval.

### 3.2.2.2 Characterization

Figure 3-13(a) shows the Raman spectra for the unmodified SWNTs, f-SWNTs, and f-SWNT-BMP hybrids used to identify the characteristic peaks. When the unmodified SWNTs were compared with the f-SWNTs, the intensity of the G peak for the f-SWNTs and the hybrids showed no noticeable change; however, the intensity of the D peak was enhanced drastically, resulting in an increased intensity ratio of the D to G band ( $I_D/I_G$ ). The D-band intensity measures the amount of  $sp^3$  defects introduced by covalent addend binding; in general, a covalent attachment would lead to a drastic increase in the D-peak intensity [147]. For the f-SWNTs, the D/G ratio significantly increased, which was attributed to the generation of carboxyl and hydroxyl groups during the treatment process. These results suggest that the route described here is a desirable approach for covalently attaching BMPs to the side walls; EDS/FE-SEM analysis confirmed the conjugation of BMPs onto the f-SWNT surface with C, O, and Fe on the surfaces of the hybrids (Fig. 3-13(b)). The Fe signals would have originated from the BMPs because most impurities, including Ni, Co, and Fe, that had been used as catalysts during the synthesis of the f-SWNTs were removed during the functionalization process (Fig. 3-13(c)). These results were further confirmed with XPS analysis. The expanded spectra of Fe 2p in Fig. 3-14(a) show the characteristic binding energy peaks of Fe 2p<sub>3/2</sub> and Fe 2p<sub>1/2</sub> of Fe<sub>3</sub>O<sub>4</sub> [148]. As shown in Fig. 3-14(b), the 400.1 eV peak was assigned to the residual amino groups on the surface of the Fe<sub>3</sub>O<sub>4</sub>, and the 401.0 eV peak was assigned to the amide groups in the hybrids [149].

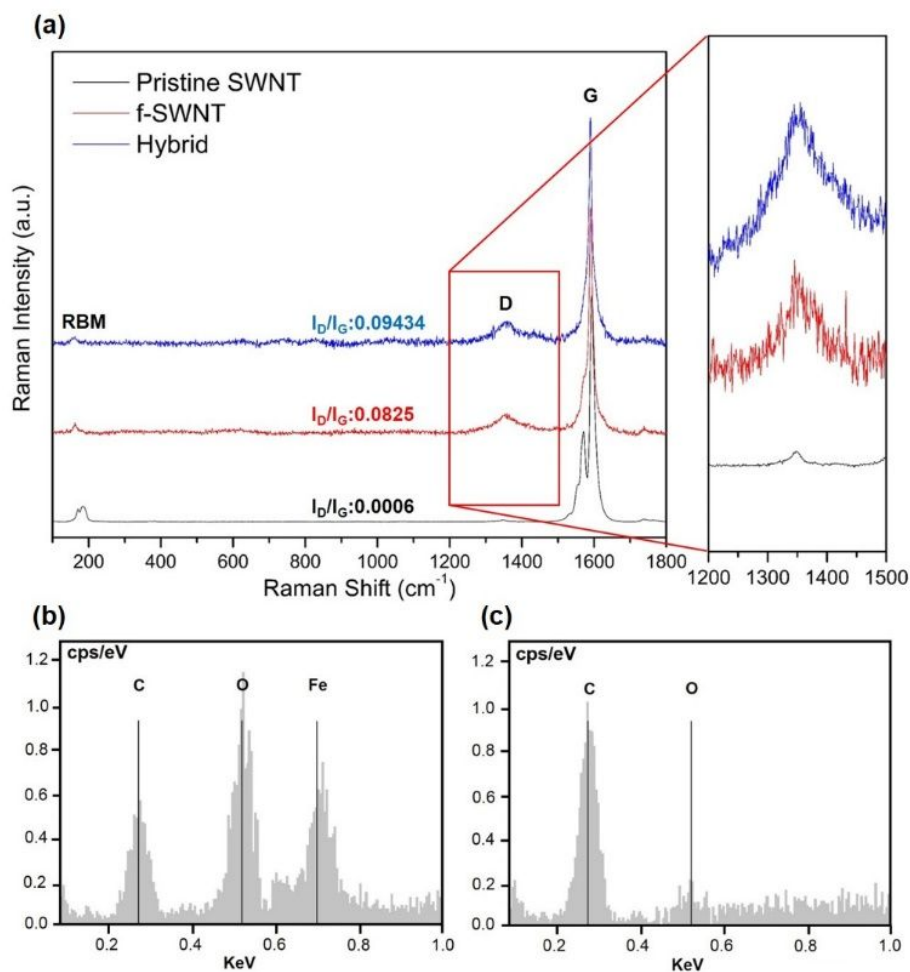


**Figure 3-13** Raman spectra (a), EDS results of f-SWNT-BMP hybrids (b) and f-SWNTs (c). When the unmodified SWNTs (pristine) were compared with the f-SWNTs, the intensity of the G peak for the f-SWNTs and the hybrids showed no noticeable change; however, the intensity of the D peak increased drastically, resulting in an increased intensity ratio of the D to G band (a). Inset: Starting from the bottom, the D peak of pristine SWNT, f-SWNT, and hybrid. The Fe signals would have originated from the BMPs (b) because most impurities, including Ni, Co, and Fe, that were used as catalysts during the synthesis of the f-SWNTs were removed during the functionalization process (c).

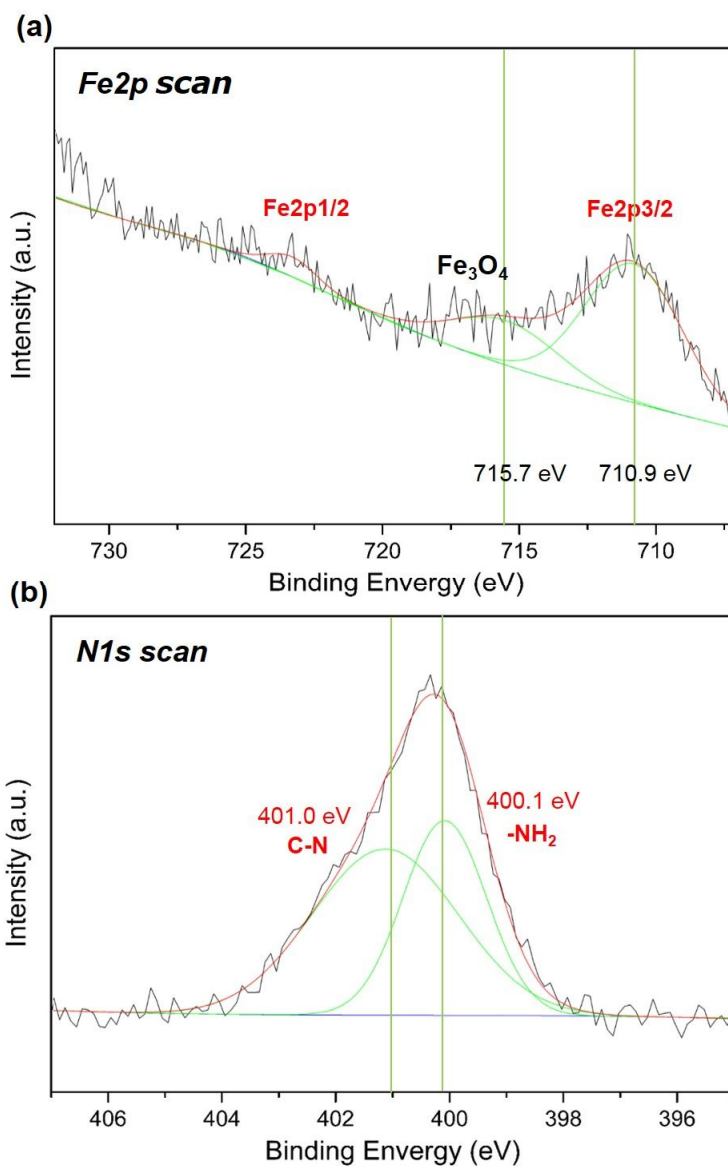


**Figure 3-14** XPS analysis of the Fe2p peak and the N1s core level of the hybrids. Fe2p scan showing the characteristic binding energy peaks of Fe 2p<sub>3/2</sub> and Fe 2p<sub>1/2</sub> of Fe<sub>3</sub>O<sub>4</sub> (a). In the N1s scan, the 400.1 eV peak was assigned to the residual amino groups on the surface of Fe<sub>3</sub>O<sub>4</sub>, and the 401.0 eV peak was assigned to the amide groups in the hybrids (b).

### 3.2.2.3 Catalytic activity of the hybrids as a peroxidase

We analyzed the mimetic peroxidase activity of the BMPs and the hybrids by measuring the extent of oxidation for a TMB peroxidase substrate by  $\text{H}_2\text{O}_2$  treatment to the oxidized product, indicated by a change to blue color observed at a wavelength of 650 nm. The TMB/  $\text{H}_2\text{O}_2$  system without hybrids or BMPs was colorless (Figure 3-15(a)), while the BMPs/ TMB/  $\text{H}_2\text{O}_2$  system produced a deep blue color (Figure 3-15(b)). Furthermore, hybrid added system produced a deeper blue color than BMPs system (Figure 3-15(c)). These results confirm that BMPs show peroxidase- like activity toward TMB, and the hybrid enhances such activities. To further characterize the peroxidase-like activity of hybrids, a series of experiments were performed by changing the concentration of BMPs while maintaining a constant concentration of the SWNTs (0.1mg/ml) for formation of hybrids. Interestingly, we found that the peroxidase-like activity was significantly enhanced upon the formation of the BMP-SWNT hybrids (Figure 3-15(d)). Figure 3-15(e) shows the time-dependent peroxidase-like activity changes against BMPs and hybrids. The colour change for the hybrid solution was much faster, and resulted in a higher peroxidase-activity than that from the BMPs alone (Figure 3-15(e)). SWNTs possess a high surface-to-volume ratio, as well as high affinity for hydrophobic molecules, such as TMB, that may increase the local concentration of the substrate and improve the catalytic effect. As shown in Figure 3-15(f), the catalytic activity of hybrids is dependent on the concentration of  $\text{H}_2\text{O}_2$ . Moreover, the hybrids quickly catalyzed the oxidation of the TMB peroxidase substrate and induced a rapid initial reaction rate and a subsequent stable stage depending on the concentration of  $\text{H}_2\text{O}_2$  (Figure 3-15(g)). Like the natural enzyme catalyzed reaction, the catalyzed reaction of hybrids is inhibited at high  $\text{H}_2\text{O}_2$  concentration. These results support the idea that the hybrids exhibit peroxidase-like behavior towards typical peroxidase substrates, such as TMB.

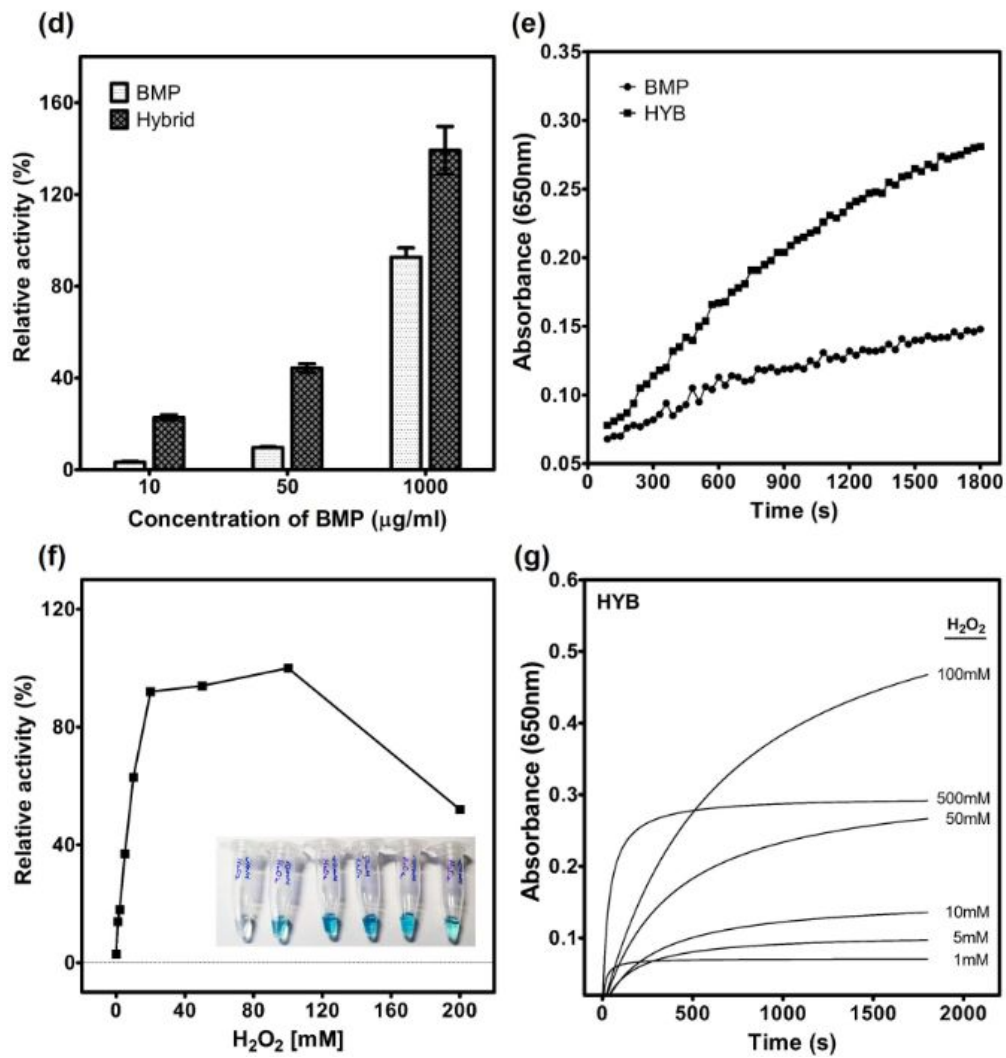
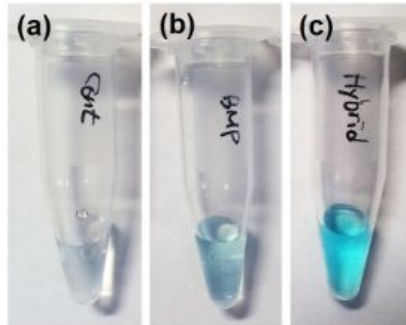


**Figure 3-15** Peroxidase-like activity of hybrids and dependence of the peroxidase-like activity on the  $\text{H}_2\text{O}_2$  concentration and the time-dependent absorbance changes at different  $\text{H}_2\text{O}_2$  concentrations. Color change of the TMB substrate in TMB +  $\text{H}_2\text{O}_2$  (a), TMB +  $\text{H}_2\text{O}_2$  + BMPs (b), and TMB +  $\text{H}_2\text{O}_2$  + Hybrids (c), Synergetic peroxidase-like activity of hybrids (d), Comparison of the time-dependent peroxidase-like activity changes with hybrids and BMPs (e). The catalytic activity of the hybrids is dependent on the concentration of  $\text{H}_2\text{O}_2$  (f). Moreover, the hybrids quickly catalyzed the oxidation of the TMB peroxidase substrate and induced a rapid initial reaction rate and a subsequent stable stage depending on the concentration of  $\text{H}_2\text{O}_2$  (g).

For further analysing the catalytic mechanism, the catalytic activity of hybrids was studied by enzyme kinetic of theory using  $\text{H}_2\text{O}_2$  and TMB as substrates. A series of experiments were performed by changing the concentration of one substrate and keeping constant the concentration of the other. Hybrid-catalysed reaction is inhibited at high  $\text{H}_2\text{O}_2$  concentrations like the enzyme catalysed reaction, however, within the suitable range of  $\text{H}_2\text{O}_2$  concentrations, typical Michaelis–Menten curves were observed (Figure 3-16). Maximum initial velocity ( $V_{\text{max}}$ ) and Michaelis–Menten constant ( $K_m$ ) were obtained using Lineweaver-Burk plot and are shown in Table 3-1 [135,150]. As a catalyst, our  $K_m$  value of hybrids with  $\text{H}_2\text{O}_2$  was comparable to that of HRP at the same molar concentration like a previously reported.<sup>25</sup> But compared with BMPs, the  $V_{\text{max}}$  value of hybrids with TMB and  $\text{H}_2\text{O}_2$  was almost two times higher than that of BMPs, while the apparent  $K_m$  value of hybrids with  $\text{H}_2\text{O}_2$  as the substrate was similar to that of BMPs. Since  $K_m$  is identified as an indicator of enzyme affinity to substrates, similar  $K_m$  values of BMPs and hybrids proved that the main peroxidase-like activity of hybrids originated from BMPs. However, incorporation of BMPs on SWNTs possess a high surface-to-volume ratio may increase the local concentration of the substrate and improve the catalytic velocity.

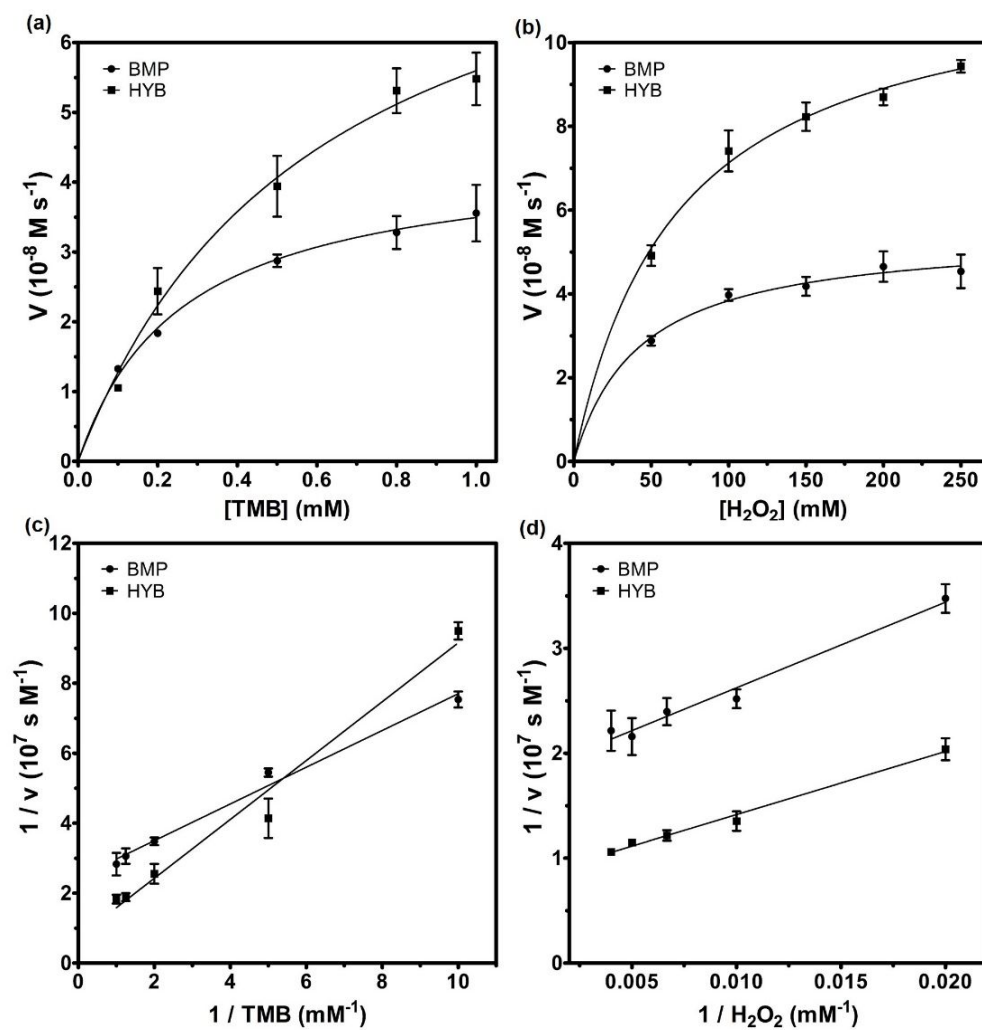


**Figure 3-16** Steady-state kinetic assay and catalytic mechanism of hybrids and BMPs. The concentration of  $\text{H}_2\text{O}_2$  was 50mM and the TMB concentration was varied (a), and the concentration of TMB was 1.6 mM and the  $\text{H}_2\text{O}_2$  concentration was varied (b). Double reciprocal plots of activity of hybrids and BMPs with fixed concentration of  $\text{H}_2\text{O}_2$  and varied TMB concentrations (c), and with the fixed concentration of TMB and varied  $\text{H}_2\text{O}_2$  concentrations (d).

**Table 3-1** Comparison of the apparent Michaelis–Menten constant ( $K_m$ ) and maximum reaction rate ( $V_{max}$ ) between hybrids and BMPs

Catalyst	$K_m$ [mM]		$V_{max}$ [ $10^{-8}$ M s <sup>-1</sup> ]	
	TMB	H <sub>2</sub> O <sub>2</sub>	TMB	H <sub>2</sub> O <sub>2</sub>
BMP	0.26±0.04	42.1±7.6	4.4±0.23	5.4±0.24
HYB	0.60±0.13	66.5±6.9	8.9±0.96	11.8±0.39

#### 3.2.2.4 Self-degradation of BMP-Decorated f-SWNTs

Previously, it was shown that the human neutrophil enzyme myeloperoxidase (hMPO) catalyzes the biodegradation of single-walled carbon nanotubes *in vitro* [151]. Gao *et al.* found that Fe<sub>3</sub>O<sub>4</sub> magnetic nanoparticles could be used as an intrinsically active catalyst for some oxidation reactions [135]. BMPs with magnetic cores composed of Fe<sub>3</sub>O<sub>4</sub> can also act as an effective intrinsic peroxidase. Based on these findings, we attempted to demonstrate the degradation of BMP-decorated f-SWNTs using the intrinsic mimetic enzyme activity of the BMPs, which is similar to that found in magnetic nanoparticles. The f-SWNTs and f-SWNT-BMP hybrids were incubated with 200 μM H<sub>2</sub>O<sub>2</sub> for 24 h at 37 °C. TEM was used to track the morphological changes of the resulting BMP-induced degradation (Figure 3-17(a)-(d)). Most of the f-SWNTs remained bundled in the H<sub>2</sub>O<sub>2</sub> condition after 24 h of incubation (Figure 3-17(b)). Remarkably, the TEM images revealed that the majority of the hybrid bundles were degraded, leaving residual BMPs and carbonaceous material in the BMP-induced degradation samples under the same condition as the f-SWNTs (Figure 3-17(d)). These results strongly suggest that BMPs can act as a highly effective intrinsic peroxidase for SWNT degradation. The Raman spectra of the f-SWNTs and hybrid samples underscore the key function of the BMPs in the degradation process. After 24 h of H<sub>2</sub>O<sub>2</sub> treatment, the I<sub>D</sub>/I<sub>G</sub> ratio for the hybrids drastically increased compared with that for the f-SWNT sample due to the BMP-induced degradation (Figure 3-17(e) and (f)).

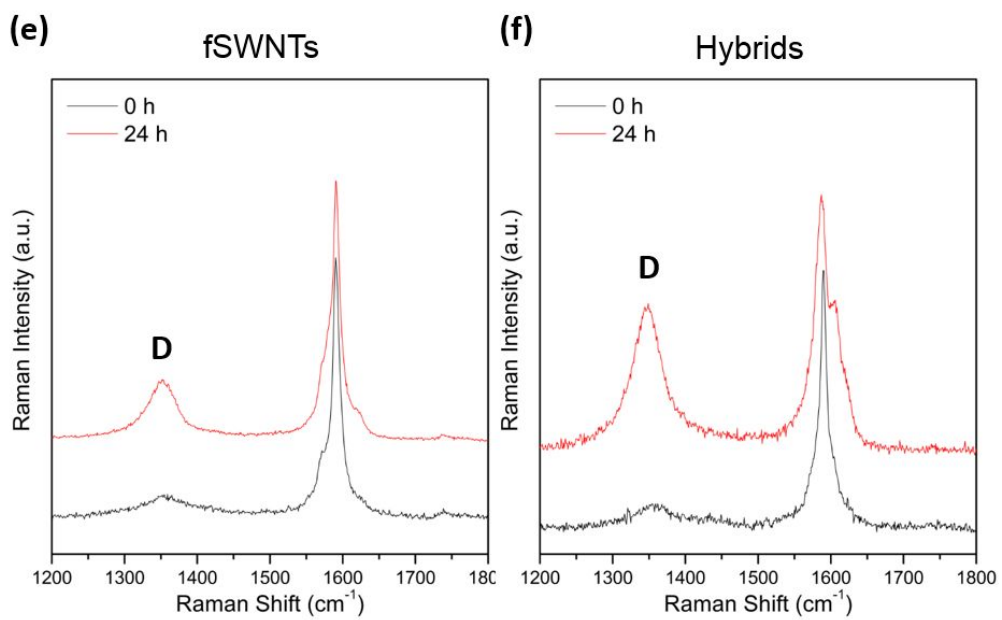
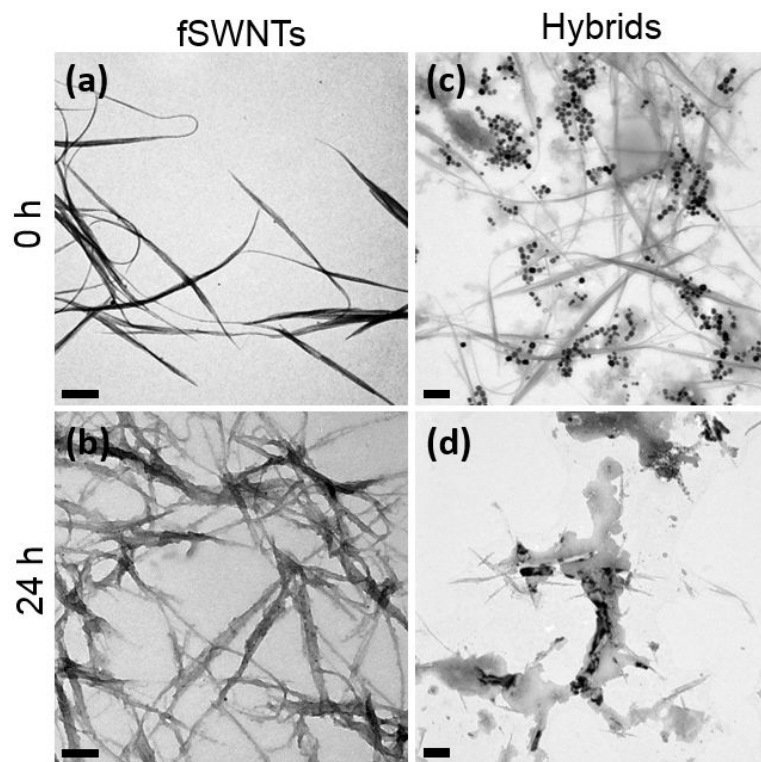


**Figure 3-17** TEM images (a)-(d) and Raman spectra (e) and (f). Most of the f-SWNTs remained bundled in the H<sub>2</sub>O<sub>2</sub> condition after 24 h of incubation (b), whereas the majority of the f-SWNT-BMP hybrid bundles were degraded, leaving residual BMPs and carbonaceous material in the samples after the BMP-induced degradation (d). Scale bars are 200 nm. In the Raman spectra, the I<sub>D</sub>/I<sub>G</sub> ratio for the hybrids drastically increased compared with that for the f-SWNT sample due to the BMP-induced degradation (e) and (f).

To compare the effect of BMP-induced SWNT degradation with other degradation methods, we also performed hMPO-induced SWNT degradation according to a previous method [151]. As shown in Figure 3-18, the intensity of the D-band for the hybrids under BMP-induced degradation was higher than that of the f-SWNTs under hMPO-induced degradation. The relative degradation ratio ( $I_D/I_G$ ) for the BMP-induced degradation (Figure 3-18(1)) was also higher than the hMPO-induced degradation (Figure 3-18(2)). In addition, in the Raman spectra for BMP-induced degradation, the hybrid showed clear disappearance of the radial breathing mode (RBM) at  $169\text{ cm}^{-1}$ , indicating the destruction of the tubular structures in the f-SWNTs.

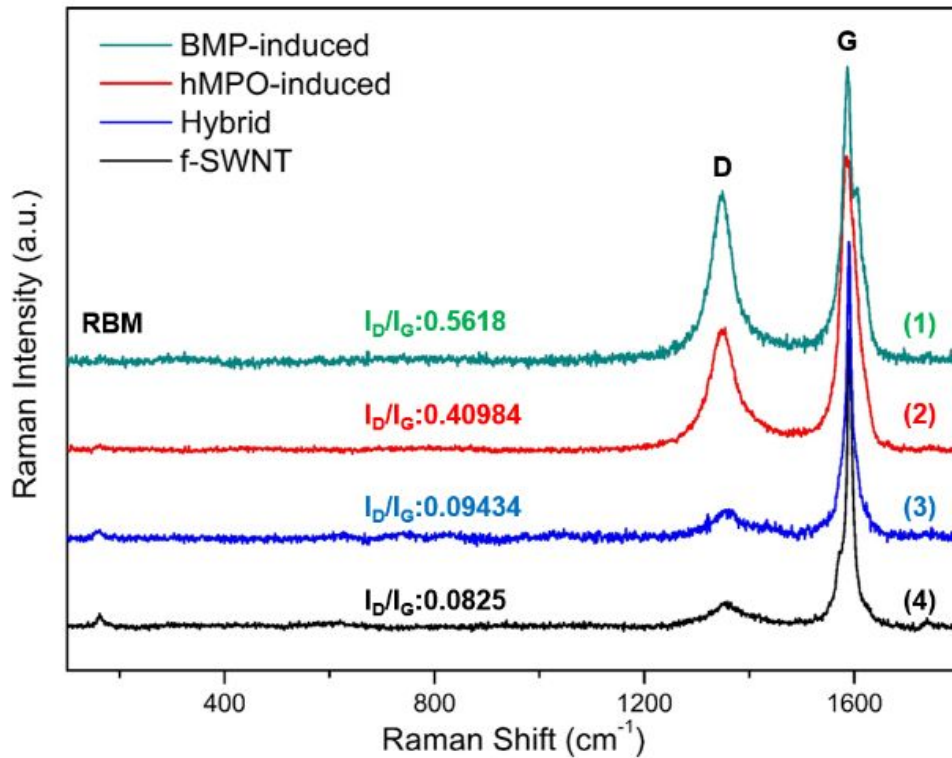


**Figure 3-18** Raman spectra of the hMPO-induced and BMP-induced degradation of f-SWNTs. The intensity of the D-band for the hybrids under BMP-induced degradation (1) was higher than that of the f-SWNTs under hMPO-induced degradation (2). The relative degradation ratio ( $I_D/I_G$ ) for the BMP-induced degradation was also higher than the hMPO-induced degradation. In addition, in the Raman spectra for BMP-induced degradation, the hybrid showed clear disappearance of the radial breathing mode (RBM) at  $169\text{ cm}^{-1}$ , indicating the destruction of the tubular structures in the f-SWNTs.

### 3.2.2.5 Inhibition of amyloid beta fibrillation

Recently, it was demonstrated that amyloid beta forms non-amyloid fibrils in the presence of carbon nanotubes [152]. According to this study, the interaction between the hydrophobic groups of the A $\beta$  peptide and SWNTs could attack the stability of the electrostatic network of the A $\beta$  peptide and lead to conformational changes in the peptide. The f-SWNT-BMP hybrids in this study are mainly composed of carbon nanotubes, including hydrophobic surfaces, so they may also act as inhibitors of the formation of A $\beta$  fibrils. Therefore, we investigated the effect of hybrids on the aggregation of A $\beta$  peptide using simple methods. To visualize A $\beta$  fibrils, FITC-labeled A $\beta$  antibodies were added to the samples after 7 days of A $\beta$  peptide incubation in the presence and absence of the hybrids. Figure 3-19(a) shows a fluorescence image of the A $\beta$  fibrils without hybrids, and it shows a strong signal compared with the A $\beta$  fibril sample in the presence of hybrids (Figure 3-19(b)). To further investigate this behavior, a thioflavin T (ThT) binding assay was also performed. ThT fluorescence is considered a highly sensitive marker for the amyloid state of various aggregating proteins and peptides. ThT in solution displays weak fluorescence in its free form but strong fluorescence when bound to amyloid fibrils [150]. The aggregation kinetics of 100  $\mu$ M A $\beta$  peptides were measured in the presence of 10  $\mu$ g/ml hybrids. In the presence of hybrids, we observed a quenching effect by the hybrid, as shown in Figure 3-19(c).

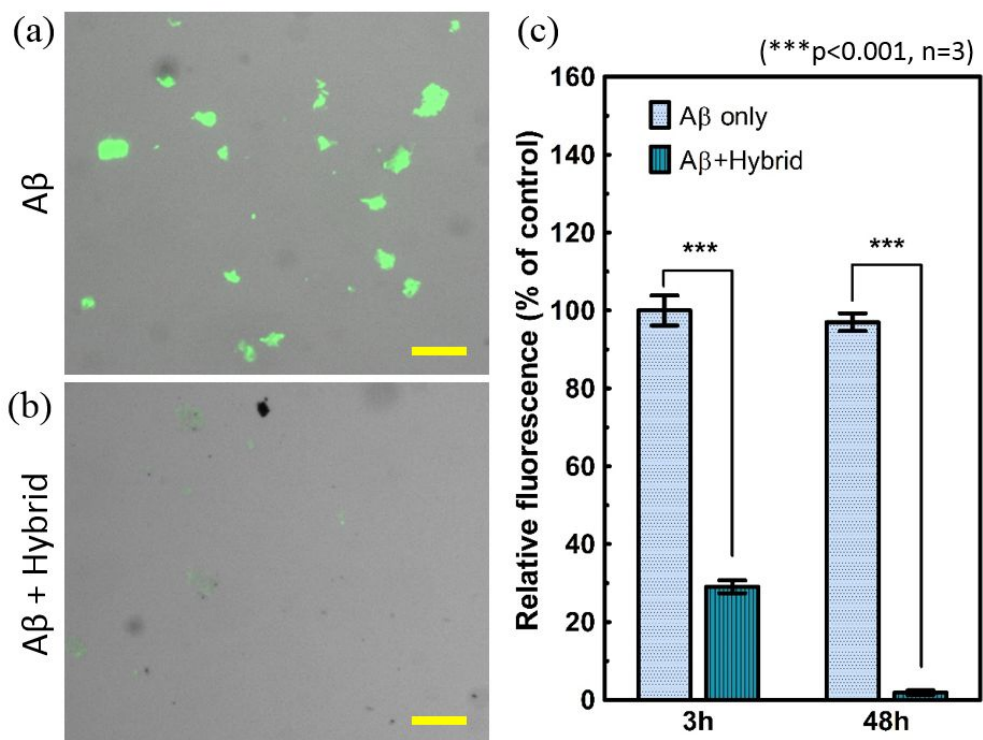


**Figure 3-19** Fluorescence images of A $\beta$  fibrils in the absence and presence of hybrids (a) and (b) and signal intensity comparison (c). To visualize A $\beta$  fibrils in solution, FITC-labeled A $\beta$  antibodies were combined with the samples after 7 days of A $\beta$  incubation. A fluorescence image of A $\beta$  without hybrids (a) shows a stronger signal than the A $\beta$  with hybrids (b). The scale bars are 10  $\mu$ m.

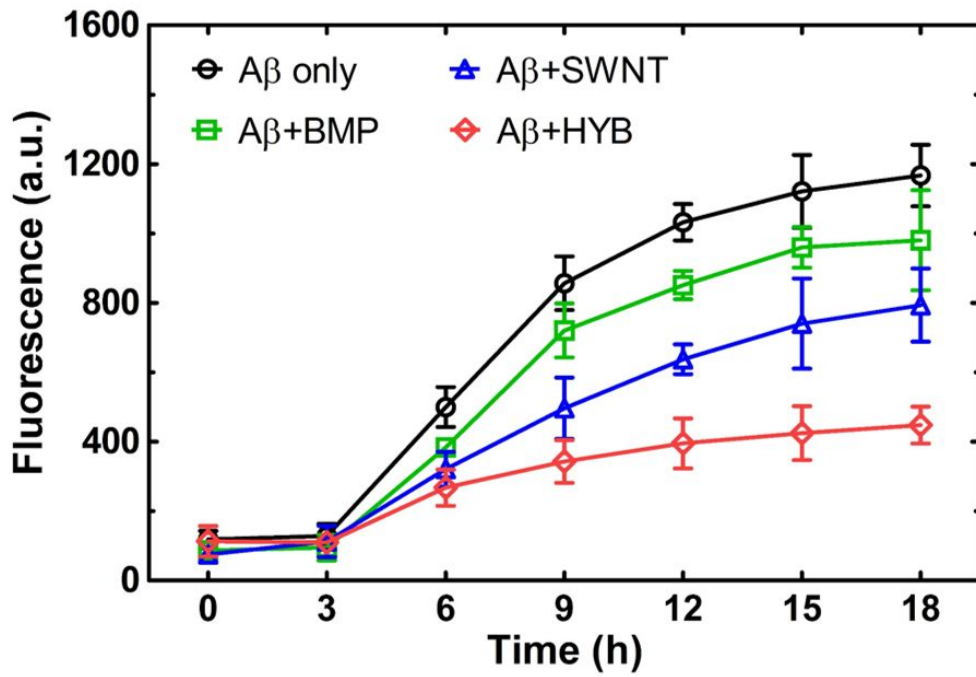


**Figure 3-20** ThT assay results of A $\beta$  only, A $\beta$  with BMP, SWNT and Hybrid. Here, we clearly observed a quenching effect, which reduces the fluorescence signal (red, blue, green dots). Meanwhile, the signal from the A $\beta$  without hybrids was greatly increased (black dots) during the 18 h of observation.

### 3.2.2.6 Prevention of A $\beta$ -induced neurotoxicity

For the purpose of using f-SWNT-BMP hybrids in neurobiology applications, it was necessary to first characterize the toxicity and biocompatibility of the hybrids. The cytotoxicity of the hybrids against the SH-SY5Y cells was evaluated using the MTS assay and normalized to the viability of the control cells without treatment with the hybrids (100% viability). Optical images captured by inverted microscopy show that there is no significant difference between without (Figure 3-20(a)) and with (Figure 3-20(b)) hybrids in the survival of the SH-SY5Y cells after 3 days of the 10  $\mu$ g/ml hybrids treatment. Moreover, the cytotoxic effects of the hybrids on the viability of the SH-SY5Y cells was also insignificant, even at a high concentration of 20  $\mu$ g/ml for  $1 \times 10^4$  cells within 3 days of the cell culture, which is ideal for using them in practical applications in the biomedical field (Figure 3-20(c)). To probe the effect of the hybrids on the neurotoxicity of the A $\beta$  fibrils, we measured the cell viability in the presence of A $\beta$  without and with hybrids. First, 200  $\mu$ M A $\beta$  in the presence and absence of 10 ng/ml hybrids was incubated at 37  $^{\circ}$ C for 3 days and added to growing SH-SY5Y cells. Interestingly, both the MTS and ATP assays in Figure 3-21 showed approximately 50% cell survival rates in the presence of the A $\beta$  fibrils, whereas more than 80% of cells survived in the presence of A $\beta$  with the hybrids (\*\*p<0.001, n=6). We assume that the hydrophobic surfaces of our f-SWNT-BMP hybrids may interact with the A $\beta$  peptides and inhibit A $\beta$  fibril formation, which causes cell death, so the cell survival rate increased in the presence of the hybrids. These results strongly supported the hypothesis that hybrids are able to reduce the toxicity of A $\beta$  peptides and inhibit their aggregation.

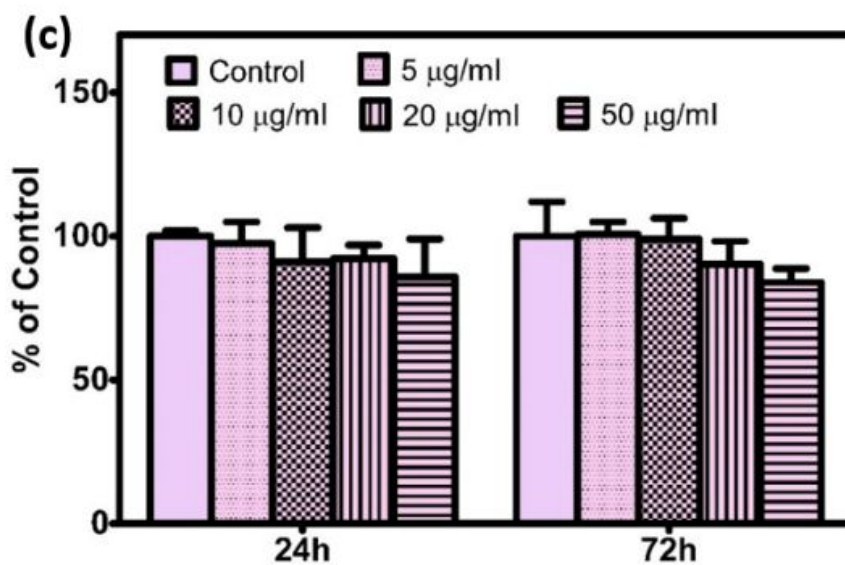
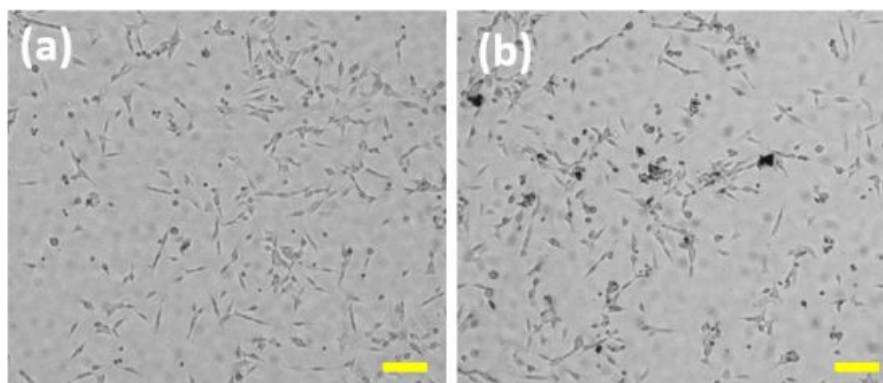


**Figure 3-21** Optical microscopy images of cultured SH-SY5Y cells with and without hybrids. We observed that there is no significant difference between without (a) and with (b) hybrids in the survival of the SH-SY5Y cells after 3 days of cell culture. The scale bars are 200  $\mu\text{m}$ . From the MTS assay, the cytotoxic effects of the hybrids on the viability of the SH-SY5Y cells were also insignificant, even at a high concentration of 20  $\mu\text{g/ml}$  (c).

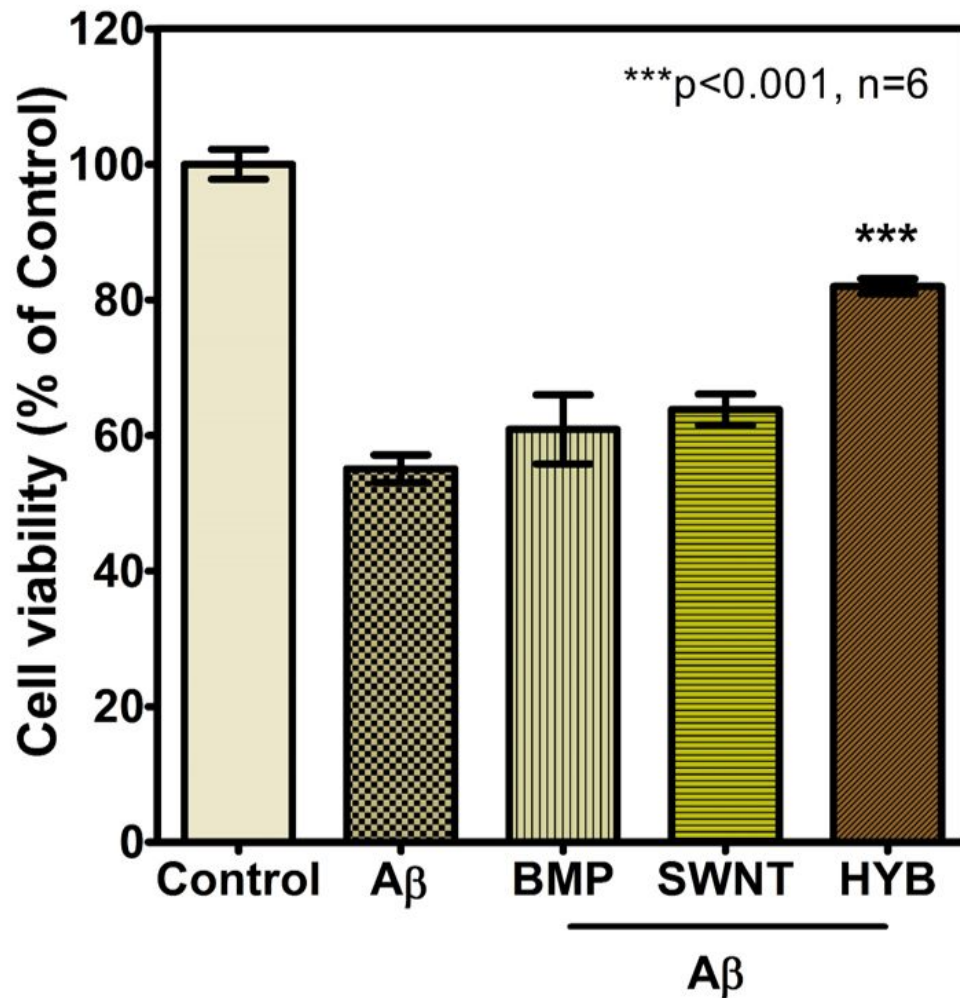


**Figure 3-22** Effect of the BMP, SWNT and hybrids on the SH-SY5Y cell growth under the amyloid-beta-induced neurotoxic condition by MTS assay. Control: untreated cells, A $\beta$ : 200  $\mu$ M A $\beta$ -treated cells, A $\beta$ +BMP: 200  $\mu$ M A $\beta$  and 10 ng/ml BMP-treated cells, A $\beta$ +SWNT: 200  $\mu$ M A $\beta$  and 10 ng/ml SWNT-treated cells and A $\beta$ +HYB: 200  $\mu$ M A $\beta$  and 10 ng/ml hybrids-treated cells. This results showed that the cell viabilities of the hybrid-treated cells increased by more than 30%.

### 3.2.3 Summary

The peroxidase-like characteristics of the  $\text{Fe}_3\text{O}_4$  magnetic nanoparticles have been previously employed in an attempt to replace the HRP enzyme that is typically used in  $\text{H}_2\text{O}_2$  detection and immunosorbent assays.  $\text{Fe}_3\text{O}_4$  magnetic nanoparticles have also been studied for application in the degradation of phenolic and aniline compounds. In this study, we reported the synthesis of biocompatible BMP-decorated f-SWNTs with intrinsic peroxidase-like activity. Moreover, the BMPs were found to function as a highly effective intrinsic peroxidase for SWNT degradation. In addition, the mimetic peroxidase catalytic activity of the hybrids that can transform a TMB peroxidase substrate, by  $\text{H}_2\text{O}_2$  treatment, into its oxidized state was shown to be significantly higher than that of pure BMPs. In addition, for possible application of this material in neurobiology, the f-SWNT-BMP hybrids were shown to be an inhibitor that reduces the aggregation of  $\text{A}\beta$  peptides, which is considered the key element behind Alzheimer's disease. To confirm this result, we showed that the neurotoxicity of  $\text{A}\beta$  fibrils (measured as the SH-SY5Y cell death) is reduced in the presence of these hybrids. This research could provide a new approach for the neurobiological application of CNTs without any of their toxic effects.

## Chapter 4 Conclusion

Cells are the basic structural and functional unit of living systems. It is hence important to understand the mechanism of how cells interact with the environment. Indeed, cells are sensitive to biochemical, mechanical, and topological cues. Our understanding of the mechanisms on how cells sense these cues and our ability to manipulate cellular behaviors accordingly will allow efficient and therapeutic intervention of related diseases and expedite the development of new methods for drug screening and discovery. Nano- micro- fabrication techniques are particularly useful in facilitating the research in this aspect by creating and mimicking the physiological and pathological cellular environment.

In this thesis, we report the effect of nano- micro- scale materials having various material property affecting cellular responses. For this purpose, micro-scale pillar array which has stepped structure with varying bottom diameter were fabricated by double step photolithography process. Single walled carbon nanotube and magnetic nanoparticle were also engineered to stimulate cellular behaviour. These materials were successfully embedded into cellular system to regulate its migration behaviour, morphology and viability. Our study could give a pioneer understanding regarding cellular response affected by nano- micro- scale systems.

First, we designed a new variation of the microfabricated polymeric pillar array platform that can decouple the stiffness gradient from the focal adhesion area of a

cell. This goal is achieved via a “stepped” micro pillar array device (SMPAD) in which the contact area with a cell was kept constant while the diameter of the pillar bodies was altered to attain the proper mechanical stiffness. Using double-step SU-8 mold fabrication, the diameter of the top of every pillar was manufactured to be identical, whereas that of the bottom was changeable, to achieve the desired substrate rigidity. Fibronectin is immobilized on the pillar tops, providing a focal adhesion site for cells. C2C12, HeLa and NIH3T3 cells were cultured on the SMPAD, and the motion of the cells was observed by time-lapse microscopy. Using this simple platform, which produces a purely physical stimulus, we observed that various types of cell behaviour are affected by the mechanical stimulus of the environment. We also demonstrated directed cell migration guided by a discrete rigidity gradient by varying stiffness.

Next, we demonstrate that the nano-scale magnetic modulation of mitochondrial VDAC2, which is the only mammalian-specific isoform among VDAC isoforms, can contribute to protect the neurodegenerative disease attenuating the changes in the intracellular calcium levels that were induced by beta-amyloid. In this study, BMPs originated from *Magnetospirillum* sp. AMB-1 directly conjugated with VDAC2 antibody using 1-Ethyl-3-(3-dimethylaminopropyl) carbodiimide (EDC) linker which is used to couple carboxyl groups to primary amines. BMPs-VDAC2 antibody complexes (BMPs-Ab) introduced into SH-SY5Y cells, human derived neuroblasts which are often used as *in vitro* models of neuronal function and differentiation. We investigated that the effect of magnetically modulated VDAC2 on the change of intracellular  $\text{Ca}^{2+}$  levels induced by  $\text{A}\beta$ . SH-SY5Y cells were loaded with 5  $\mu\text{M}$  Fluo-3 AM for 30 min, and then the changes in the level of  $\text{Ca}^{2+}$  before and after treatment with  $\text{A}\beta$  were measured by 488-nm laser source to excite Fluo-3. BMPs-VDAC2 antibody complexes (BMPs-Ab) introduced into SH-SY5Y cells were successfully internalized into SH-SY5Y cells. We found that the capture of VDAC2 with BMPs-Ab was significantly decreasing the expressed intracellular

calcium levels induced by A $\beta$ . This magnetic modulation of VDAC2 considerably increases the proliferation and reduced A $\beta$ -induced toxicity in SH-SY5Y. These results suggest that magnetic modulation of VDAC-2 is able to protect the neurodegenerative disease attenuating the changes in the intracellular calcium levels that were induced by A $\beta$ .

Finally, we investigated a self-degradation route for single-wall carbon nanotubes (SWNTs) mediated by built-in peroxidase-like activity of bacterial magnetic nanoparticles (BMPs). Biocompatible BMPs originated from *Magnetospirillum* sp. AMB-1 were directly conjugated through covalent bonding to yield functionalized SWNTs (f-SWNTs) without any additional functionalized processes. Employing transmission electron microscopy (TEM) and Raman spectroscopy, we found that BMPs can act as effective built-in intrinsic peroxidase compare to other enzymatic methods for the degradation of SWNTs. For the possible application in neurobiology, f-SWNT-BMP hybrids were shown as an inhibitor to reduce formation of amyloid-beta (A $\beta$ ) fibrils which is considered as the key element behind Alzheimer's disease. To conform this, we showed that neurotoxicity of A $\beta$  peptide affecting SH-SY5Y cell death is reduced in the presence of these hybrids. Our findings could offer a new approach of mitigating the toxic impact and neurobiological application of CNTs.

## Bibliography

- [1] C.S. Chen, M. Mrksich, S. Huang, G.M. Whitesides, D.E. Ingber, Geometric control of cell life and death, *Science* 276 (1997) 1425-1428.
- [2] L.E. Dike, C.S. Chen, M. Mrksich, J. Tien, G.M. Whitesides, D.E. Ingber, Geometric control of switching between growth, apoptosis, and differentiation during angiogenesis using micropatterned substrates, *In Vitro Cellular & Developmental Biology-Animal* 35 (1999) 441-448.
- [3] Y.T. Shiu, S. Li, S.L. Yuan, Y.X. Wang, P. Nguyen, S. Chien, Shear stress-induced c-fos activation is mediated by Rho in a calcium-dependent manner, *Biochemical and Biophysical Research Communications* 303 (2003) 548-555.
- [4] J. Dobson, Cancer Therapy Death by magnetism, *Nature Materials* 11 (2012) 1006-1008.
- [5] R. McBeath, D.M. Pirone, C.M. Nelson, K. Bhadriraju, C.S. Chen, Cell shape, cytoskeletal tension, and RhoA regulate stem cell lineage commitment, *Developmental Cell* 6 (2004) 483-495.

- [6] S.A. Ruiz, C.S. Chen, Emergence of Patterned Stem Cell Differentiation Within Multicellular Structures, *Stem Cells* 26 (2008) 2921-2927.
- [7] A.J. Engler, S. Sen, H.L. Sweeney, D.E. Discher, Matrix elasticity directs stem cell lineage specification, *Cell* 126 (2006) 677-689.
- [8] S. Na, O. Collin, F. Chowdhury, B. Tay, M.X. Ouyang, Y.X. Wang, N. Wang, Rapid signal transduction in living cells is a unique feature of mechanotransduction, *Proceedings of the National Academy of Sciences of the United States of America* 105 (2008) 6626-6631.
- [9] J.B. Recknor, D.S. Sakaguchi, S.K. Mallapragada, Directed growth and selective differentiation of neural progenitor cells on micropatterned polymer substrates, *Biomaterials* 27 (2006) 4098-4108.
- [10] D. Zahor, A. Radko, R. Vago, L.A. Gheber, Organization of mesenchymal stem cells is controlled by micropatterned silicon substrates, *Materials Science & Engineering C-Biomimetic and Supramolecular Systems* 27 (2007) 117-121.
- [11] E. Engel, E. Martinez, C.A. Mills, M. Funes, J.A. Planell, J. Samitier, Mesenchymal stem cell differentiation on microstructured poly (methyl methacrylate) substrates, *Annals of Anatomy-Anatomischer Anzeiger* 191 (2009) 136-144.
- [12] J.M. Karp, J. Yeh, G. Eng, J. Fukuda, J. Blumling, K.Y. Suh, J. Cheng, A. Mahdavi, J. Borenstein, R. Langer, A. Khademhosseini, Controlling size, shape and homogeneity of embryoid bodies using poly(ethylene glycol) microwells, *Lab on a Chip* 7 (2007) 786-794.

- [13] C. O'Neill, P. Jordan, G. Ireland, Evidence for two distinct mechanisms of anchorage stimulation in freshly explanted and 3T3 Swiss mouse fibroblasts, *Cell* 44 (1986) 489-496.
- [14] Y.X. Wang, N. Wang, FRET and mechanobiology, *Integrative Biology* 1 (2009) 565-573.
- [15] D.A. Lauffenburger, A.F. Horwitz, Cell migration: A physically integrated molecular process, *Cell* 84 (1996) 359-369.
- [16] A.J. Ridley, M.A. Schwartz, K. Burridge, R.A. Firtel, M.H. Ginsberg, G. Borisy, J.T. Parsons, A.R. Horwitz, Cell migration: Integrating signals from front to back, *Science* 302 (2003) 1704-1709.
- [17] R.J. Petrie, A.D. Doyle, K.M. Yamada, Random versus directionally persistent cell migration, *Nature Reviews Molecular Cell Biology* 10 (2009) 538-549.
- [18] M. Bailly, L. Yan, G.M. Whitesides, J.S. Condeelis, J.E. Segall, Regulation of protrusion shape and adhesion to the substratum during chemotactic responses of mammalian carcinoma cells, *Experimental Cell Research* 241 (1998) 285-299.
- [19] W. Saadi, S.W. Rhee, F. Lin, B. Vahidi, B.G. Chung, N.L. Jeon, Generation of stable concentration gradients in 2D and 3D environments using a microfluidic ladder chamber, *Biomedical Microdevices* 9 (2007) 627-635.
- [20] N.L. Jeon, H. Baskaran, S.K.W. Dertinger, G.M. Whitesides, L. Van de Water, M. Toner, Neutrophil chemotaxis in linear and complex gradients of interleukin-8 formed in a microfabricated device, *Nature Biotechnology* 20 (2002) 826-830.

- [21] A. Wood, Contact Guidance on Microfabricated Substrata - the Response of Teleost Fin Mesenchyme Cells to Repeating Topographical Patterns, *Journal of Cell Science* 90 (1988) 667-681.
- [22] A. Webb, P. Clark, J. Skepper, A. Compston, A. Wood, Guidance of Oligodendrocytes and Their Progenitors by Substratum Topography, *Journal of Cell Science* 108 (1995) 2747-2760.
- [23] N. Gomez, S.C. Chen, C.E. Schmidt, Polarization of hippocampal neurons with competitive surface stimuli: contact guidance cues are preferred over chemical ligands, *Journal of the Royal Society Interface* 4 (2007) 223-233.
- [24] D.K. Hoover, E.W.L. Chan, M.N. Yousaf, Asymmetric peptide nanoarray surfaces for studies of single cell polarization, *Journal of the American Chemical Society* 130 (2008) 3280-+.
- [25] M.J.P. Biggs, R.G. Richards, N. Gadegaard, R.J. McMurray, S. Affrossman, C.D.W. Wilkinson, R.O.C. Oreffo, M.J. Dalby, Interactions with nanoscale topography: Adhesion quantification and signal transduction in cells of osteogenic and multipotent lineage, *Journal of Biomedical Materials Research Part A* 91A (2009) 195-208.
- [26] Y.S. Hwang, B.G. Chung, D. Ortmann, N. Hattori, H.C. Moeller, A. Khademhosseini, Microwell-mediated control of embryoid body size regulates embryonic stem cell fate via differential expression of WNT5a and WNT11, *Proceedings of the National Academy of Sciences of the United States of America* 106 (2009) 16978-16983.

- [27] E. Martinez, E. Engel, J.A. Planell, J. Samitier, Effects of artificial micro- and nano-structured surfaces on cell behaviour, *Annals of Anatomy-Anatomischer Anzeiger* 191 (2009) 126-135.
- [28] V.C. Hirschfeld-Warneken, M. Arnold, A. Cavalcanti-Adam, M. Lopez-Garcia, H. Kessler, J.P. Spatz, Cell adhesion and polarisation on molecularly defined spacing gradient surfaces of cyclic RGDfK peptide patches, *European Journal of Cell Biology* 87 (2008) 743-750.
- [29] A.S. Sarvestani, E. Jabbari, Analysis of Cell Locomotion on Ligand Gradient Substrates, *Biotechnology and Bioengineering* 103 (2009) 424-429.
- [30] E. Cukierman, R. Pankov, D.R. Stevens, K.M. Yamada, Taking cell-matrix adhesions to the third dimension, *Science* 294 (2001) 1708-1712.
- [31] S. Even-Ram, K.M. Yamada, Cell migration in 3D matrix, *Current Opinion in Cell Biology* 17 (2005) 524-532.
- [32] U.B.T. Giang, D. Lee, M.R. King, L.A. DeLouise, Microfabrication of cavities in polydimethylsiloxane using DRIE silicon molds, *Lab on a Chip* 7 (2007) 1660-1662.
- [33] S.H. Chao, R. Carlson, D.R. Meldrum, Rapid fabrication of microchannels using microscale plasma activated templating ( $\mu$  PLAT) generated water molds, *Lab on a Chip* 7 (2007) 641-643.
- [34] J.Y. Park, C.M. Hwang, S.H. Lee, Ice-lithographic fabrication of concave microwells and a microfluidic network, *Biomedical Microdevices* 11 (2009) 129-133.

- [35] Y. Yi, J.H. Kang, J.K. Park, Moldless electroplating for cylindrical microchannel fabrication, *Electrochemistry Communications* 7 (2005) 913-917.
- [36] M.B. Chan-Park, C. Yang, X. Guo, L.Q. Chen, S.F. Yoon, J.H. Chun, Fabrication of 3-D curved microstructures by constrained gas expansion and photopolymerization, *Langmuir* 24 (2008) 5492-5499.
- [37] M. Okochi, S. Takano, Y. Isaji, T. Senga, M. Hamaguchi, H. Honda, Three-dimensional cell culture array using magnetic force-based cell patterning for analysis of invasive capacity of BALB/3T3/v-src, *Lab on a Chip* 9 (2009) 3378-3384.
- [38] R.D. Piner, J. Zhu, F. Xu, S.H. Hong, C.A. Mirkin, "Dip-pen" nanolithography, *Science* 283 (1999) 661-663.
- [39] K.B. Lee, S.J. Park, C.A. Mirkin, Protein nanoarrays generated by Dip-Pen Nanolithography., *Abstracts of Papers of the American Chemical Society* 223 (2002) C94-C94.
- [40] A.N. Broers, W.W. Molzen, J.J. Cuomo, N.D. Wittels, Electron-Beam Fabrication of 80-Å Metal Structures, *Applied Physics Letters* 29 (1976) 596-598.
- [41] S. Yasin, D.G. Hasko, H. Ahmed, Fabrication of < 5 nm width lines in poly(methylmethacrylate) resist using a water : isopropyl alcohol developer and ultrasonically-assisted development, *Applied Physics Letters* 78 (2001) 2760-2762.
- [42] J.D. Hoff, L.J. Cheng, E. Meyhofer, L.J. Guo, A.J. Hunt, Nanoscale protein patterning by imprint lithography, *Nano Letters* 4 (2004) 853-857.

- [43] G.Y. Liu, S. Xu, Y.L. Qian, Nanofabrication of self-assembled monolayers using scanning probe lithography, *Accounts of Chemical Research* 33 (2000) 457-466.
- [44] D. Zhou, A. Bruckbauer, L.M. Ying, C. Abell, D. Klenerman, Building three-dimensional surface biological assemblies on the nanometer scale, *Nano Letters* 3 (2003) 1517-1520.
- [45] T. Dvir, B.P. Timko, D.S. Kohane, R. Langer, Nanotechnological strategies for engineering complex tissues, *Nat Nano* 6 (2011) 13-22.
- [46] S.H. Hu, L. Eberhard, J.X. Chen, J.C. Love, J.P. Butler, J.J. Fredberg, G.M. Whitesides, N. Wang, Mechanical anisotropy of adherent cells probed by a three-dimensional magnetic twisting device, *American Journal of Physiology-Cell Physiology* 287 (2004) C1184-C1191.
- [47] J. Yu, J. Xiao, X.J. Ren, K.Q. Lao, X.S. Xie, Probing gene expression in live cells, one protein molecule at a time, *Science* 311 (2006) 1600-1603.
- [48] J.H. Hyun, H.W. Ma, Z.P. Zhang, T.P. Beebe, A. Chilkoti, Universal route to cell micropatterning using an amphiphilic comb polymer, *Advanced Materials* 15 (2003) 576-579.
- [49] H.W. Ma, J. Hyun, Z.P. Zhang, T.P. Beebe, A. Chilkoti, Fabrication of biofunctionalized quasi-three-dimensional microstructures of a nonfouling comb polymer using soft lithography, *Advanced Functional Materials* 15 (2005) 529-540.
- [50] J.A. Rogers, R.G. Nuzzo, Recent progress in soft lithography, *Materials Today* 8 (2005) 50-56.

- [51] S. Takayama, E. Ostuni, P. LeDuc, K. Naruse, D.E. Ingber, G.M. Whitesides, Laminar flows - Subcellular positioning of small molecules, *Nature* 411 (2001) 1016-1016.
- [52] A. Folch, M. Toner, Cellular micropatterns on biocompatible materials, *Biotechnology Progress* 14 (1998) 388-392.
- [53] O. Hartman, C. Zhang, E.L. Adams, M.C. Farach-Carson, N.J. Petrelli, B.D. Chase, J.F. Rabolt, Microfabricated Electrospun Collagen Membranes for 3-D Cancer Models and Drug Screening Applications (vol 10, pg 2031, 2009), *Biomacromolecules* 10 (2009) 2718-2718.
- [54] W.L. Neeley, S. Redenti, H. Klassen, S. Tao, T. Desai, M.J. Young, R. Langer, A microfabricated scaffold for retinal progenitor cell grafting, *Biomaterials* 29 (2008) 418-426.
- [55] J. Park, M. Toner, M.L. Yarmush, A.W. Tilles, Microchannel bioreactors for bioartificial liver support, *Microfluidics and Nanofluidics* 2 (2006) 525-535.
- [56] M.A. Alyassin, S. Moon, H.O. Keles, F. Manzur, R.L. Lin, E. Haeggstrom, D.R. Kuritzkes, U. Demirci, Rapid automated cell quantification on HIV microfluidic devices, *Lab on a Chip* 9 (2009) 3364-3369.
- [57] A. Carraro, W.M. Hsu, K.M. Kulig, W.S. Cheung, M.L. Miller, E.J. Weinberg, E.F. Swart, M. Kaazempur-Mofrad, J.T. Borenstein, J.P. Vacanti, C. Neville, In vitro analysis of a hepatic device with intrinsic microvascular-based channels, *Biomedical Microdevices* 10 (2008) 795-805.

- [58] L.C. Abraham, J.F. Dice, P.F. Finn, N.T. Mesires, K. Lee, D.L. Kaplan, Extracellular matrix remodeling - Methods to quantify cell-matrix interactions, *Biomaterials* 28 (2007) 151-161.
- [59] B.M. Gillette, J.A. Jensen, B.X. Tang, G.J. Yang, A. Bazargan-Lari, M. Zhong, S.K. Sia, In situ collagen assembly for integrating microfabricated three-dimensional cell-seeded matrices, *Nature Materials* 7 (2008) 636-640.
- [60] S.X. Hsiong, T. Boonthekul, N. Huebsch, D.J. Mooney, Cyclic Arginine-Glycine-Aspartate Peptides Enhance Three-Dimensional Stem Cell Osteogenic Differentiation, *Tissue Engineering Part A* 15 (2009) 263-272.
- [61] S.R. Khetani, S.N. Bhatia, Microscale culture of human liver cells for drug development, *Nature Biotechnology* 26 (2008) 120-126.
- [62] M.J. Brown, L.M. Loew, Electric Field-Directed Fibroblast Locomotion Involves Cell-Surface Molecular Reorganization and Is Calcium-Independent, *Journal of Cell Biology* 127 (1994) 117-128.
- [63] S.B. Carter, Principles of cell motility: the direction of cell movement and cancer invasion, *Nature* 208 (1965) 1183-1187.
- [64] S.B. Carter, Haptotaxis and the mechanism of cell motility, *Nature* 213 (1967) 256-260.
- [65] A. Curtis, C. Wilkinson, Topographical control of cells, *Biomaterials* 18 (1997) 1573-1583.
- [66] B. Lowe, The role of Ca<sup>2+</sup> in deflection-induced excitation of motile, mechanoresponsive balancer cilia in the ctenophore statocyst, *J Exp Biol* 200 (1997) 1593-1606.

- [67] J. Saranak, K.W. Foster, Rhodopsin guides fungal phototaxis, *Nature* 387 (1997) 465-466.
- [68] G. Bao, S. Suresh, Cell and molecular mechanics of biological materials, *Nature Materials* 2 (2003) 715-725.
- [69] P.A. Janmey, C.A. McCulloch, Cell mechanics: integrating cell responses to mechanical stimuli, *Annual Review of Biomedical Engineering* 9 (2007) 1-34.
- [70] D.S. Gray, J. Tien, C.S. Chen, Repositioning of cells by mechanotaxis on surfaces with micropatterned Young's modulus, *Journal of Biomedical Materials Research Part A* 66A (2003) 605-614.
- [71] C.M. Lo, H.B. Wang, M. Dembo, Y.L. Wang, Cell movement is guided by the rigidity of the substrate, *Biophysical Journal* 79 (2000) 144-152.
- [72] J.Y. Wong, A. Velasco, P. Rajagopalan, Q. Pham, Directed movement of vascular smooth muscle cells on gradient-compliant hydrogels, *Langmuir* 19 (2003) 1908-1913.
- [73] J.T. Connelly, J.E. Gautrot, B. Trappmann, D.W.M. Tan, G. Donati, W.T.S. Huck, F.M. Watt, Actin and serum response factor transduce physical cues from the microenvironment to regulate epidermal stem cell fate decisions, *Nature Cell Biology* 12 (2010) 711-U177.
- [74] J.P. Fu, Y.K. Wang, M.T. Yang, R.A. Desai, X.A. Yu, Z.J. Liu, C.S. Chen, Mechanical regulation of cell function with geometrically modulated elastomeric substrates, *Nat Methods* 7 (2010) 733-U795.
- [75] P.M. Gilbert, K.L. Havenstrite, K.E.G. Magnusson, A. Sacco, N.A. Leonardi, P. Kraft, N.K. Nguyen, S. Thrun, M.P. Lutolf, H.M. Blau, Substrate Elasticity

Regulates Skeletal Muscle Stem Cell Self-Renewal in Culture, *Science* 329 (2010) 1078-1081.

- [76] N. Huebsch, P.R. Arany, A.S. Mao, D. Shvartsman, O.A. Ali, S.A. Bencherif, J. Rivera-Feliciano, D.J. Mooney, Harnessing traction-mediated manipulation of the cell/matrix interface to control stem-cell fate, *Nature Materials* 9 (2010) 518-526.
- [77] K.R. Levental, H.M. Yu, L. Kass, J.N. Lakins, M. Egeblad, J.T. Emler, S.F.T. Fong, K. Csiszar, A. Giaccia, W. Weninger, M. Yamauchi, D.L. Gasser, V.M. Weaver, Matrix Crosslinking Forces Tumor Progression by Enhancing Integrin Signaling, *Cell* 139 (2009) 891-906.
- [78] H. Sunami, I. Yokota, Y. Igarashi, Influence of the pattern size of micropatterned scaffolds on cell morphology, proliferation, migration and F-actin expression, *Biomaterials Science* 2 (2014) 399-409.
- [79] Y.S. Choi, L.G. Vincent, A.R. Lee, K.C. Kretchmer, S. Chirasatitsin, M.K. Dobke, A.J. Engler, The alignment and fusion assembly of adipose-derived stem cells on mechanically patterned matrices, *Biomaterials* 33 (2012) 6943-6951.
- [80] C.H.R. Kuo, J. Xian, J.D. Brenton, K. Franze, E. Sivaniah, Complex Stiffness Gradient Substrates for Studying Mechanotactic Cell Migration, *Advanced Materials* 24 (2012) 6059-+.
- [81] P. Tseng, D. Di Carlo, Substrates with Patterned Extracellular Matrix and Subcellular Stiffness Gradients Reveal Local Biomechanical Responses, *Advanced Materials* 26 (2014) 1242-1247.

- [82] N.Q. Balaban, U.S. Schwarz, D. Riveline, P. Goichberg, G. Tzur, I. Sabanay, D. Mahalu, S. Safran, A. Bershadsky, L. Addadi, B. Geiger, Force and focal adhesion assembly: a close relationship studied using elastic micropatterned substrates, *Nature Cell Biology* 3 (2001) 466-472.
- [83] J.L. Tan, J. Tien, D.M. Pirone, D.S. Gray, K. Bhadriraju, C.S. Chen, Cells lying on a bed of microneedles: An approach to isolate mechanical force, *Proceedings of the National Academy of Sciences of the United States of America* 100 (2003) 1484-1489.
- [84] R.D. Sochol, A.T. Higa, R.R.R. Janairo, S. Li, L.W. Lin, Unidirectional mechanical cellular stimuli via micropost array gradients, *Soft Matter* 7 (2011) 4606-4609.
- [85] M. Allieux-Guerin, D. Icard-Arcizet, C. Durieux, S. Henon, F. Gallet, J.C. Mevel, M.J. Masse, M. Tramier, M. Coppey-Moisan, Spatiotemporal Analysis of Cell Response to a Rigidity Gradient: A Quantitative Study Using Multiple Optical Tweezers, *Biophysical Journal* 96 (2009) 238-247.
- [86] M.A. Wozniak, K. Modzelewska, L. Kwong, P.J. Keely, Focal adhesion regulation of cell behavior, *Biochimica Et Biophysica Acta-Molecular Cell Research* 1692 (2004) 103-119.
- [87] I. Schoen, W. Hu, E. Klotzsch, V. Vogel, Probing Cellular Traction Forces by Micropillar Arrays: Contribution of Substrate Warping to Pillar Deflection, *Nano Letters* 10 (2010) 1823-1830.
- [88] Q. Cheng, Z. Sun, G.A. Meininger, M. Almasri, Note: Mechanical study of micromachined polydimethylsiloxane elastic microposts, *Review of Scientific Instruments* 81 (2010).

- [89] W. Chien-Wen, C. Wei-Ren, W. Ching-Chou, C. Hsien-Chang, Study on the Cell Mechanics of MDCK Cells by Elastic Micro-pillars Arrays, Nano/Micro Engineered and Molecular Systems, 2007. NEMS '07. 2nd IEEE International Conference on, 2007, pp. 1125-1128.
- [90] J. Park, J. Ryu, S.K. Choi, E. Seo, J.M. Cha, S. Ryu, J. Kim, B. Kim, S.H. Lee, Real-time measurement of the contractile forces of self-organized cardiomyocytes on hybrid biopolymer microcantilevers, *Analytical Chemistry* 77 (2005) 6571-6580.
- [91] Y. Zhao, X. Zhang, Adaptation of flexible polymer fabrication to cellular mechanics study, *Applied Physics Letters* 87 (2005).
- [92] H. Juhee, L. Sujin, P. Sukho, L. Junghoon, Micro checkerboard patterned polymeric surface with discrete rigidity for studying cell migration, *Journal of Micromechanics and Microengineering* 25 (2015) 045012.
- [93] A.J. Engler, M.A. Griffin, S. Sen, C.G. Bonnetmann, H.L. Sweeney, D.E. Discher, Myotubes differentiate optimally on substrates with tissue-like stiffness: pathological implications for soft or stiff microenvironments, *Journal of Cell Biology* 166 (2004) 877-887.
- [94] S. Romanazzo, G. Forte, M. Ebara, K. Uto, S. Pagliari, T. Aoyagi, E. Traversa, A. Taniguchi, Substrate stiffness affects skeletal myoblast differentiation in vitro, *Science and Technology of Advanced Materials* 13 (2012).
- [95] S.S. Chang, W.H. Guo, Y. Kim, Y.L. Wang, Guidance of Cell Migration by Substrate Dimension, *Biophysical Journal* 104 (2013) 313-321.

- [96] M. Nagayama, H. Haga, K. Kawabata, Drastic change of local stiffness distribution correlating to cell migration in living fibroblasts, *Cell Motility and the Cytoskeleton* 50 (2001) 173-179.
- [97] J. Solon, I. Levental, K. Sengupta, P.C. Georges, P.A. Janmey, Fibroblast adaptation and stiffness matching to soft elastic substrates, *Biophysical Journal* 93 (2007) 4453-4461.
- [98] T. Yeung, P.C. Georges, L.A. Flanagan, B. Marg, M. Ortiz, M. Funaki, N. Zahir, W.Y. Ming, V. Weaver, P.A. Janmey, Effects of substrate stiffness on cell morphology, cytoskeletal structure, and adhesion, *Cell Motility and the Cytoskeleton* 60 (2005) 24-34.
- [99] B.C. Isenberg, P.A. DiMilla, M. Walker, S. Kim, J.Y. Wong, Vascular Smooth Muscle Cell Durotaxis Depends on Substrate Stiffness Gradient Strength, *Biophysical Journal* 97 (2009) 1313-1322.
- [100] L.G. Vincent, Y.S. Choi, B. Alonso-Latorre, J.C. del Alamo, A.J. Engler, Mesenchymal stem cell durotaxis depends on substrate stiffness gradient strength, *Biotechnology Journal* 8 (2013) 472-+.
- [101] D. Gincel, H. Zaid, V. Shoshan-Barmatz, Calcium binding and translocation by the voltage-dependent anion channel: a possible regulatory mechanism in mitochondrial function, *Biochemical Journal* 358 (2001) 147-155.
- [102] M.Y. Vyssokikh, D. Brdiczka, The function of complexes between the outer mitochondrial membrane pore (VDAC) and the adenine nucleotide translocase in regulation of energy metabolism and apoptosis, *Acta Biochimica Polonica* 50 (2003) 389-404.

- [103] T.K. Rostovtseva, W.Z. Tan, M. Colombini, On the role of VDAC in apoptosis: Fact and fiction, *Journal of Bioenergetics and Biomembranes* 37 (2005) 129-142.
- [104] V. Shoshan-Barmatz, D. Gincel, The voltage-dependent anion channel - Characterization, modulation, and role in mitochondrial function in cell life and death, *Cell Biochemistry and Biophysics* 39 (2003) 279-292.
- [105] M.J. Berridge, Neuronal calcium signaling, *Neuron* 21 (1998) 13-26.
- [106] Z.S. Khachaturian, Hypothesis on the regulation of cytosol calcium concentration and the aging brain, *Neurobiol Aging* 8 (1987) 345-346.
- [107] G. Csordas, A.P. Thomas, G. Hajnoczky, Quasi-synaptic calcium signal transmission between endoplasmic reticulum and mitochondria, *Embo Journal* 18 (1999) 96-108.
- [108] L. Galluzzi, O. Kepp, C. Trojel-Hansen, G. Kroemer, Mitochondrial control of cellular life, stress, and death, *Circ Res* 111 (2012) 1198-1207.
- [109] T.J. Preston, A. Abadi, L. Wilson, G. Singh, Mitochondrial contributions to cancer cell physiology: potential for drug development, *Adv Drug Deliv Rev* 49 (2001) 45-61.
- [110] A. Deshpande, E. Mina, C. Glabe, J. Busciglio, Different conformations of amyloid beta induce neurotoxicity by distinct mechanisms in human cortical neurons, *J Neurosci* 26 (2006) 6011-6018.
- [111] H.L. Pahl, P.A. Baeuerle, Activation of NF-kappa B by ER stress requires both Ca<sup>2+</sup> and reactive oxygen intermediates as messengers, *Febs Letters* 392 (1996) 129-136.

- [112] H.K. Anandatheerthavarada, G. Biswas, M.A. Robin, N.G. Avadhani, Mitochondrial targeting and a novel transmembrane arrest of Alzheimer's amyloid precursor protein impairs mitochondrial function in neuronal cells, *Journal of Cell Biology* 161 (2003) 41-54.
- [113] L. Devi, B.M. Prabhu, D.F. Galati, N.G. Avadhani, H.K. Anandatheerthavarada, Accumulation of amyloid precursor protein in the mitochondrial import channels of human Alzheimer's disease brain is associated with mitochondrial dysfunction, *J Neurosci* 26 (2006) 9057-9068.
- [114] P.H. Reddy, Mitochondrial dysfunction in aging and Alzheimer's disease: strategies to protect neurons, *Antioxid Redox Signal* 9 (2007) 1647-1658.
- [115] J. Shin, C.H. Yoo, J. Lee, M. Cha, Cell response induced by internalized bacterial magnetic nanoparticles under an external static magnetic field, *Biomaterials* 33 (2012) 5650-5657.
- [116] J. Choi, J. Shin, J. Lee, M. Cha, Magnetic response of mitochondria-targeted cancer cells with bacterial magnetic nanoparticles, *Chem Commun (Camb)* 48 (2012) 7474-7476.
- [117] J. Dobson, Remote control of cellular behaviour with magnetic nanoparticles, *Nat Nanotechnol* 3 (2008) 139-143.
- [118] S. Hughes, S. McBain, J. Dobson, A.J. El Haj, Selective activation of mechanosensitive ion channels using magnetic particles, *Journal of the Royal Society Interface* 5 (2008) 855-863.

- [119] R.J. Mannix, S. Kumar, F. Cassiola, M. Montoya-Zavala, E. Feinstein, M. Prentiss, D.E. Ingber, Nanomagnetic actuation of receptor-mediated signal transduction, *Nat Nanotechnol* 3 (2008) 36-40.
- [120] A. Bianco, K. Kostarelos, M. Prato, Applications of carbon nanotubes in drug delivery, *Curr Opin Chem Biol* 9 (2005) 674-679.
- [121] Z. Liu, K. Chen, C. Davis, S. Sherlock, Q. Cao, X. Chen, H. Dai, Drug delivery with carbon nanotubes for in vivo cancer treatment, *Cancer Research* 68 (2008) 6652-6660.
- [122] Z. Liu, C. Davis, W. Cai, L. He, X. Chen, H. Dai, Circulation and long-term fate of functionalized, biocompatible single-walled carbon nanotubes in mice probed by Raman spectroscopy, *Proc Natl Acad Sci U S A* 105 (2008) 1410-1415.
- [123] S. Park, M. Cha, J. Lee, Promotion of cell growth with magnetically enhanced single-walled carbon nanotubes, *Diamond and Related Materials* 19 (2010) 942-945.
- [124] S. Park, J. Shin, J. Lee, M. Cha, Manipulation of NIH3T3 cells with functionalized single-walled carbon nanotubes under a magnetic field, *Materials Letters* 68 (2012) 378-381.
- [125] R. Singh, D. Pantarotto, L. Lacerda, G. Pastorin, C. Klumpp, M. Prato, A. Bianco, K. Kostarelos, Tissue biodistribution and blood clearance rates of intravenously administered carbon nanotube radiotracers, *Proc Natl Acad Sci U S A* 103 (2006) 3357-3362.

- [126] J.M. Worle-Knirsch, K. Pulskamp, H.F. Krug, Oops they did it again! Carbon nanotubes hoax scientists in viability assays, *Nano Letters* 6 (2006) 1261-1268.
- [127] L.H. Ding, J. Stilwell, T.T. Zhang, O. Elboudwarej, H.J. Jiang, J.P. Selegue, P.A. Cooke, J.W. Gray, F.Q.F. Chen, Molecular characterization of the cytotoxic mechanism of multiwall carbon nanotubes and nano-onions on human skin fibroblast, *Nano Letters* 5 (2005) 2448-2464.
- [128] A. Helland, P. Wick, A. Koehler, K. Schmid, C. Som, Reviewing the environmental and human health knowledge base of carbon nanotubes, *Environmental Health Perspectives* 115 (2007) 1125-1131.
- [129] D.A. Heller, S. Baik, T.E. Eurell, M.S. Strano, Single-walled carbon nanotube spectroscopy in live cells: Towards long-term labels and optical sensors, *Advanced Materials* 17 (2005) 2793-+.
- [130] L. Lacerda, A. Bianco, M. Prato, K. Kostarelos, Carbon nanotubes as nanomedicines: from toxicology to pharmacology, *Adv Drug Deliv Rev* 58 (2006) 1460-1470.
- [131] A.D. Maynard, P.A. Baron, M. Foley, A.A. Shvedova, E.R. Kisin, V. Castranova, Exposure to carbon nanotube material: aerosol release during the handling of unrefined single-walled carbon nanotube material, *J Toxicol Environ Health A* 67 (2004) 87-107.
- [132] J. Muller, F. Huaux, N. Moreau, P. Misson, J.F. Heilier, M. Delos, M. Arras, A. Fonseca, J.B. Nagy, D. Lison, Respiratory toxicity of multi-wall carbon nanotubes, *Toxicology and Applied Pharmacology* 207 (2005) 221-231.

- [133] A.A. Shvedova, V. Castranova, E.R. Kisin, D. Schwegler-Berry, A.R. Murray, V.Z. Gandelsman, A. Maynard, P. Baron, Exposure to carbon nanotube material: Assessment of nanotube cytotoxicity using human keratinocyte cells, *Journal of Toxicology and Environmental Health-Part A* 66 (2003) 1909-1926.
- [134] A.A. Shvedova, E.R. Kisin, R. Mercer, A.R. Murray, V.J. Johnson, A.I. Potapovich, Y.Y. Tyurina, O. Gorelik, S. Arepalli, D. Schwegler-Berry, A.F. Hubbs, J. Antonini, D.E. Evans, B.K. Ku, D. Ramsey, A. Maynard, V.E. Kagan, V. Castranova, P. Baron, Unusual inflammatory and fibrogenic pulmonary responses to single-walled carbon nanotubes in mice, *Am J Physiol Lung Cell Mol Physiol* 289 (2005) L698-708.
- [135] L.Z. Gao, J. Zhuang, L. Nie, J.B. Zhang, Y. Zhang, N. Gu, T.H. Wang, J. Feng, D.L. Yang, S. Perrett, X. Yan, Intrinsic peroxidase-like activity of ferromagnetic nanoparticles, *Nat Nanotechnol* 2 (2007) 577-583.
- [136] Z. Genfa, P.K. Dasgupta, Hematin as a Peroxidase Substitute in Hydrogen-Peroxide Determinations, *Analytical Chemistry* 64 (1992) 517-522.
- [137] Q. Wang, Z. Yang, X. Zhang, X. Xiao, C.K. Chang, B. Xu, A supramolecular-hydrogel-encapsulated hemin as an artificial enzyme to mimic peroxidase, *Angew Chem Int Ed Engl* 46 (2007) 4285-4289.
- [138] R. Cui, Z. Han, J.J. Zhu, Helical carbon nanotubes: intrinsic peroxidase catalytic activity and its application for biocatalysis and biosensing, *Chemistry* 17 (2011) 9377-9384.
- [139] F. Qu, T. Li, M. Yang, Colorimetric platform for visual detection of cancer biomarker based on intrinsic peroxidase activity of graphene oxide, *Biosensors & Bioelectronics* 26 (2011) 3927-3931.

- [140] Y. Song, X. Wang, C. Zhao, K. Qu, J. Ren, X. Qu, Label-free colorimetric detection of single nucleotide polymorphism by using single-walled carbon nanotube intrinsic peroxidase-like activity, *Chemistry* 16 (2010) 3617-3621.
- [141] E. Lam, S. Hrapovic, E. Majid, J.H. Chong, J.H. Luong, Catalysis using gold nanoparticles decorated on nanocrystalline cellulose, *Nanoscale* 4 (2012) 997-1002.
- [142] N. Pradhan, A. Pal, T. Pal, Silver nanoparticle catalyzed reduction of aromatic nitro compounds, *Colloids and Surfaces a-Physicochemical and Engineering Aspects* 196 (2002) 247-257.
- [143] X.L. Zuo, C. Peng, Q. Huang, S.P. Song, L.H. Wang, D. Li, C.H. Fan, Design of a Carbon Nanotube/Magnetic Nanoparticle-Based Peroxidase-Like Nanocomplex and Its Application for Highly Efficient Catalytic Oxidation of Phenols, *Nano Research* 2 (2009) 617-623.
- [144] Y. Guo, L. Deng, J. Li, S. Guo, E. Wang, S. Dong, Hemin-graphene hybrid nanosheets with intrinsic peroxidase-like activity for label-free colorimetric detection of single-nucleotide polymorphism, *Acs Nano* 5 (2011) 1282-1290.
- [145] T. Tanaka, T. Matsunaga, Fully automated chemiluminescence immunoassay of insulin using antibody-protein A-bacterial magnetic particle complexes, *Analytical Chemistry* 72 (2000) 3518-3522.
- [146] A.G. Osorio, I.C.L. Silveira, V.L. Bueno, C.P. Bergmann, H<sub>2</sub>SO<sub>4</sub>/HNO<sub>3</sub>/HCl-Functionalization and its effect on dispersion of carbon nanotubes in aqueous media, *Applied Surface Science* 255 (2008) 2485-2489.

- [147] L.G. Cancado, A. Jorio, E.H.M. Ferreira, F. Stavale, C.A. Achete, R.B. Capaz, M.V.O. Moutinho, A. Lombardo, T.S. Kulmala, A.C. Ferrari, Quantifying Defects in Graphene via Raman Spectroscopy at Different Excitation Energies, *Nano Letters* 11 (2011) 3190-3196.
- [148] M.A. Correa-Duarte, M. Grzelczak, V. Salgueirino-Maceira, M. Giersig, L.M. Liz-Marzan, M. Farle, K. Sieradzki, R. Diaz, Alignment of carbon nanotubes under low magnetic fields through attachment of magnetic nanoparticles, *Journal of Physical Chemistry B* 109 (2005) 19060-19063.
- [149] M.H. Liao, D.H. Chen, Preparation and characterization of a novel magnetic nano-adsorbent, *Journal of Materials Chemistry* 12 (2002) 3654-3659.
- [150] S.A. Hudson, H. Ecroyd, T.W. Kee, J.A. Carver, The thioflavin T fluorescence assay for amyloid fibril detection can be biased by the presence of exogenous compounds, *Febs Journal* 276 (2009) 5960-5972.
- [151] V.E. Kagan, N.V. Konduru, W.H. Feng, B.L. Allen, J. Conroy, Y. Volkov, I.I. Vlasova, N.A. Belikova, N. Yanamala, A. Kapralov, Y.Y. Tyurina, J.W. Shi, E.R. Kisin, A.R. Murray, J. Franks, D. Stolz, P.P. Gou, J. Klein-Seetharaman, B. Fadeel, A. Star, A.A. Shvedova, Carbon nanotubes degraded by neutrophil myeloperoxidase induce less pulmonary inflammation, *Nat Nanotechnol* 5 (2010) 354-359.
- [152] J.H. Luo, S.K.T.S. Warmlander, C.H. Yu, K. Muhammad, A. Graslund, J.P. Abrahams, The A beta peptide forms non-amyloid fibrils in the presence of carbon nanotubes, *Nanoscale* 6 (2014) 6720-6726.

## 국문초록

본 학위 논문에서는, 다양한 형태와 물성을 지닌 마이크로 나노 스케일 물질을 이용하여 세포에 물리적 자극을 가하고 그 영향을 보고자 한다. 이를 위해 세포가 부착된 부분의 면적은 일정하게 유지하면서 경도의 차이를 형성하기 위해 계단식으로 이중 원형 기둥구조를 고안하였다. 그 다음으로 자성나노입자와 세포 표면에 다량으로 존재하여 세포기작에 관여하는 세포막 수용체에 특이적으로 결합하는 단백질 즉 항체를 이용하여 신경세포의 증식을 조절하였다. 또한 단일 벽 탄소나노튜브에 자성나노입자를 부착하여 알츠하이머를 유발하는 아밀로이드 베타의 형성을 저지하였고, 이를 이용해 신경세포의 활성을 촉진하도록 하였다. 본 논문은 나노 마이크로 스케일의 구조물이 세포의 움직임 및 활성화에 미치는 영향에 대한 기초적인 자료가 될 수 있을 것이다.

먼저, 세포부착표면의 경도차이를 이용하여 세포의 이동성을 관찰하기 위해 고분자 화합물로 이루어진 마이크로 원형 기둥구조를 고안하였다. 세포가 부착된 부분의 면적은 일정하게 유지하면서 경도의 차이를 형성하기 위해 계단식으로 이중 원형 기둥구조를 고안하였다. 계단식으로 이루어진 고분자 기둥 이중구조(SMPAD)는 적절한 기계적 강도를 구현하기 위해 아래 단의 직경은 강도에 비례하게 조절하고, 셀과 접촉하는 단의 직경은 세포와 부착되는 면적을 일정하게 유지하기 위해 모든 직경을 고정 하였다. 세포의 부착을 용이하게 하기 위해 기둥 구조물의 표면에 파이브로넥틴을 균일하게 코팅하였다. C2C12, HeLa 및 NIH3T3의 세포를 SMPAD상에서 배양하고, 부착된 세포의 움직임은 오랜 시간 동안 현미경으로 연속 촬영하여 이동성을 추적 관찰할 수 있게 하였다. 우리는 이러한 연구를 통해 순수한 물리적 자극을 구현할 수 있는 마이크로 구조 플랫폼을 고안하였고, 이러한 외부 자극에 의해 세포의 움직임이 크게 영향을 받는다는 것을 관찰하였다.

그 다음으로, 자성나노입자와 VDAC2 항체를 이용하여 신경세포의 증식을 조절하였다. 본 연구에서 표적으로 하는 입자는 세포막과 미토콘드리아 외 막에 존재하여 이온 전달에 관여하는 Voltage-dependent anion-selective channel2(VDAC2) 단백질로, 특정 자극을 받으면 ion의 이동을 조절하여 세포기작에 영향을 미치는 단백질이다. 본 연구에서는 VDAC2 항체를 박테리아 표면에 접합한 'BMP-VDAC2 Antibody' 접합체로 제어하여 신경세포의 성장과 생존율을 조절하는 것을 목표로 한다. 또한 이러한 접합체가 처리된 세포에 외부자극을 이용하여 VDAC2 단백질에 직접적으로 물리적 자극을 준 후 세포의 거동을 관찰하고 VDAC2의 생체 내 물리학적 역할을 규명하였다.

마지막으로, 자성나노입자의 과산화효소적인 성질을 이용하여 단일벽 탄소나노튜브의 자가분해를 유도하여 이를 세포 실험에 이용하였다. 탄소나노튜브는 세포독성을 보일 수 있기 때문에 다양한 장점에도 불구하고 세포치료에 사용하는 것이 꺼려져 왔다. 따라서 본 연구에서는 자성나노입자를 이용하여 탄소나노튜브의 자가분해를 유도하고자 하였다. 자성나노입자의 표면에 다량으로 존재하는 아민기를 이용하여 탄소나노튜브의 카복실기에 부착하였고, 전자현미경과 EDX, XPS 등의 분석법을 통해 두 가지 물질이 공유 결합되어 있다는 것을 확인하였다. 탄소나노튜브의 자가분해를 유도하기 위해서 미량의 과산화수소를 접합체에 하루 동안 처리하였고, 투과전자현미경 및 라만분광법을 통하여 자성나노입자가 탄소나노튜브의 분해에 관여한다는 사실을 알 수 있었다. 그 뒤에는 제작된 자성나노입자-탄소나노튜브 접합체를 이용하여 알츠하이머를 유발하는 물질로 알려진 아밀로이드베타 섬유단백질의 발생을 억제하는 실험을 진행하였다. 이러한 현상을 세포실험에서 확인하기 위해 SH-SY5Y 세포에 아밀로이드베타와 자성나노입자-탄소나노튜브 접합체를 함께 첨가하여 3일간 배양하였고 세포 접합체가 첨가된 실험 군의 세포사멸이 현저하게 저하되는 결과를 얻었다.

**주요어:** 이중기둥구조, 박테리아 자성나노입자, 단일벽 탄소나노튜브, 세포이동, 미토콘드리아, 자가분해

**학번:** 2009-31248